# Physik Department

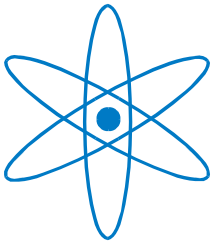

Kinetics of polymer desorption from solid substrates and supported lipid bilayers

Dissertation

von

Stefanie Krysiak

Technische Universität

München

TECHNISCHE UNIVERSITÄT MÜNCHEN

Physik-Department

Lehrstuhl für Biophysik E22

und

Zentralinstitut für Medizintechnik

# Kinetics of polymer desorption from solid substrates and supported lipid bilayers

Stefanie Krysiak

Vollständiger Abdruck der von der Fakultät für Physik der Technischen Universität München zur Erlangung des akademischen Grades eines

Doktors der Naturwissenschaften (Dr. rer. nat.)

genehmigten Dissertation.

Vorsitzender: Univ.-Prof. Dr. U. Gerland

Prüfer der Dissertation:

1. Univ.-Prof. Dr. T. Hugel
   Albert-Ludwigs-Universität Freiburg
2. Univ.-Prof. Dr. M. Rief

Die Dissertation wurde am 12.02.2015 bei der Technischen Universität München eingereicht und durch die Fakultät für Physik am 08.04.2015 angenommen.

# Table of contents

Summary ..... 9
1 Introduction ..... 11
2 Fundamental principles ..... 15
2.1 Polymer models ..... 15
2.1.1 Worm like chain and freely jointed chain ..... 15
2.1.2 Extended models ..... 16
2.1.3 Rouse Model ..... 17
2.2 Intermolecular forces and bonds ..... 17
2.2.1 Electrostatic forces ..... 18
2.2.2 Van der Waals forces ..... 18
2.2.3 Covalent bonds ..... 20
2.2.4 Coordination complex ..... 20
2.2.5 Hydrophobic interaction ..... 20
2.2.6 Adhesion and interfacial energy ..... 21
2.3 Bonds under force ..... 21
2.3.1 Bell Model ..... 22
2.3.2 Loading rate dependence ..... 22
2.3.3 The rebinding rate ..... 24
2.3.4 Multiple Bonds under force ..... 24
2.3.5 Determining Bond valency ..... 25
2.4 Protein membrane interactions ..... 27
2.4.1 Lipid bilayer ..... 27
2.4.2 Membrane proteins and their adhesion mechanisms ..... 29
2.4.3 Phospholipase A2 – membrane interactions ..... 30
2.5 Mussel based biomimetic adhesive ..... 31
3 Materials and Methods ..... 33
3.1 Biomolecules ..... 33
3.1.1 Polyhomopeptides ..... 33

3.1.2 Dendritic Polymers ..... 35
3.1.3 Phospholipase A2 ..... 35
3.1.4 Elastin like polypeptides ..... 36
3.2 Surface preparation and characterization ..... 36
3.2.1 Hydrophobic surfaces ..... 37
3.2.2 Surface characterization ..... 38
3.2.3 Maleimide functionalized glass ..... 38
3.2.4 Metal oxides ..... 39
3.2.5 Supported lipid bilayer ..... 39
3.3 Atomic Force Microscope ..... 41
3.3.1 Imaging with an AFM ..... 42
3.3.1 Single Molecule Force Spectroscopy measurements ..... 42
3.3.2 Calibration ..... 47
3.4 Data Analysis ..... 48
3.4.1 Plateau length and force ..... 48
3.4.2 Rupture force analysis ..... 48
4 Single polypeptide desorption kinetics on hydrophobic surfaces ..... 51
4.1 Solvent effect on desorption length and desorption force ..... 52
4.2 Waiting time - desorption at constant distance ..... 57
4.3 Simultaneous fit of measurements ..... 62
4.4 Effect of a readsorption rate and velocity dependence ..... 64
4.5 Conclusion ..... 66
5 Polypeptide desorption experiments on supported lipid bilayers ..... 69
5.1 Desorption forces of different polyhomopeptides on DOPC ..... 70
5.2 Desorption length of different polyhomopeptides on DOPC ..... 77
5.3 Velocity dependence of most probable desorption forces on DOPC ..... 80
5.4 Variation of dwell time and trigger force for polytryptophan on DOPC ..... 85
5.5 Desorption of Phospholipase A2 from DOPC/DOPS ..... 88
5.6 Conclusion ..... 92
6 Desorption of biomimetic dendritic adhesives ..... 95

6.1 Desorption force of dopamine from $TiO_2$ ..... 96
6.2 Desorption of different catechol functionalized architectures from $TiO_2$ ..... 100
6.3 Desorption force of catechol functionalized hPG from $TiO_2$ ..... 103
6.4 Dwell time effect ..... 105
6.5 Conclusion ..... 111
7 Conclusion and Outlook ..... 113
Appendix ..... 115
Bibliography ..... 123
List of publications ..... 129
Acknowledgements ..... 131

# Summary

Glue is present everywhere in modern everyday life and mostly we are only aware of it once it fails. While sticking objects together with the help of glue is a century old technique, adhesives have faced a boom in the last century. Our modern society increasingly relies on synthetic adhesives to produce products ranging from smart phones to cars. Over 50% of Henkels 16 billion euro revenue stems from adhesive technology. [1] But there remain challenges to the use of adhesives like the long term stability or the difficulties in gluing wet surfaces. Some of this research is focused on studying adhesion in nature and adapting the principles to synthetic materials. Here, adhesion of both natural and synthetic systems was studied on a single molecule level. Therefore, atomic force microscope (AFM) based single molecule force spectroscopy experiments were chosen. With the AFM forces on the piconewton scale in physiological conditions with a single polypeptide can be measured to understand both natural and synthetic adhesion phenomena in more detail.

In this study single molecule force probes were used to study the desorption kinetics of single polyhomopeptide chains on hydrophobic surfaces to learn more about the stability of non-covalent adhesives bonds. It was possible to determine all relevant kinetic parameters, namely the polymer contour length $L_c$, the adsorption free energy per monomer $\lambda$, the Kuhn or persistence length depending on the polymer model and the monomeric desorption rate $k_0$, due to employing two complementary experimental protocols. On one hand standard constant velocity experiments and on the other hand waiting time experiments at constant distance. The kinetics of the biopolymers exhibited a power law dependence on chain length and a high cooperativity of the chain lead to slowed down dynamics compared to the desorption of monomeric amino acids.

In a next step a more biological system, namely the adhesion of different polyhomopeptides on a supported zwitterionic lipid bilayer was investigated. This is important to understand the mechanism underlying the adhesion of membrane proteins to different kinds of biological membranes. Together with experiments performed with a peripheral membrane protein, the result underlines the importance of aromatic amino acids for strong interactions between proteins and zwitterionic membranes.

Finally a mussel inspired dendritic adhesive was investigated. The extraordinary adhesive properties of mussels are attributed to catechols, but a lot of questions remain about the molecular mechanism. Here, the adhesion of mussel inspired dendritic adhesives to metal oxides was studied. High forces in the range of half a nN were needed to desorb a single

dopamine with a catechol group from a titanium dioxide surface at low pH. Using hyperbranched polyglycerols (hPG) with several catecholic endgroups enhances the adhesion to $TiO_2$ and multivalent adhesion of forces over 1nN were observed. Therefore hyperbranched polyglycerols with added catecholic endgroups are a promising candidate for durable surface coatings in aqueous environment.

# 1 Introduction

Adhesives are part of nearly all modern products. The global market for adhesives was 8977 kilo tons in 2013, which corresponds to 1.5 kg per person. [2] While sticking objects together with the help of glue is a century old technique, adhesives have faced a boom in the last century. More than 120,000 years ago in the middle Pleistocene spears were glued together by beach tar. [3] For a long time adhesives were limited to naturally occurring ones like the collagen harvested by boiling animal bones or tissue. In the 1930s the adhesive industry was revolutionized by the advent of polymer science. Synthetic adhesives like epoxy and later polyurethane were developed and started to replace welding or mechanical fasting. Today nearly all objects we use on a day to day basis contain glue, from our mobile phone to credit cards or cars. The advantages of adhesives are the large available variety with different properties, the low price, the new techniques to precisely glue very small objects of different materials and the low weight in conjunction with new materials. This is especially important when making cars or airplanes more energy efficient.

But there remain challenges to the use of adhesives. There is the need to prepare clean and dry surfaces. Often time, pressure or heat is needed for curing. Another challenge is the long term stability. Most adhesives rely on a large number of covalent bonds that once broken cannot form anew. Large effort is made to develop self-healing adhesives were bonds once broken can form again. [4] Some of this research is focused on studying adhesion in nature and adapting the principles to synthetic materials. [5] While the human adhesive industry is quite young, nature had millions of years of trial and error to find solutions for adhesive problems. Examples range from spiders to geckos or marine organisms. [6] Especially interesting is how the mytilus edulis blue mussel is able to cling to diverse surfaces like rocks or ship hulls during adverse conditions namely the wet basic environment and high drift forces. It has been found that the mussel foot proteins are rich in dopa [7], a post-translational modification of tyrosine. This lead to the discovery that the catechol group contained in dopa can reversibly bind to oxide surfaces and withstand forces nearly as well as covalent bonds. [8] Therefore it is a promising approach to add catechol as a functional group to polymer architectures which could be utilized as underwater adhesives, as surface coatings or as biomedical adhesives.

While understanding adhesion in nature can help finding solutions to technical challenges it is also important to understand the adhesion mechanisms inside our own bodies. Adhesion

is on one hand important for platelets in the blood to stick to an injured vessel with the help of the protein von Willebrand factor but on the other hand inappropriate platelet adhesion to the cell wall can lead to thrombosis. [9] Therefore adhesion has to be finely regulated in many parts of our body and it is important to understand in which ways and under what circumstances cells and proteins can adhere. An especially important group of proteins involved in adhesion are the membrane proteins. Integral membrane proteins make up about 20-30% of all proteins encoded in human DNA [10] but about 60% of modern drugs target membrane proteins since they are essential for cell signaling and transduction. [11] The group of peripheral membrane proteins phospholipase A2 for example is considered as target for anti cancer [12] and anti atherosclerosis [13] drugs. There are indications that inhibition of phospholipase A2 alters cell growth and that phospholipase A2 is observed in the synovial fluid of the joints of arthritic patients. [12,14] But still there are many open questions about the molecular mechanisms of the larger number of diverse phospholipases A2.

To be able to systematically develop synthetic biomimetic adhesives or selectively targeted drugs it is important to understand the adhesion mechanisms on a molecular level. Therefore single molecule force spectroscopy experiments which allow to measure forces on the piconewton scale in physiological conditions are an important tool. Here single molecule force spectroscopy (SMFS) experiments were performed with the atomic force microscope (AFM). An AFM tip was functionalized with covalently attached biomolecules and forces were measured between the single biomolecules and surfaces in aqueous solution.

First polyhomopeptides were desorbed from hydrophobic self assembled monolayers to gain an understanding of the dynamics of polymer adhesion on solid surfaces. For this well defined system all relevant kinetic parameters could be determined.

Based on these findings more complex systems were studied as follows.

First solid substrate were replaced by zwitterionic phospholipid bilayers. This setup serves as a simple model system to understand the role that the affinity of the different amino acids for the zwitterionic bilayer plays in the adhesion of peripheral membrane proteins. To study an even more biological relevant system, in a next step experiments with a peripheral membrane protein, the enzyme phospholipase A2, were performed on the zwitterionic bilayer. Those experiments highlight the important role that aromatic residues play in the adhesion of proteins to zwitterionic membranes.

As mentioned before it is not only important to understand adhesion in nature but also to develop new biomimetic materials by taking advantage of existing biological adhesion mechanisms. The extraordinary strength of the catechol titanium dioxide bond and its ability to reform after breaking are very promising and have garnered wide interest in the research

community. Still a lot of questions about the adhesion mechanism of catechol remain. Here the adhesion of the catechol group under different conditions to a metal oxide surface is studied in single molecule experiments. Furthermore experiments with hyperbranched polyglycerol functionalized with different amounts of catechol groups were performed. We investigated their multivalent binding which makes them good candidates for coatings.

# 2 Fundamental principles

## 2.1 Polymer models

Polymers are macromolecules that consist of many repeating subunits. Biological examples are polypeptides, polysaccharides or polynucleotides. Synthetic polymers are used in diverse products such as polyester in textiles or polyethylene for plastic bags. Polymers can consist of just one type of monomer or they can consist of different monomers for example as blockcopolymers. The architecture can range from linear polymers to brush polymers, dendronized polymers, star shaped polymers or dendrimers. This chapter will focus on polymer models for linear polymers.

### 2.1.1 Worm like chain and freely jointed chain

The simplest model for a linear chain is an ideal chain. For an ideal chain it is assumed that there is no interaction between non-neighboring monomers even if they are close to each other in space. There are different ideal chain models that differ in the assumptions they make about torsion and bond angles between the monomers.

**Freely jointed chain**

The freely jointed chain (FJC) model assigns the chain an effective fixed bond length called Kuhn length and the angles between two Kuhn segments are randomly assigned and equally likely. The Kuhn segment itself is treated as an inflexible rod. [15] The root mean square end-to-end distance $R_0$ of a FJC is

$$R_0 = aN^{\frac{1}{2}} \tag{2.1}$$

where *a* denotes the Kuhn length and *N* the number of Kuhn segments. The contour length $L_c$ of the FJC can be expressed as

$$L_c = aN \tag{2.2}$$

**Worm like chain**

The worm like chain (WLC) model is a model for relatively stiff polymers for which the assumption of small bond angles is valid. In contrast to the FJC model the WLC model has a continuous flexibility, whereas the Kuhn segments in the FJC model are inflexible rods. The persistence length is a measure for the length of a segment of the chain in which the

monomers are still correlated in their orientation. This means a higher persistence length indicates a stiffer polymer. The persistence length $l_p$ corresponds to half the length of a Kuhn segment *a*.

$$2l_p = a \tag{2.3}$$

If the chain is stretched by a force the relation between end-to-end distance D and force f for a FJC can be expressed as [15]

$$\frac{D}{L_c} = \coth\left(\frac{fa}{k_B T}\right) - \frac{k_B T}{fa} \tag{2.4}$$

For the WLC model there is no analytical solution but an approximation [16]

$$\frac{f l_p}{k_B T} \cong \frac{D}{L_c} + \frac{1}{4(1 - D/L_c)^2} - \frac{1}{4} \tag{2.5}$$

$k_B T$ denotes the Boltzmann constant times the temperature.

### 2.1.2 Extended models

While the worm like chain and freely jointed chain are successful in describing the chain stretching under force in the low and middle force regime, for high forces the observed experimental behavior diverges from the simple models. The aforementioned models only treat the entropic elasticity of the chain. But when forces approach the nanonewton range chemical bonds and angles will be deformed before they break. This can be described as an additional contribution to the equations by a hookean spring term with the elasticity per monomer $K_S$. [17]

$$\frac{D}{L_c} = \coth\left(\frac{fa}{k_B T}\right) - \frac{k_B T}{fa} + \frac{f}{K_S a} \tag{2.6}$$

$$\frac{f l_p}{k_B T} \cong \frac{D}{L_c} + \frac{1}{4(1 - D/L_c)^2} - \frac{1}{4} - \frac{f}{K_S l_p} \tag{2.7}$$

Deviations from those models also occur when there are conformational changes in the chain during the stretching. A well known example is the B-S transition of double stranded DNA. [18] Furthermore polyethylene glycol (PEG) often used as linker molecule undergoes a force induced transition between an α-helix and a planar conformation in aqueous environment. When PEG is used as a linker molecule the conformational transition has to be

included in the polymer model. The ratio of population of the monomers in helical or planar conformation is Boltzmann distributed with the Gibbs free energy $\Delta G$. $L_p$ and $L_h$ denote the contour length per monomer in planar and helical conformation. [19]

$$D = N\left(\frac{L_p}{e^{-\Delta G/k_BT}+1}+\frac{L_h}{e^{+\Delta G/k_BT}+1}\right)\left(\coth\left(\frac{fa}{k_BT}\right)-\frac{k_BT}{fa}\right)+\mathrm{N}\frac{\mathrm{f}}{\mathrm{K_S}} \qquad (2.8)$$

The Gibbs free energy changes with force as follows:

$$\Delta G = \Delta G_0 - f(L_p - L_h) \qquad (2.9)$$

with $\Delta G_0$ the Gibbs free energy at zero force.

### 2.1.3 Rouse Model

The Rouse model was the first molecular model to describe polymer dynamics. The Rouse model is based on a chain with $N$ segments of length $a$. Instead of stiff rods like in the FJC those segments are beads interconnected with springs of length $a$ representing the entropic restoring force of the chain. Each bead experiences its own independent internal friction with friction coefficient $\zeta$. The diffusion coefficient of the center of mass of the chain follows as [15]:

$$D_R = \frac{k_BT}{N\zeta} \qquad (2.10)$$

The characteristic time the polymer needs to diffuse a distance of the order of its size $R$ is called Rouse time: [15]

$$\tau_R = \frac{R^2}{D_R} = \frac{\zeta}{k_BT}NR^2 \qquad (2.11)$$

## 2.2 Intermolecular forces and bonds

Our understanding of nature on a fundamental level is based on four distinct types of forces. The strong and weak interactions are short ranged and act between elementary particles and are of relevance to nuclear and high energy physics. Gravitational interactions between masses is weak but has an infinite range, is always attractive, determines the movement of matter in the universe and makes earth inhabitable. The electromagnetic interactions are the

basis of all intermolecular forces. In principle to correctly and comprehensively describe intermolecular forces one would have to solve the Schrödinger equation for all electrons in the system and compute the forces from electrostatic theory. Since solving the Schrödinger equation for more than one atom is unpractical, intermolecular forces are grouped together in categories and described separately. [20] Van der Wall's forces are forces between dipoles, electrostatic interactions are forces between charged particles described by Coulombs law. Covalent bonds are based on the sharing of an electron pair between atoms or in quantum mechanics vocabulary are based on overlapping orbitals. Hydrogen bonds are bonds between electronegative atoms (0, N, F, Cl) and H atoms covalently bound to another of those electronegative atoms. Hydrogen bonds (5-10 $k_BT$) are stronger than one would suspect from van der Waals (1 $k_BT$) interactions but weaker and less directional than covalent bonds (100 $k_BT$). The hydrophobic interaction is not a direct force between two hydrophobic particles but an indirect result of the waters tendency to preserve its hydrogen bonds. [20]

### 2.2.1 Electrostatic forces

Electrostatic forces occur between charged particles. The size and direction of the force between two charged particles is described by Coulombs law

$$F(r) = -\frac{Q_1 Q_2}{4\pi\varepsilon_0\varepsilon_r r^2} \tag{2.12}$$

where $Q_1$ and $Q_2$ denote the two charges and $\varepsilon_0$ and $\varepsilon_r$ are the dielectric permittivity constant of vacuum and the relative permittivity of the medium respectively. The force decays with the square of the distance similar to the gravitational force. But unlike the gravitational force it can be attractive or repulsive depending on the sign of the charges. Unlike charges attract each other and like charges repel each other. This is the reason that in practice the electrostatic force has a smaller range than the gravitational force despite the same dependence on distance *r*. Additional charges in mediums like salt containing buffer or ion crystals lead to an effective screening of electric fields. [20]

### 2.2.2 Van der Waals forces

In contrast to the electrostatic interaction Van der Waals forces are forces between uncharged molecules. But even if a molecule has a zero net charge it is possible that the charges are not uniformly distributed across the molecule. This happens for example if an atom in a molecule has a higher electronegativity (draws the electrons stronger) than its

bond partner atom. Such molecules have a permanent dipole and are called polar. The dipole moment *u* of a molecule is defined as

$$u = ql \tag{2.13}$$

Where *q* is the charge and *l* the distance between the charges (+*q* and –*q*). Even if a molecule is nonpolar and has no permanent dipole moment the electron distribution fluctuates in the molecule over time. This means that it can have a nonzero dipole moment at a certain time. This then leads to a temporary electric field and the charges in neighboring nonpolar molecules are rearranged according to the electric field. In the second molecule a dipole is induced by the field and there is an attractive interaction between the two nonpolar molecules. The strength of the induced dipole dependence on the polarizability *α* of the molecule defined as follows:

$$u_{ind} = \alpha E \tag{2.14}$$

$u_{ind}$ is the induced dipole moment and *E* the electric field. There are three contributions to the Van der Waals interaction:

- The Keesome interaction between two permanent dipoles

$$E_K = -\frac{u_1^2 u_2^2}{3kT(4\pi\varepsilon_0\varepsilon_r)^2 r^6} \tag{2.15}$$

- The Debye interaction between a permanent dipole and an induced dipole

$$E_D = -\frac{2u^2\alpha}{(4\pi\varepsilon_0\varepsilon_r)^2 r^6} \tag{2.16}$$

- The London dispersion interaction between two nonpolar molecules

$$E_L = -\frac{3\alpha^2 h\nu}{4(4\pi\varepsilon_0\varepsilon_r)^2 r^6} \tag{2.17}$$

Here *h* is the Planck constant and *v* the electronic adsorption frequency.

### 2.2.3 Covalent bonds

Covalent bonds between atoms are characterized by the sharing of electron pairs. In the classical covalent bond each atom donates one electron and then both electrons are shared by the two atoms. Atoms can form several bonds according to their valency. It is also possible that multiple covalent bonds are formed with one partner atom if more than two electrons are shared between the two atoms. Coordinate bonds are covalent bonds where both shared electrons are donated from one atom. Covalent forces are of short range (0.1-0.2 nm) and they are highly directional. They are quite strong at about 100 $k_BT$. [20]

### 2.2.4 Coordination complex

A coordination complex consists of a usually metallic center ion and the surrounding bound molecules or ions which are called ligands. In the past it was assumed that complexes are held together by weak chemical bonds but the understanding today is that coordinate bonds are in fact covalent and quite strong. The central ion acts as a Lewis acid or a electron pair acceptor while the ligands are electron pair donors (Lewis base). The coordination number of the central ion is the number of attached donor atoms. A monodentate ligand is a ligand which has only one donor atom. Polydentate ligands have several donor atoms that can coordinate to different sites on the center ion. [21]

### 2.2.5 Hydrophobic interaction

Water molecules are polar molecules and have the ability to form hydrogen bonds between the electronegative oxygen and the hydrogen of another water molecule. Since the oxygen has two pairs of available electrons and each water molecule has two hydrogen atoms, one molecule can bond to up to four other molecules. The hydrogen bonding is the reason for waters unusually high boiling point for such a small molecule. The intermolecular distance of a water hydrogen bond is 0.176 nm. Less than what is expected of Van der Waals interaction (0.26 nm) but longer than a covalent O-H bond (0.1 nm).

The hydrogen bonds are energetically very favorable. When a nonpolar molecule or surface comes into contact with water, it is still energetically favorable to preserve most of the hydrogen bonds between water molecules by re-orientating the water molecules in the vicinity of the nonpolar molecule. This hydrophobic solvation leads to a more ordered conformation with a loss in entropy. This is the reason for the low solubility of nonpolar molecules in water as well as the dewetting tendency of water to minimize contact area to nonpolar surfaces.

Between hydrophobic molecules and surfaces in water a strong attraction can be observed. It was originally proposed that this is some sort of hydrophobic bond. But it is not a bond as such but a rearrangement of the overlapping solvation zones of the hydrophobic particles. In this sense the hydrophobic interaction is mainly an entropic phenomenon. [20]

### 2.2.6 Adhesion and interfacial energy

The work of adhesion is defined as the work needed to separate unit areas of surfaces from contact to infinity in vacuum. If the surfaces are identical the term is cohesion instead of adhesion. Adhesion is the sum of different interactions like covalent bonds, electrostatic interactions, Van der Waals interactions, hydrogen bonds or steric interactions. Separating to bodies A and B requires work to create the two surfaces with surface energy in vacuum γ. Separating to bodies A and B in a solution C can be understood as creating surfaces A and B in vacuum and bringing surfaces A and B in contact with C from the vacuum. This can be expressed in the Dupre equation:

$$W_{ABC} = W_{AB} + W_{CC} - W_{AC} - W_{BC} = \gamma_{AC} + \gamma_{BC} - \gamma_{AB} \tag{2.18}$$

where $\gamma_{AB}$ denotes the interfacial energy between medium A and B. This formalism can also be used to describe the wetting of surfaces, solid (S), with a liquid (L) in a gas phase (G) in the Young and Young- Dupre equations with the equilibrium contact angle Θ: [20]

$$\gamma_{SL} + \gamma_{LG}\cos\,\theta = \gamma_{SG} \tag{2.19}$$

$$\gamma_{LG}(1 + cos\theta) = W_{SLG} \tag{2.20}$$

## 2.3 Bonds under force

Understanding molecular binding and unbinding transitions is important for all chemical reactions. In the 1940s Kramer developed a reaction rate theory that is still in use today. The bond is understood as a local free energy minimum. For unbinding an energy barrier has to be overcome. Kramer treated this escape as a diffusive flux of the thermalized states undergoing Brownian motion. Kramer calculated the rate of escape of an overdamped particle as:

$$k = \frac{\sqrt{\kappa_0 \kappa_b}}{2\pi\eta} e^{-\Delta U/k_B T} \tag{2.21}$$

Where $\kappa_0$ is the curvature of the energy landscape at the bound state, $\kappa_b$ the curvature of the energy landcape at the barrier, $\eta$ the damping coefficient and $\Delta U$ the energy difference between bound state and the barrier. [22]

### 2.3.1 Bell Model

Bell studied how the transition rate changed with an external force perturbating the energy landscape. He described that the force tilts the energy landscape along the reaction coordinate *x*. When a sufficiently large force is applied the energy minimum vanishes. This is the case for $f = \frac{\Delta U}{x_\beta}$, where $x_\beta$ is the distance between the bound state and barrier. The lifetime $\tau$ respectively the transition rate *k* can be described as:

$$\tau = \tau_0 e^{(\Delta U - x_\beta f)/k_B T} \tag{2.22}$$

$$k = k_0 e^{(x_\beta f)/k_B T} \tag{2.23}$$

$$k_0 = A e^{-\Delta U/k_B T} \tag{2.24}$$

where *A* is the attempt frequency and $\tau_0$ the inverse attempt frequency. [23]

### 2.3.2 Loading rate dependence

For experiments of constant force the mean lifetime of a bond can be described as in equation (2.22). In a lot of experimental setups the force is not constant but varies with time. The change of the force in time is called loading rate $r_F$. The transition rate *k(F)* as described in (2.23) itself is independent of the loading rate or the force history of the bond it depends

only on the instantaneous force. But the probability that the system is still in the bound state at a certain time depends on the force history and thus on the loading rate. Here it becomes important how the force is applied to the bond. In AFM (atomic force microscope) experiments the force is applied via a soft cantilever with a spring constant $\kappa_c$ . Furthermore there are typically biomolecules and chemical linkers between the cantilever tip and the bond that have nonlinear loading dynamics. See chapter 2.1 for details.

$$\frac{d}{dt}p_{on}(t) = -k_{off}(t)p_{on}(t) \tag{2.25}$$

For a force ramp with the substitution $\frac{1}{r_F}dF = dt$ and $p_{on}(0) = 1$ one can calculate the probability to remain bound up to the force *f* as:

$$p_{on}(f) = exp\left[-\frac{1}{r_F}\int_0^f k_{off}(f)df\right] \tag{2.26}$$

The most probable rupture force $f^*$ is then determined by $\frac{dp_{on}(f)}{df} = 0$

$$k(f)|_{f^*} = r_F \frac{dlnk(f)}{df}\Big|_{f^*} \tag{2.27}$$

for the Bell model (2.23) this gives

$$f^* = \frac{k_B T}{x_\beta} ln\left[\frac{r_F x_\beta}{k_0 k_B T}\right] \tag{2.28}$$

With flexible linkers the loading rate will not be constant during the experiment but it itself will be a function of force. [24]

### 2.3.3 The rebinding rate

The simple Bell model is a two state model with an unbinding rate *k(F).* The rebinding rate is assumed to be zero. If rebinding is considered, the model evolves to a two state process with time dependent rates:

$$\frac{d}{dt}p_{on}(t) = -k_{off}(t)p_{on}(t) + k_{on}(t)p_{off}(t) \tag{2.29}$$

$$\frac{d}{dt}p_{off}(t) = k_{off}(t)p_{on}(t) - k_{on}(t)p_{off}(t) \tag{2.30}$$

with the probabilities at time zero $p_{on}(0) = 1$ , $p_{off}(0) = 0$ and $p_{on}(t) + p_{off}(t) = 1$.

If the system is driven slow enough that equilibrium can be assumed the equations (2.29) and (2.33) simplify to:

$$k_{off}(t)p_{on}(t) = k_{on}(t)p_{off}(t) \tag{2.31}$$

This is the principle of detailed balance. The number of transitions per unit time from one state to the other and vice versa are equal.

The rebinding rate is suppressed for systems far from equilibrium (e.g. high loading rate) or if a soft linker molecule is used. [25]

### 2.3.4 Multiple Bonds under force

Multivalency is common in nature were multiple ligands enhance binding between molecules or cells. Multiple bonds are ideally arranged in series or parallel.

Multiple uncorrelated bonds in parallel carry only the Nth part of the force. The lifetime of the multiple bond cluster can be seen as sum of lifetimes for each step in the unbinding pathway *N* to *N-1* and so forth. The rate of transition from *N* to *N-1* bonds is enhanced compared to a single bond by the increased number of bonds available for unbinding.

$$k_{N\to N-1}(f) = Nk_0 exp\left[\frac{fx_\beta}{Nk_BT}\right] \tag{2.32}$$

The failure of the first bond will increase the load on the remaining bonds. For fast loading rates the remaining bonds will fail soon after. So the rupture force of *N* bonds in the kinetic regime of fast loading rates is less than *N* times the rupture force of one. On the other hand in the equilibrium regime when the loading rate is small at each step there is finite probability of rebinding. That can lead to strong enhancement in lifetime of the multiple bonds compared to a single one.

In the case of bonds arranged in series the bonds feel the full force. Examples of bonds arranged in series are the monomers of a macromolecular chain held together by bonds or domains in a protein that unfold under force. The unbinding rate is enhanced by the number of bonds that means a series of *N* bonds fails faster than a single bond. [25]

$$k_{N\to N-1}(f) = Nk_0 exp\left[\frac{fx_\beta}{k_B T}\right] \tag{2.33}$$

Data taken under most experimental conditions are harder to interpret as the above discussed cases imply. In most cases the partition of the force and the degree of cooperativity among the binding sites is unknown.

### 2.3.5 Determining Bond valency

Determining the bond valency of an AFM experiment is important in correctly interpreting the results. In some cases the valency of an interaction is apparent in the force-distance trace of an AFM experiment for example if the force drops to zero in a stepwise manner. But sometimes this is not readily apparent.

In a lot of AFM force spectroscopy measurements it is desired that a single molecule is measured. This is achieved by diluting the available molecules or binding sites. Experimental setups either bond the probe molecules directly to the tip or spread them on the surface and pick them up with the tip. In both cases it is important to limit the number of possible binding sites. If Poisson statistic are assumed the number of curves with interaction events ($N_e$) compared to the total number of collected curves ($N_{tot}$) give an estimate on how probable it is to measure single molecule events: [25]

$$\frac{N_1}{N_e} = \left(\left(\frac{N_e}{N_{tot}}\right)^{-1} - 1\right) ln\left(\frac{1}{1 - N_e/N_{tot}}\right) \quad (2.34)$$

So according to Poisson statistics when only 10% of the measured curve give adhesion events then the probability that those are single molecule events is 94.8%. For 20% the probability is 89%, for 50% events 69%, for 90% 25.6%. Poisson statistics are more accurate for a low probability of bond formation.

Getfert et al. [26] studied hidden multiple bonds in AFM force spectroscopy experiments by comparing a numerically solved model with experimental data. The model includes probe molecules covalently attached to the tip ($R$=15nm) via linkers ($l$=30nm). The number of linkers on the tip is varied as is the density of acceptors on the surface. The linker is treated as freely jointed chain and rupture probabilities are calculated following Evans and Ritchie. [24] It is not assumed that the force is equally distributed to each bond since the acceptors on the surface have slightly different distances from the tip. It is assumed that two bond that rupture closer together than 1nm cannot be experimentally distinguished from a single bond. They find that about 40-50% of the multiple bonds cannot be distinguished from single ones. This percentage of course would be lowered when polydisperse linkers or biomolecules would be used. This would lead to even larger variations on how the force is distributed and at which point the ruptures occur. Interestingly they find that the hidden multiple bonds do not form separate peaks in the force distribution, they also do not distort the most probable force for single bond events but they add to the long tail of the force distribution. This means that in most cases the most probable force of a force histogram corresponds to the single events and the amount of hidden multiple bonds can be approximated by looking if the force distribution has a long tail.

## 2.4 Protein membrane interactions

A biological membrane is a selectively permeable barrier. The membrane that encloses the cell is called plasma or cytoplasmic membrane but other membranes also define separate compartments within the cell. A biological membrane consists of a lipid bilayer and embedded membrane proteins. It serves as the attachment surface of the intercellular cytoskeleton and extracellular structures such as the glycocalyx. In this the plasma membrane helps to give the cell a shape and to form tissue when attaching to the extracellular matrix. The selective permeability of the membrane maintains and regulates a biochemical environment inside the cell that differs from the outside and even larger molecules can be transferred across the membrane. Cellular processes such as cell signaling and membrane trafficking involve highly complex interactions of lipids and proteins in the membrane. [27]

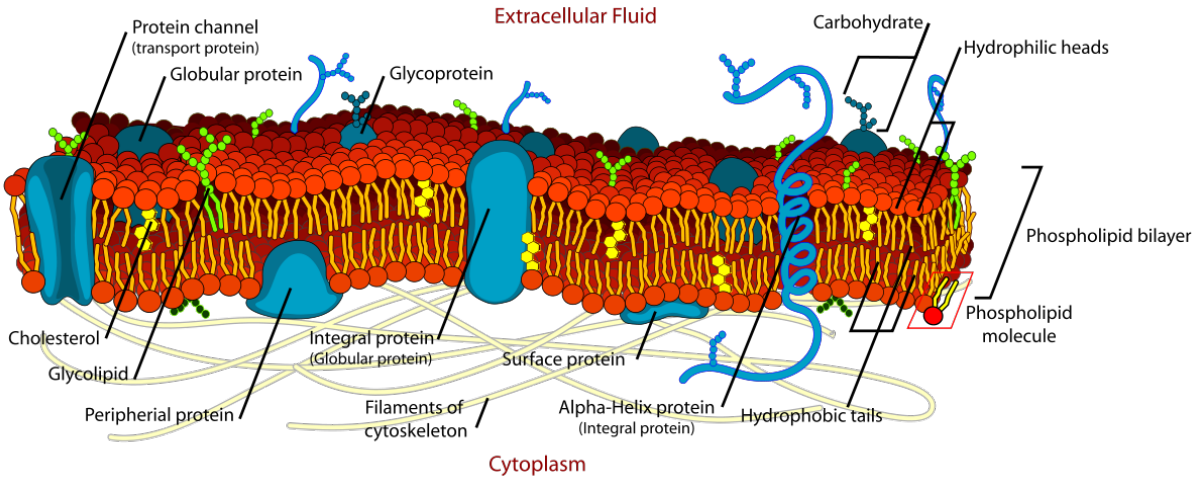


**Figure 2.1:** shows a schematic of a plasma membrane. It mostly consist of a bilayer of phospholipids together with some other lipids like cholesterol and integral and peripheral membrane proteins. On the inside of the cell the cytoskeleton is attached to the membrane, on the outside glycoproteins and glycolipids are shown where the glycocalyx polysaccharides can attach. Image by LadyofHats Mariana Ruiz Licensed under Public domain/Wikimedia Commons.

### 2.4.1 Lipid bilayer

Lipids are naturally occurring amphiphatic molecules which contain hydrophobic and hydrophilic parts. Sterols like cholesterol, fatty acids, mono-, di- or triglyceride, glycerophospholipids or even some vitamins are all lipids. The main component of eukaryotic plasma membranes are glycerophospholipids. Other lipid components are cholesterol or sphingomyelin. Glycerophospholipids consists of a glycerol with two fatty acid chains and one phosphoric acid attached as esters. In the mammalian plasma membrane most of the phospholipids have a zwitterionic phosphate headgroup such as phosphatidylcholine (PC) or

phosphatidylethanolamin (PE) but there are also some charged phospholipids present such as phosphatidylserine (PS) and phosphatidylinositol (PI). There is an asymmetry in the composition of lipids in the inner or outer part of the bilayer. Most of the charged PS lipids are contained in the inner part of the lipid bilayer facing inward to the cell. The fatty acid chains can differ in their length and in their saturation. This can affect the fluidity of the membrane since unsaturated double bonds introduce “kinks” in the chain that affect the packaging of the chains. [28]

Lipids can assemble spontaneously to supramolecular structures depending on the parameters like water content, salt concentrations and temperature. In aqueous solutions the hydrophobic effect makes it energetically unfavorable for the hydrophobic tails of the lipids to be exposed to the water. The resulting structures can be grouped as different phases. In biological membranes the lipids assemble in a lamellar structure of two layers facing each other. At low temperatures the lipid is in an ordered gel phase and at temperatures above the transition temperature the lipids are in a fluid state. The transition temperature depends on the length and saturation of the sidechains as well as the headgroup. [20]

The first modern model of the plasma membrane was that of a fluid mosaic developed by Singer and Nicholson in 1972. [29] The bio membrane is treated as a 2D viscous fluid with the functionality added by membrane proteins that freely diffuse and that are laterally homogenous. This model was revolutionary in the sense that it diverged from the picture that bio membranes are mainly static. But with today’s knowledge the fluid mosaic model has to be amended. The functionality is not only provided by the membrane proteins but can also be influenced by the local lipid composition and mechanical properties of the membrane. Furthermore the idea that the distribution of lipid composition and membrane proteins is homogenous across the membrane is not accurate. The plasma membrane has a complex lateral structure and has local inhomogenities like lipid rafts or protein microdomains. [30]

The plasma membrane is a highly complex system. To better understand certain aspects of protein membrane interactions it can be helpful to study much simpler model systems. The simplest system would be to not include any membrane proteins and just use one lipid or a mix of a few lipids for the lipid bilayer. For the use of experimental techniques that are surface sensitive such as total internal reflection microscopy (TIRF), surface plasmon resonance (SPR) or atomic force microscopy (AFM) it is useful to prepare a lipid bilayer on a solid support surface as supported lipid bilayer (SLB). The lipid bilayer can be assembled through vesicle fusion on hydrophilic surfaces such as mica.

### 2.4.2 Membrane proteins and their adhesion mechanisms

There are a large number of different membrane proteins and they have diverse strategies of adhering to the membrane. Membrane proteins can be grouped into integral membranes that are permanently attached to the membrane and peripheral membrane proteins that reversibly attach to the membrane. Most integral membranes are transmembrane proteins spanning the whole bilayer. They form α-helices or β-sheets inside the bilayer and utilize hydrophobic matching. That means that they expose hydrophobic side chains to the hydrophobic core of the bilayer and hydrophilic side chains to the headgroups and the water layer. [28]

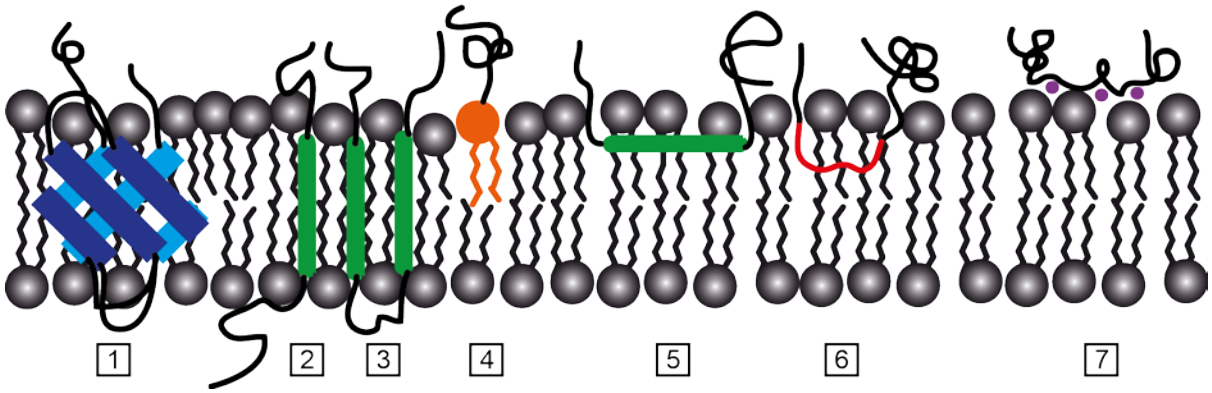


**Figure 2.2:** Different binding strategies of proteins to membranes are illustrated. 1, 2 and 3 depict representations of different integral transmembrane proteins adhering with the help of incorporated ß-sheets (1) or α-helixes with single (2) or multiple (2) passes. 4 is a schematic of an attachment of a peripheral membrane protein via a bound lipid. Peripheral protein 5 has an amphiphatic α-helix incorporated parallel into the membrane. In case 6 the protein extend hydrophobic loops into the membrane and in 7 a protein electrostatically interacts with a charged membrane with the help of divalent ions.

Peripheral membrane proteins use a variety of ways to attach to the membrane. Some are bound to lipids that can be incorporated into the membrane, others extend loops into the membrane or have an amphiphatic secondary structure that can be immersed parallel into the membrane. Some have specialized binding domains that for example bind to lipid second messengers such as dyacylglycerol. Which kind of attachment occurs depends also on the lipid composition. If the bilayer contains a large fraction of charged anionic lipids such as PS, cationic residues of the membrane proteins can attach to the surface via electrostatic interaction. Sometimes the electrostatic interaction is mediated by bound divalent ions like $Ca^{2+}$. The attachment process can be orchestrated in several stages like first attachment by electrostatic interaction followed by insertion of a hydrophobic loop or a binding pocket. Sometimes the surface or $Ca^{2+}$ has to induce a conformational change that makes insertion possible. If the membrane is mainly zwitterionic like the outer plasma membrane, amino acids with aromatic residues like tyrosine and tryptophan play a major role in the attachment since they have the highest affinity of all residues for the interfacial region. [27] The reasons for

this are not yet fully understood but hydrophobic attraction, hydrogen bonds and π-interactions of the aromatic rings are thought to contribute. [31,32]

### 2.4.3 Phospholipase A2 – membrane interactions

The phospholipases A2 are a family of enzymes that can catalyze the hydrolysis of phospholipids. They are named A2 since they catalyze the hydrolysis of the middle sn2 ester bond. The products are free fatty acids and lysophospholipid. There are numerous phospholipases A2 that can again be sorted into different categories. The secreted phospholipases A2 called sPLA2 are of relatively small molecular weight (13-15 kDa), have a number of disulfide bonds, a catalytic histidine and a $Ca^{2+}$ bound in the active center. [33] They need a mM concentration of $Ca^{2+}$ to catalyze the hydrolysis. While $Ca^{2+}$ is needed for hydrolysis, it was shown that binding to the phospholipid membrane did not depend on $Ca^{2+}$. [34] They are put into different groups. Group IA contains phospholipases from cobra and krait venom, IB from mammal pancreas. The sPLA2 from honey bee venom is placed into group III. This sPLA2 is special since it is the least genetically related to the other sPLA2s. [35] Group IV consists of unrelated cytoscolic 85 kDa phospholipase A2 (cPLA2).

It has been found that the active center of sPLA2s is surrounded in the folded structure by a flat planar surface covering approximately 1500 $Å^2$ consisting of about 20 amino acids. This region is called interfacial binding surface or i-face. When comparing different sPLA2s it has been found that a lot of the interfacial residues are in structurally conserved regions but are not necessarily conserved in amino acid sequence. [36] The residues that are present on the interfacial binding surface influence the affinity of the sPLA2s to the different phospholipids. The interfacial binding surface of honey bee venoms sPLA2 is compromised mainly of hydrophobic residues and the affinity for zwitterionic PC membranes is much higher than for anionic PS membranes. [37] On the other hand human group IIA sPLA2 interfacial binding surface is highly charged as it contains many cationic residues. It was found that it has a high affinity for the anionic POPG over PC vesicles. Interestingly the difference was much more pronounced for the rate of association than for the rate of dissociation. This supports the assumption that electrostatic interactions are mainly important for membrane association. Acid PLAs from cobra venom have a high activity on PC membranes thought to originate from aromatic residues on the interfacial binding surface especially Trp61. Mutating the tryptophan at position 61 resulted in a 150 fold reduction in PC affinity influencing both association and dissociation rate. This indicates that aromatic residues accelerate the zwitterionic membrane adsorption and elongate the membrane residence time. [34]

The functions of sPLA2s include dietary phospholipid digestion (sPLA2 group IB in the human pancreas), host defense against gram positive bacteria (human group IIA sPLA2) and their activity has been observed in a variety of inflammatory diseases like rheumatoid arthritis, psoriasis, sepsis, pancreatitits and cancer. But their exact role in the inflammatory diseases is yet unclear. A recent study found that while sPLA2 group IIA is pro-inflammatory in arthritis, group V sPLA2 has an anti-inflammatory function. [38]

## 2.5 Mussel based biomimetic adhesive

While under water glues are still a challenge for industrial adhesive development, mussels have found a way for strong and long term adhesion to wet surfaces. Wet hydrophilic surfaces are difficult for glues since any adhesive will have to compete with the surface water layer. Mussels can not only adhere to metal oxides like ship hulls or mineralic surfaces like rocks, they do so despite large tidal forces. Studying how mussels adhere gives the chance to adapt certain principles for the development of industrial coatings and biomedical adhesives.

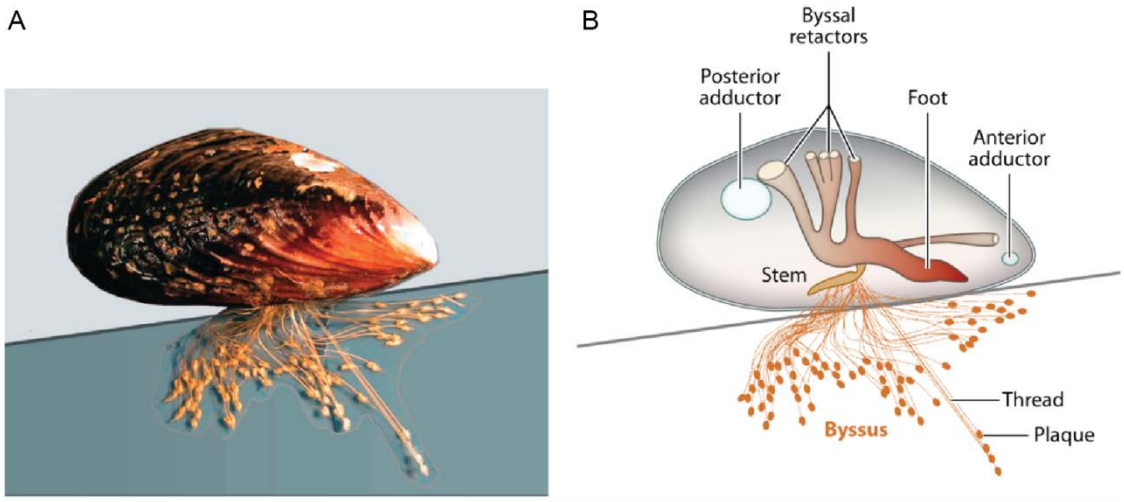


**Figure 2.3:** A shows the marine mussel *Mytilus californianus* attached to a mica surface and B a schematic of the adhesion with byssus. Each byssus is a bundle of threads tipped with adhesive plaques. Adapted from [39]

Mussels adhere to surfaces via with their byssus, a bundle of threads with adhesive plaque at their end. They are made of protein and contain no living cells. To understand their adhesive properties the proteins in the byssus were studied. The Mytilus byssus contains about 25-30 different proteins but the part that adheres to external surfaces, the byssal plaque contains only 7-8 of which 5 are unique to the plaque. Those are the mussel foot proteins (mfp) 2,3,4,5 and 6. Directly at the contact area mainly mfp 3, 5 and 6 are found. [40,41]

Mfp 3 and 5 are rich in dopa (15-30 mol%). [7,42] 3,4-dihydroxyphenylalanine (dopa) is formed by posttranslational modification of tyrosine. Mfp 6 is rich in cysteins (11 mol%). [41] It has been found that the dopa in mfp 3 and 5 is adhering to the surfaces, while the cystein rich mfp 6 controls the redox balance and can keep interfacial dopa in a reduced state. [40,43] The byssal plaque also shows strong cohesion through crosslinks. The cysteins can crosslink with dopa and the oxidized dopa, the semiquinons can crosslink via radical addition. Furthermore iron chelate complexes of dopa can add to cohesion. [39]

The catechol group of the dopa residues can interact in a number of different ways. The hydroxyl groups can form hydrogen bonds, the aromatic ring can participate in π stacking and the whole catechols can form bidentate coordination complexes via their hydroxyl groups. Dopa can oxidize to quinon or semiquinon form and the quinon can react in different ways most notably the covalent crosslinking via radical addition to another semiquinon. [44]

The adhesion of a single dopa to titanium oxide was studied with AFM force spectroscopy and rupture force of approximately 800 pN were measured. This is a significant part of the 1.4 nN at which the S-Au bond ruptures. [45] Besides the strength of the bond the most interesting feature is that the bonds were found to be reversible. Once broken they can form again. [8]

Since dopa has been identified as the reason for the adhesive properties of blue mussels, the research and development of biomimetic polymers with catecholic groups for different applications like surface coatings or medical adhesives has begun. [39]

# 3 Materials and Methods

## 3.1 Biomolecules

In this thesis the desorption forces of different biomolecule on various surfaces were studied. In order to investigate their properties they were covalently attached to the tip of the AFM cantilever using NHS-ester chemistry. Depending on solubility different reaction buffers were used to conjugate the probe molecule to the tip.

### 3.1.1 Polyhomopeptides

**Poly-L-lysine**

70-150 kDa poly-L-lysine was purchased from Sigma Aldrich. At physiological conditions poly-L-lysine carries a positive charge and is hydrophilic. It was solved in 50 mM sodium borate buffer at pH 8.1 to a concentration of 1mg/ml for functionalization of the tip.

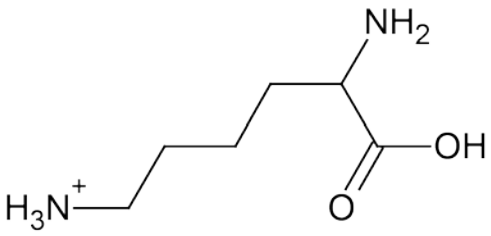


**Figure 3.1:** Chemical structure of a charged lysine monomer.

**Poly-D-tyrosine**

Poly-D-tyrosine was purchased from Sigma Aldrich with the molecular weight 40-100 kDa. Poly-D-tyrosine is an aromatic hydrophobic polymer and is not solvable in water. Poly-D-tyrosine was dissolved in 1 M NaOH to a concentration of 1mg/ml and the buffer was exchanged for 50mM sodium borate buffer pH 8.1 using spin desalting columns (7 kDa MWCO).

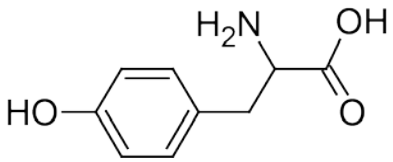


**Figure 3.2:** Chemical structure of a tyrosine monomer.

### Poly-L-glutamic acid

Poly-L-glutamic acid sodium salt was bought from Sigma Aldrich with the molecular weight 50-100kDa. Poly-L-glutamic acid has a negatively charged carboxylate group at physiological pH and is solvable in water. Functionalization was performed using a 1mg/ml solution in 50mM sodium borate buffer at pH 8.1.

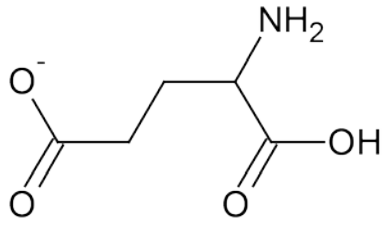


**Figure 3.3:** Chemical structure of a charged glutamic acid monomer.

### Poly-L-tryptophan

Poly-L-tryptophan was bought from Sigma Aldrich with molecular weight 15-50 kDa. It is an aromatic hydrophobic amino acid and was solved at a concentration of 1mg/ml in dry DMSO for functionalization.

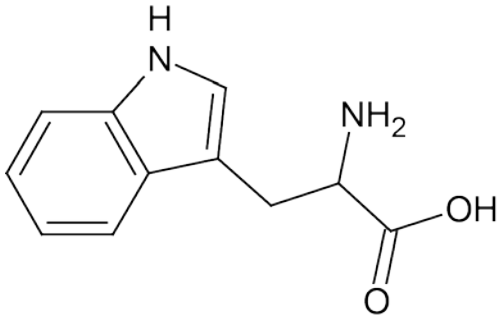


**Figure 3.4:** Chemical structure of a tryptophan monomer.

### 3.1.2 Dendritic Polymers

Hyperbranched polyglycerol (hPG) with Mn≈5000 g/mol and Mw≈7500 g/mol, was polymerized by a one-step ring-opening anionic polymerization, as described in the literature. [46,47] Trimethylolpropane (TMP) was used as the initiator. Amine functionalized hPG was prepared according to previously published procedures. [48] 3,4-Dihydroxyhydrocinnamic acids and acrylic acids were grafted to the amine groups by amide coupling to introduce catechol and vinyl groups, respectively. [49] Different constructs with different numbers of amine and catechol endgroups were prepared by Qiang Wei in the group of Prof. Rainer Haag at FU Berlin including hPG with 12% amine endgroups, hPG with 2% amine groups and 8% catechol groups and hPG with 60% amine groups and 40% catechol groups. Details for the synthesis are found in the Appendix.

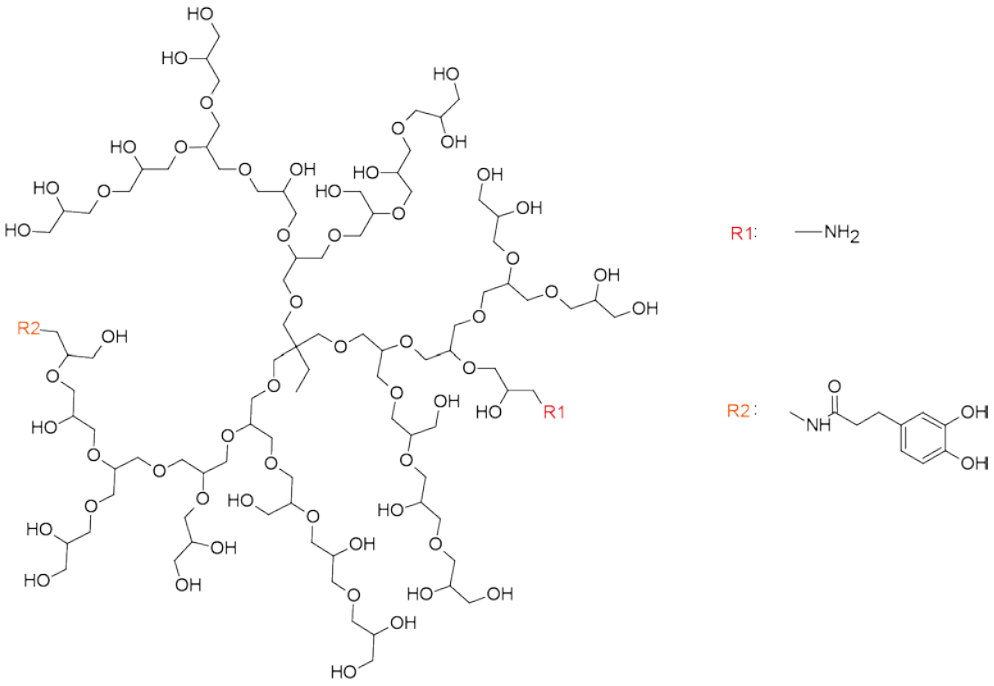


**Figure 3.5:** Schematic of a hyperbranched polyglycerol (hPG). hPGs are functionalized with differing amounts of amino groups (R1) for attachment to the tip and catechol groups (R2) for better adhesion to metal oxides.

### 3.1.3 Phospholipase A2

The phospholipases A2 are a family of enzymes that can catalyze the hydrolysis of phospholipids. They are named A2 since they catalyze the hydrolysis of the middle sn2 ester bond. The products are free fatty acids and lysophospholipids.

**Phospholipase A2 from honey bee venom**

Phospholipase A2 from honey bee venom (Apis mellifera) was bought as lyophilized powder from Sigma Aldrich, Germany. The polypeptide chain contains app. 123 amino acids and seven disulfide bridges. The molecular weight is 14.5 kDa. The secreted phospholipase A2 from honey bee venom is sorted into group III of secreted phospholipases A2 (sPLA2).

**Phospholipase A2 from mozambique spitting cobra venom**

The enzyme phospholipase A2 from mozambique spitting cobra venom (Naja mossambica mossambica) was purchased from Sigma Aldrich as lyophilized powder. Phospholipase A2 from mozambique spitting cobra belongs to group IA of sPLA2s. Both phospholipases A2 were solved at a concentration of 0.3 mg/ml in sodium borate buffer at pH 8.1 for functionalization.

### 3.1.4 Elastin like polypeptides

Elastin like polypeptides (ELP) were prepared by Ali Ghoorchian and James Cole in the group of Nolan B. Holland (Cleveland State University). ELPs with and without the foldon trimerization were synthesized as explained in a previous publication. [50] Construct with sequences MGHK$(GVGVP)_{80}$C and MGH$(GVGVP)_{40}$-Foldon-C were prepared and solved at a concentration of 50 µM in 50 mM sodium borate buffer at pH 8.1 for tip functionalization.

## 3.2 Surface preparation and characterization

Surfaces were prepared and mounted in a home build fluid cell of the AFM. Several small surfaces can be mounted together in one fluid cell. For measurements below or above room temperature special fluid cells can be operated with the Cooler Heater respectively Bio Heater build by Asylum Research (now part of Oxford Instruments).

### 3.2.1 Hydrophobic surfaces

**Self assembled monolayers**

For the preparation of self assembled monolayers (SAMs) gold coated glass slides are incubated in a solution with molecules with thiol endgroups. To receive a hydrophobic surface molecules with thiol groups on one end and methyl groups on the other are chosen.

- Glass slides are sonicated for 15 min in a 2% Hellmanex solution (Hellma GMBH, Germany) and twice in ultrapure water (Biochrom, Germany) and then cleaned with RCA solution (v:v:v: 5:1:1 water, 32% ammonia, 35% hydrogen peroxide, VWR, Germany) at 75 °C for 15 min.
- The slides are coated by a vacuum coater (Edwards GMBH, Kirchheim, Germany) with 10nm chrome-nickel and 100 nm gold and stored in the fridge.
- The gold slides are again cleaned in RCA solution at 75 °C for 15 min and then immersed for 12 h in 2 mM 1-dodecanthiol (Sigma Aldrich, Germany) diluted in ethanol (absolute, >99.9%, Merck, Germany) for the formation of hydrophobic self assembled monolayers (SAMs).
- The slides are rinsed with ethanol and ultrapure water before being dried by nitrogen gas.

**Hydrogen terminated diamond**

A hydrogen terminated diamond was prepared from a 5 mm × 5 mm polycrystalline diamond (Advancing Diamond Ltd, UK) by Andreas Reitinger in the group of Jose Garrido. According to the previously published protocol following steps were performed [51]:

- Heating up to 700 °C in a vacuum chamber pressure of 10mbar
- 100 sccm hydrogen flow
- Plasma 15 min at 50 mbar
- Cooling under hydrogen atmosphere

Hydrogen terminated diamond was sonicated before measurement in acetone followed by isopropanol for 30 minutes each.

**PTFE**

A commercially available polytetrafluoroethylene (PTFE) surface of the size 1cm × 1cm was sonicated before measurement in acetone followed by isopropanol for 30 minutes each.

### 3.2.2 Surface characterization

The SAM surface was imaged in contact mode with OMCL AC240 TS cantilevers (Olympus, Germany) as depicted in Figure 3.6 A. The root-mean-square roughness of this image is 1.7 nm.

The hydrophobicity of surfaces was confirmed with the help of static contact angle measurements. They were carried out with a home-built goniometer equipped with a CCD camera and analyzed with Image J drop analysis plugin. [52] Contact angles between 105 ° and 110 ° were measured for the hydrophobic SAMs. In Figure 3.6 B a droplet with contact angle 109 ° is shown.

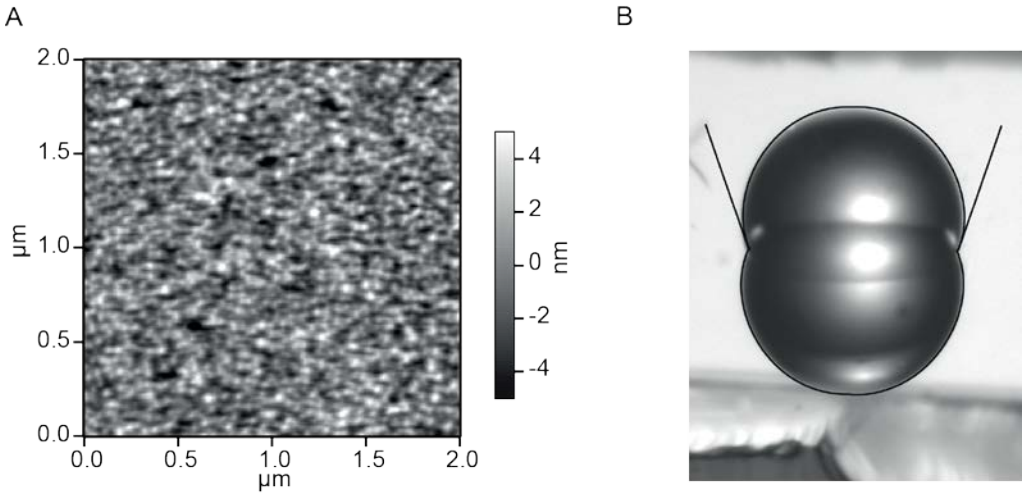


**Figure 3.6:** Surface characterization of a $CH_3$ terminated hydrophobic SAM. A shows an AFM image of a 2 µm × 2 µm area. B depicts a CCD image of a 2.5 µl water droplet on the SAM. The black lines encircling the droplet and its reflection were made with Image J drop analysis plugin. [52,53]

### 3.2.3 Maleimide functionalized glass

Maleimide functionalized glass is prepared so that probe molecules on the tip with cysteins can bin to the surface and be stretched between tip and surface.

- For the surfaces preparation glass slides are sonicated for 30 min in a 2 % Hellmanex solution (Hellma GMBH, Germany) and twice in ultrapure water (Biochrom, Germany)

and then cleaned with RCA solution (v:v:v: 5:1:1 water, 32% ammonia, 35% hydrogen peroxide, VWR, Germany) at 75°C for 15 min and dried in an oven.

- The slides are placed in a oxygen plasma (100W, 0.3mbar, 30min) and afterwards incubated for 10 min in a Vectabond (Axxora, Germany) solution (50 µl Vectabond in 2.5 ml dry acetone) for silanization.
- The slides are rinsed in dry acetone and dry chloroform and then placed in a 3mg/ml solution of SMCC (Succinimidyl-4-(N-maleimidomethyl)cyclohexane-1-carboxylate, Thermo-Fisher, Germany) in dry chloroform for the formation of a maleimide layer.
- They are rinsed with ethanol and immediately used in the AFM measurement.

### 3.2.4 Metal oxides

$SiO_2$ slides were cut from a commercially available silica wafer. Directly before the measurement the $SiO_2$ slides were put in an oxygen plasma (100W, 0.3mbar, 1h, Edwards GMBH, Kirchheim, Germany) and afterwards rinsed with ultrapure water.

$TiO_2$ slides were prepared by Andreas Hartwig at IFAM, Bremen by sputtering titanium on silica wafers as previously published. [49] The sputter process was performed using a commercially available radio frequency magnetron sputter unit (Edwards Auto 306). The purity of the Ti target was 99,995%. The titanium was deposited with a power of 83 W for 4 min. The surface layer was naturally oxidized. Directly before the AFM measurements the $TiO_2$ slides were put in an oxygen plasma (100W, 0.3mbar, 1h, Edwards GMBH, Kirchheim, Germany) and afterwards rinsed with ultrapure water.

### 3.2.5 Supported lipid bilayer

DOPC (1,2-dioleoyl-sn-glycero-3-phosphocholine), DOPS (1,2-dioleoyl-sn-glycero-3-phospho-L-serine sodium salt) and 18:1 Liss Rhod PE (1,2-dioleoyl-sn-glycero-3-phosphoethanolamine-N-(lissamine rhodamine B sulfonyl) ammonium salt) were purchased from Avanti Polar Lipids, USA.

**Figure 3.7:** Schematic of DOPC (1,2-dioleoyl-sn-glycero-3-phosphocholine). The two oleoyl fatty acid chains are depicted in red and orange, they make up the hydrophobic tail of the lipid. The fatty acid chains are bound to a glycerol group depicted in green. The hydrophilic headgroup further consists of the phosphate group in blue and the choline depicted in purple. DOPC is zwitterionic with a negative charge at the phosphate and a positive charge at the choline group.

DOPC is a zwitterionic amphipathic molecule and is depicted in Figure 3.7. It consists of two hydrophobic fatty acid chains bound to a glycerol. The hydrophilic headgroup further consists of a negatively charged phosphate group and a positively charged choline group.

DOPS is depicted in Figure 3.8. It is similar to DOPC but has a serine group instead of a choline group. Because of this it carries a net negative charge.

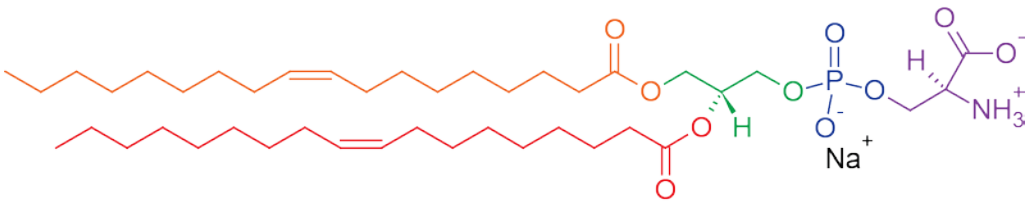

**Figure 3.8:** Schematic of DOPS (1,2-dioleoyl-sn-glycero-3-phospho-L-serine (sodium salt)). The two oleoyl fatty acid chains are depicted in red and orange, they make up the hydrophobic tail of the lipid. The fatty acid chains are bound to a glycerol group depicted in green. The hydrophilic headgroup further consists of the phosphate group in blue and the serine group depicted in purple. DOPS carries a net negative charge.

18:1 Liss Rhod PE is depicted in Figure 3.9. Bound to the headgroup is a fluorescent rhodamine group. The lipid carries a net negative charge.

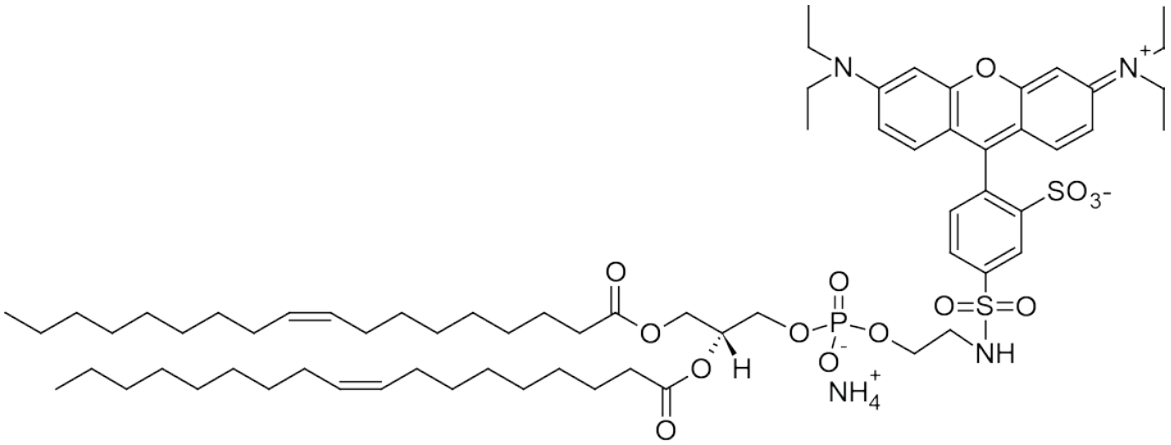

**Figure 3.9:** Schematic of 18:1 Liss Rhod PE (1,2-dioleoyl-sn-glycero-3-phosphoethanolamine-N-(lissamine rhodamine B sulfonyl) ammonium salt). The fluorescent rhodamine is bound to the lipid headgroup.

Supported lipid bilayers (SLB) of DOPC were prepared from mixtures of DOPC and 18:1 Liss Rhod PE in the molar ratio of 2000:1 by vesicle fusion on mica. In addition for some measurements supported lipid bilayers with 20% DOPS were prepared.

- DOPC and 18:1 Liss Rhod PE were mixed in chloroform at molar ratio 2000:1.
- For SLBs with 20% of DOPS: DOPC, DOPS and 18:1 Liss Rhod PE mere mixed in chloroform at molar ration 159.2 : 39.8 : 1.
- Chloroform was evaporated form the lipid mixture samples in a gentle nitrogen gas stream and afterwards the samples were placed in a vacuum for 1 hour.
- The lipids were solvated at 2.5 mg/ml in ultrapure water and the mixture was extruded using the Avanti Mini Extruder with polycarbonate membranes of pore size 100 nm.
- The vesicle solution was diluted 1:5 (0.5 mg/ml) and $CaCl_2$ was added to a concentration of 3 mM.
- Mica was glued to a glass slide and inserted into a fluid cell together with a hydrophobic control substrate (PTFE or hydrogen terminated diamond).
- Mica was then freshly cleaved and a droplet of 100 µl vesicle solution was incubated on the mica for 10 minutes before the sample was rinsed with ultrapure water.
- The sample was then placed in an oven at 50°C for 1h to get rid of possible remaining adherent vesicles.
- The formation of the bilayer was confirmed by looking at the fluorescence in a microscope. The sample was slowly rinsed with the measurement buffer of 10 mM Hepes and 50 mM NaCl at pH7 and then placed in the AFM.

## 3.3 Atomic Force Microscope

The atomic force microscope (AFM) is a high resolution scanning probe microscope that was developed by Binnig et al. in 1986. [54] A mechanical probe consisting of a cantilever with a sharp tip is scanned over the surface. Forces between the tip and the surface cause the lever to bend. The deflection of the lever is detected over a laser beam reflected from the back of the lever onto a segmented photodiode. Accurate scanning and movement in z direction is performed by piezoelectric elements.

### 3.3.1 Imaging with an AFM

Advantages of AFM imaging include the possibility to image not only in air but also in fluid. Imaging with an AFM can be done in many different modes. In a simple contact mode image a force is chosen as setpoint and held constant during the scan by adjusting the distance between the cantilever and the surface. This yields a topographic height image with nanometer resolution.

In contact mode imaging the imaged object can be subject to high shear forces. In order to avoid this imaging can be performed in tapping mode. The cantilever is driven to oscillate near its resonance frequency by an additional piezo element. Forces between the surface and tip perturbate the oscillation and cause the oscillation amplitude to decrease. In amplitude modulation tapping mode a feedback loop adjusts the height of the cantilever above the surface to keep the amplitude constant. This yields a height image of the sample topography.

All AFM images in this thesis were obtained with an MFP-3D SA (Asylum Research, Santa Barbara, USA, now part of Oxford Instruments). For tapping mode in air OMCL AC240 TS cantilevers (Olympus, Germany) were used. For tapping mode in aqueous solution softer silicon nitride cantilevers (MLCT B,D,E,F Bruker SPM probes, Camarillo, USA) were used. For contact mode in aqueous solution the MLCT C lever is a good choice.

### 3.3.1 Single Molecule Force Spectroscopy measurements

The AFM is not only a tool for high resolution imaging but it is also possible to use it for force spectroscopy measurements. In those the high force resolution of the AFM is employed to measure binding forces of individual molecules. Single molecules are tethered between AFM tip and surface either by unspecific interaction or through covalent attachment. The tip is moved in z direction towards the surface and after contacting the surface is retracted again. In such a way force distance traces are obtained. The strength of a single bond between a biomolecule and surface can be deduced from the rupture forces. This technique has been used to measure the strength of ligand receptor systems as well as covalent bonds. [45,55,56] In this type of measurement the bond rupture forces depend on the force loading rate, e.g. the pulling velocity as discussed in chapter 2.3.2. Dynamic force spectroscopy, the measurement of rupture forces for different force loading rates opens up new possibilities to explore the energy landscapes of those bonds. [24,57,58]

With the AFM it is also possible to determine mechanical properties of biomolecules by stretching them between the AFM tip and surface. This approach has led to new insights into the mechanics of proteins and DNA at a molecular level. [18,59,60,61]

Furthermore it is possible to measure interactions between whole polymer chains and surfaces. Depending on the nature of the interaction and the measurement parameters different motives can be observed in the measured force distance traces. When the speed of the pulling velocity in z direction is faster than the dynamics of the probed bonds the polymer chain is stretched until the bond ruptures. [62] If there are several bonds in the polymer chain interacting with the surface in this way, a saw tooth pattern can be observed in the force distance trace. When the dynamics of the interaction between polymer and surface are fast compared to the pulling velocity the unbinding and rebinding of the individual bonds is not resolved anymore by the measurement and flat force plateaus can be observed in the force distance traces. [63,64]

Those flat force plateaus are often observed on hydrophobic surfaces. A combined experimental and molecular dynamic simulation study found that while on hydrophobic self assembled monolayers force plateaus were observed, on too hydrophilic SAMs (contact angle below 50°-60°) no interaction of the polymers with the surface were observed. The molecular dynamic simulations revealed that this is caused by a strongly bound interfacial water layer at the surface. [65]

A different study desorbed poly-D-tyrosine from solid hydrophobic surfaces (PTFE, SAM) as well as from water-chloroform and water-air interfaces. Despite the large difference in interfacial energy the plateau forces changed very little. This is explained by a compensation mechanism between dispersive and hydration forces. [66]

The influence of the solvent on the plateau forces was investigated as well. Adding kosmotropic (they can salt out proteins) salts to the measurement solution increases the plateau force but only modestly. [67] Measuring in water ethanol mixtures leads to a decreasing plateau force with increasing ethanol concentrations. [66]

Horinek et al. investigated the individual contributions to the free energy change between adsorbed and desorbed polymer with molecular dynamics simulations. They found that individual interactions between polymer, solvent and surface are quite large but nearly cancel each other out leading to a relatively low free energy difference. [68] This compensation mechanism explains why most variations of experimental parameters lead to relatively small changes in the plateau force.

#### 3.3.1.1 Tip functionalization protocol

To measure forces between single molecules and surfaces with an AFM the probe molecule needs to adhere to the tip. In early single molecule experiment the molecule was deposited on the surface and picked up by the tip via unspecific interactions. This technique has the disadvantage that the molecule is picked up at unspecified points. Furthermore the whole measurement is not done with one single molecule but which of the molecules on the surface is picked up from the surface is random. To be able to measure with one single molecule over a long time a tip functionalization protocol was developed which covalently attaches the probe molecule to the tip via a PEG linker. The use of PEG linkers is also useful when investigating small probe molecules. Without a linker the interaction of small molecules would be hidden in the unspecific interaction of the tip with the surface.

In a first step the silicon nitride cantilevers (MLCT, Bruker SPM probes, Camarillo, USA) are activated in an oxygen plasma. This cleans the surface and leads to the formation of hydroxyl groups on the surface.

Then amino groups are formed on the surface by silanization by incubating the cantilever chips in a Vectabond ((3-Aminopropyl)triethoxysilane, Axxora, Germany) solution.

In a third step polyethylene glycol (PEG) linker molecules are coupled to the amino groups via NHS ester chemistry. To be able to measure single molecules only a small fraction of the linker molecules have a second functional group. The probe molecules are attached at this second functional group. What chemistry is employed depends on the functional groups of the probe molecule. All the probe molecules in this thesis were attached via primary amine groups. A mixture of PEG linkers with only one NHS ester group (mPEG or $CH_3O$-PEG-NHS, 5kDa, Rapp Polymere GmBH, Tübingen, Germany) with PEG linkers with two NHS ester groups (DiNHS-PEG or PEG-α-ω-Di-NHS, 6kDa or 10kDa, Rapp Polymere GmBH, Tübingen, Germany) is prepared in dry chloroform in a typical ratio 1500:1. The cantilever chips are incubated in this solution.

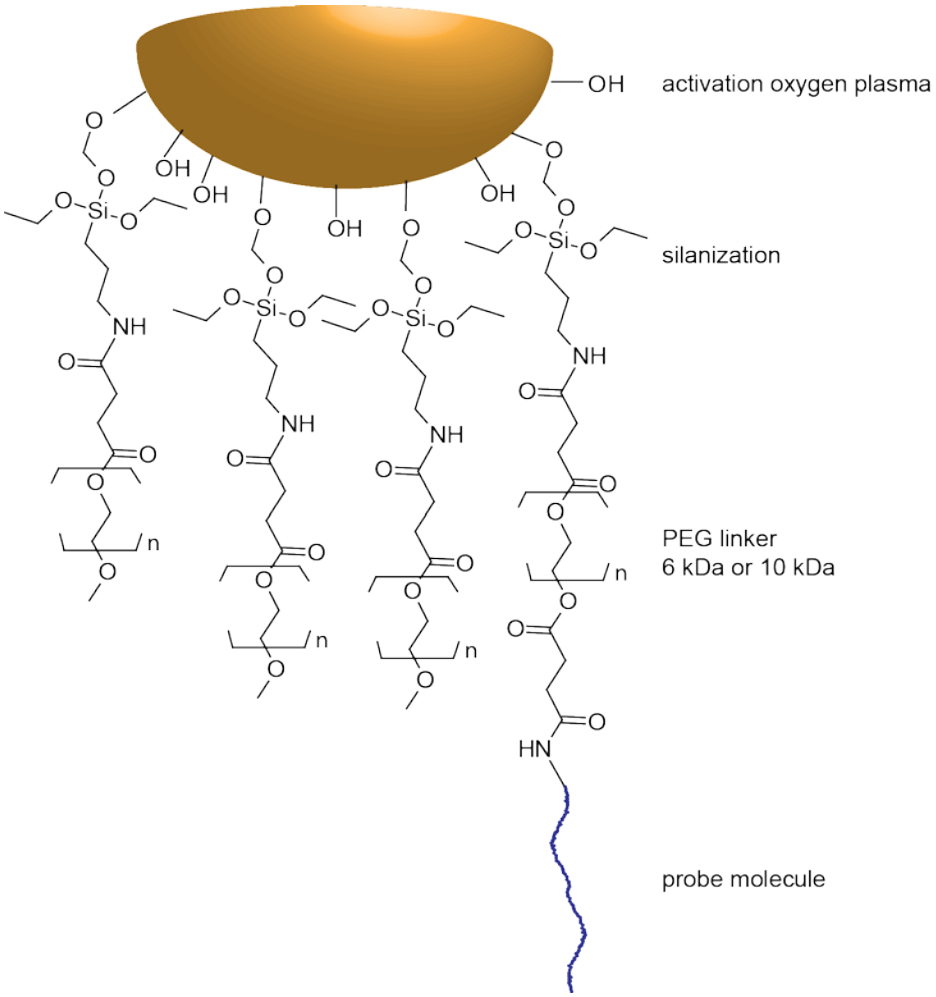


**Figure 3.10:** The figure illustrates the tip functionalization protocol with the steps plasma activation, silanization, coupling of PEG linker and coupling of the probe molecules. The schematic shows one bound probe molecule and three PEGs with a methyl group.

The mPEG passivates the tip and the probe molecules are bound to the DiNHS-PEG in the fourth step. This is performed either in sodium borate buffer at pH 8.1 or in a dry organic solvent (VWR, Germany) depending on the solubility of the probe molecule. The conjugation of the probe molecule to the tip is illustrated in Figure 3.10. The protocol is described in the Appendix in more detail.

### 3.3.1.2 Constant pulling velocity measurements

All force spectroscopy measurements were done with an MFP-3D SA (Asylum Research, Santa Barbara, USA, now part of Oxford Instruments). The cantilever is mounted on a holder suited for liquid measurements. The surfaces can be placed in home build or commercially available fluid cells. For measurements below or above room temperature special fluid cells can be operated with the Cooler Heater respectively Bio Heater build by Asylum Research.

In the standard AFM force spectroscopy measurements the tip approaches the surface at constant velocity (typically 0.5 µm/s or 1 µm/s) until a certain surface trigger force (on a solid surface typically several nN) is reached. At this point a surface dwell of typically 1 s is observed. Afterwards the tip is retracted again for a set force distance (typically 1µm) with constant velocity. The deflection of the cantilever and the piezo path of the tip are recorded. This process is repeated several times. For dynamic force spectroscopy the measurement is repeated for different pulling velocities.

#### 3.3.1.3 Constant distance measurements

A variation of this experimental protocol is the constant distance measurement. The cantilever is not fully retracted. Instead the retraction is stopped at a point where the biomolecule is still attached to the surface. At this point a waiting time, for example 10 s, is observed at constant distance to the surface. The time until desorption of the probe molecule occurs is recorded. Then the cantilever is completely retracted and the measurement is repeated. Figure 3.11 illustrates this measurement. The distance at which the waiting time is observed is varied. In this way the lifetime of the biomolecule is probed for different fractions of the still adsorbed polymer chain.

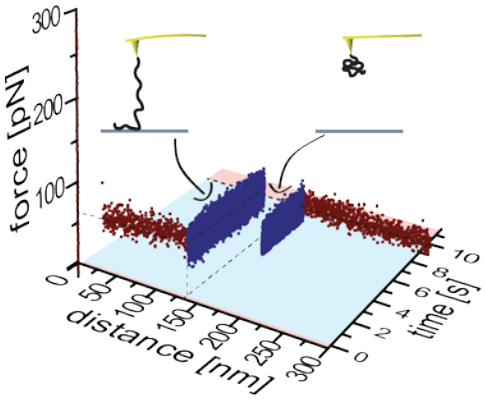


**Figure 3.11:** This figure illustrates a waiting time at constant distance measurement. The polytyrosine chain is only partially desorbed from the hydrophobic surface and a waiting period of 10 s is then observed at fixed distance H=135nm. During the waiting time the polymer completely desorbs as can be seen from the drop in force to zero. The polymer still adsorbed at the beginning of the waiting time and desorbed at the end of the waiting time is drawn as schematic in the insets.

#### 3.3.1.4 Stretching

When the probe molecule is covalently attached to the tip and interacts with the surface the probe molecule is stretched between the tip and surface during retraction of the cantilever. Is the bond with the surface strong, and thus the probe molecule not mobile on the surface, high forces can be reached before the bond ruptures. This can for example be achieved by a

maleimide functionalized surface which can form covalent bonds with cysteins of the probe molecule.

The standard constant pulling velocity protocol can be employed here. But sometimes it is interesting to not immediately rupture the bond to the surface but to observe several successive stretching relaxation cycles. In this way a possible hysteresis between retraction and extension curves can be investigated.

To achieve this the surface trigger is disabled and a small force distance is chosen so that the bond does not rupture. Once a bond is formed the starting point of the force distance curve is slowly moved away from the surface. Now several retraction and extension cycles can be measured while the same single biomolecule is stretched between tip and surface.

### 3.3.2 Calibration

In an AFM force spectroscopy experiment deflection and piezo path values are measured. To convert the deflection and piezo path into force distance traces the inverse optical lever sensitivity (InVOLS) and the spring constant of the cantilever have to be determined.

#### 3.3.2.1 Inverse optical lever sensitivity

The inverse optical lever sensitivity (InVOLS) is determined by pressing the cantilever tip on a hard surface. [69] The slope of the deflection against piezopath in contact with the hard surface is the optical lever sensitivity. The inverse of the slope is the InVOLS. With the help of the InVOLS the deflection measured in Volts on the photodiode can be converted in the actual displacement of the bend cantilever in nanometer. This is needed to convert the piezopath into the distance between tip and surface. The InVOLS is extracted from at least six force curves and averaged. For each part of the measurement like different measurement on different surfaces or in several solutions the InVOLS is determined again.

#### 3.3.2.2 Spring Constant

The spring constant is determined by the thermal noise method [70] immediately after the InVOLS is measured. The thermal noise spectrum is collected with the cantilever far withdrawn from the surface at the highest quality setting of the MFP 3D. 20 spectra are accumulated to receive a good signal to noise ratio. Then the thermal noise spectrum is fitted with a harmonic oscillator as automated in the Asylum Research MFP 3D software. From this fit the spring constant is extracted. The spring constant is determined for each part of the measurement but at least once at the beginning and end. All measured spring constant of the same cantilever are averaged and the same value is used for the whole experimental set.

The deflection converted to nanometer by multiplying with the InVOLS is multiplied with the spring constant to calculate the force.

## 3.4 Data Analysis

From the piezopath and the deflection, force distance traces are calculated with the help of InVOLS and spring constant. This is done automatically by a home-written algorithm in Igor Pro. The data is further analyzed depending on the observed motives in the measurement.

### 3.4.1 Plateau length and force

In the case of flat force plateaus the plateau is fitted with a sigmoidal curve (see Figure 3.12 A). Plateau length and plateau force are extracted from the fit. The plateau forces and the plateau length are plotted into histograms and fitted with a Gaussian (see Figure 3.12 B and C). From this Gaussian fits the peak plateau force and plateau length values as well as the standard variation are extracted.

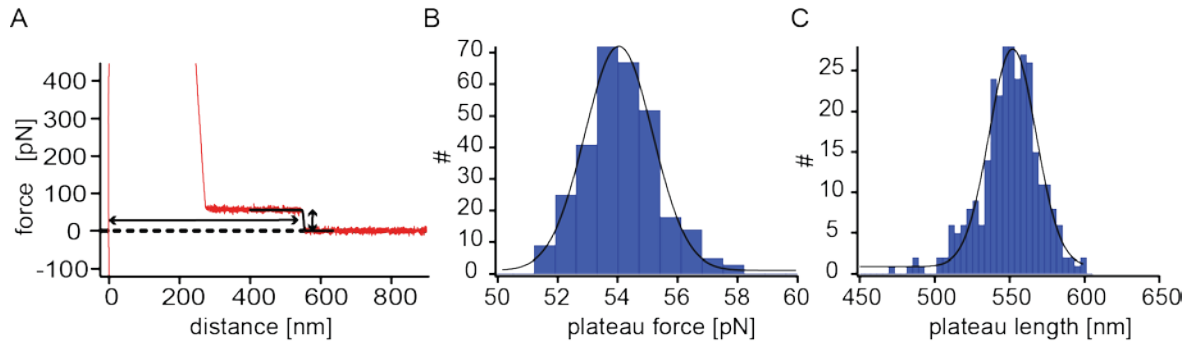


**Figure 3.12:** A depicts a sample force distance curve measured with polylysine on a hydrophobic SAM. The arrows indicate the plateau force and plateau length. In B the plateau forces of the measurement are plotted in a histogram and fitted with a Gaussian. The peak value is 54 pN and the standard variation is 2 pN. In C the plateau lengths of the measurement are plotted in a histogram and fitted with a Gaussian. The peak value is 552 nm and the standard variation is 31 nm.

### 3.4.2 Rupture force analysis

In the case of more complex motives than flat force plateaus for example single or multiple rupture events an home-written algorithm extracts the peak forces of the force distance trace. To exclude unspecific adhesion events a minimal distance from the surface, for example 15nm, is stipulated. Furthermore in the peak finder software a minimal force value can be set (for example 20 pN) and the data is smoothed (typically over 10 measurement points) before searching for peaks to exclude noise. The maximal force peak is determined and optionally averaged over a number of points (typically 10). The length at the maximal force is extracted as well. In addition to the highest force peak the last force peak is extracted as detach force together with the detach length. An average force is calculated beginning at the unspecific force cutoff until the detach length. This is illustrated in Figure 3.13 A. In the case of dynamic

force spectroscopy measurements the instantaneous loading rate is determined for each curve. For this the force is plotted against time and a line is fitted to a number of points (typically 50) before the maximal peak. The slope of the fit is the instantaneous loading rate in the moment of rupture. This is shown in Figure 3.13 B.

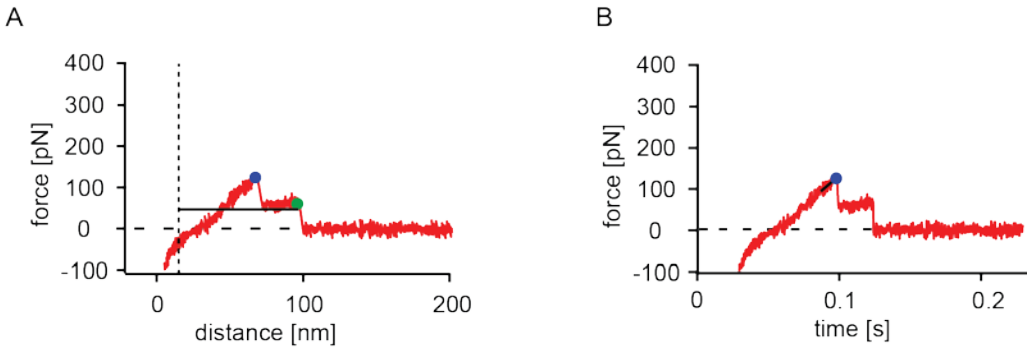


**Figure 3.13:** A shows a sample force distance curve for polytryptophan on a DOPC bilayer. The adhesion peak cutoff is marked with a dashed line and the averaged force with a solid line. The max peak is indicated by a blue dot the detach peak by a green dot. B shows a force time trace of the same measurement. The max peak is indicated by a blue dot and the fit to determine the instantaneous loading rate is plotted as a black line.

Furthermore rupture events can in some cases be fitted with the appropriate polymer model to learn more about the elastic properties of the polymer (see chapter 2.1 for details on polymer models). The contour length as well as the Kuhn or persistence length can be extracted from those fits.

# 4 Single polypeptide desorption kinetics on hydrophobic surfaces

*This chapter is based on the following publication: Krysiak, S.; Liese, S.; Netz, R. R.; Hugel, T., Peptide Desorption Kinetics from Single Molecule Force Spectroscopy Studies. Journal of the American Chemical Society,* ***2013****, 136, 688.* [53]

Understanding the desorption kinetics of polymers from solid surfaces is important for as diverse fields as polymer adhesives or biological systems. Long polymer chains have a high number of internal degrees of freedom which makes them more complex to model. A simple expectation would be that the desorption rate decreases exponentially with the total adsorption free energy. This would mean that the desorption rate decreases exponentially in polymer length. It also implies the desorption can be treated as a single step process with one large energy barrier. The first experimental indication that this is not the case is the work by Johnson et al. [71] who found that the lifetime of polymers on a surface scales as a power law in molecular mass. They rationalized this by claiming the kinetics of the desorption process to be mainly governed not by the total free energy but by the center of mass diffusion and that the lifetime is reciprocally proportional to the diffusion coefficient. Descas et al. and Wang et al. found a similar power law dependence in Monte Carlo Simulations. [72,73] They observed loop and train formation initiated at different points of the polymer chain simultaneously.

To describe the desorption process, in particular the desorption rate of the polymer chain, four parameters have to be known. The polymer contour length $L_c$ or number of monomers $N$, the adsorption free energy per monomer $\lambda$, the Kuhn or persistence length depending on the polymer model and the monomeric desorption rate $k_{0.}$ In a standard AFM desorption experiment where the surface polymer bonds relax faster than the polymer is pulled, flat force plateaus are observed in the force distance traces. In such an experiment two parameters are extracted namely the plateau length and the plateau force. The plateau force is related to the adsorption free energy through the FJC or WLC polymer model. To calculate one from the other the Kuhn or persistence length has to be known. The plateau length is not identical to the contour length but clearly a function of it. Their relation is determined by the Kuhn length, the polymer model and the kinetic regime and will be investigated in this study. Determining the polymer length accurately is not easy and finding a relationship between plateau length and contour length would mean that polymer length

could be determined with AFM force spectroscopy. The two values measured in the standard AFM force spectroscopy experiment, the plateau force and plateau length, are clearly not enough to determine all four parameters of the desorption process. For this two complementary experimental protocols are employed.

The standard constant pulling speed experiments are repeated for varying adsorption free energies, which were varied by adding cosolutes to the measurement solution. The addition of ethanol lowers the adhesion energy while the addition of certain salts increases the adhesion energy. To be able to relate the plateau lengths of different adhesion free energies to each other it is essential that the whole experiment is performed with one and the same polymer. To ensure this the polymer is covalently coupled to the AFM tip and a probe with a narrow monomodal peak in the plateau length histogram is chosen.

In a complementary second protocol the kinetics of the desorption process are studied in a constant distance measurement. The cantilever is only partially retracted from the surface to a certain distance at which the polymer is still attached and a waiting time is observed. If the polymer desorbs during this time the measured force drops to zero and the time till desorption occurs is recorded. This is repeated for different distances.

By simultaneously fitting both experiments it is possible to determine all relevant parameters of the desorption process.

## 4.1 Solvent effect on desorption length and desorption force

The standard constant pulling experiments were performed with polylysine and polytyrosine on a hydrophobic self assembles monolayer (SAM). Pulling speeds of 0.5 µm/s or 1 µm/s were chosen and a dwell time of 1 s on the surface was observed. Flat force plateaus were observed in the force-distance traces and plateau force and plateau length are extracted with a sigmoidal fit of the force curves. This was done for at least 90 force curves for each measurement point and plateau forces and plateau length were collected in histograms. The measurements were performed in water as well as in different water-ethanol mixtures. Adding ethanol to the measurement solution weakens the hydrophobic interaction between the polyhomopeptides and the hydrophobic surface and leads to lower plateau forces. Figure 4.1 A and D show plateau force distributions for polytyrosine and polylysine in water and water mixed with different molar percentages of ethanol. In Figure 4.1 B and E the plateau length histograms of the same measurements are shown. The data for polylysine and polytyrosine show clearly that the plateau length decreases with decreasing plateau force. The histograms were fitted with a Gaussian and the peak value as well as the width of the distribution were extracted. The peak values of the plateau length are plotted against the

peak values of the plateau force in Figure 4.1 C and F with the width of the distributions as error.

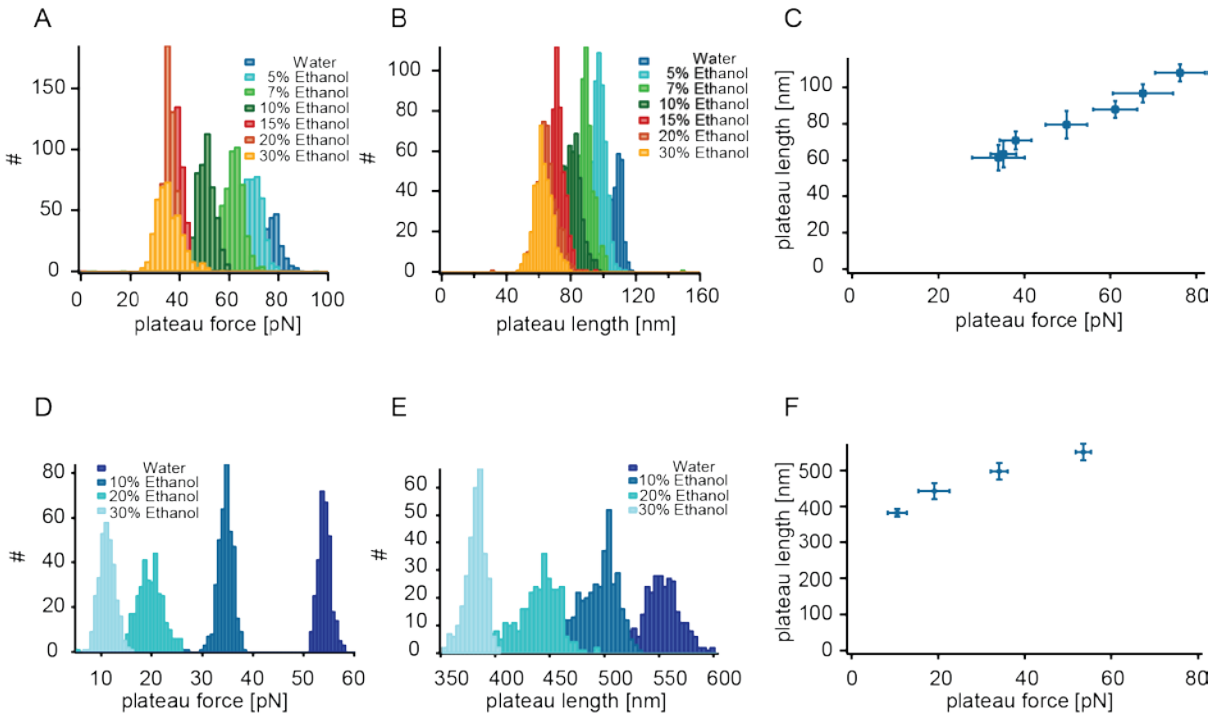


**Figure 4.1:** Histograms of plateau force (A,D) and plateau length (B, E) for polytyrosine (A,B) and polylysine (D,E) in water and water ethanol mixtures of different molar percentage. C and F show the peak plateau length plotted against the peak plateau force for polytyrosine (C) and polylysine (F)

To describe the plateau length as a function of plateau force the desorption process has to be studied in more detail. The linear polymer is continuously pulled away from the surface and so the height of the tip above the surface increases with time as illustrated in Figure 4.2. Part of the polymer is desorbed into solution (contour length *s*) while another part is still adsorbed on the surface (*L*-*s*). The desorbed part of the polymer chain is stretched by the plateau force f.

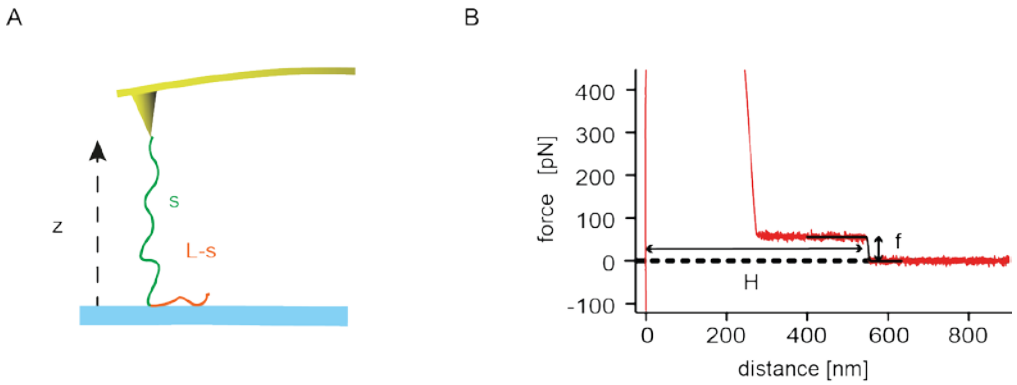


**Figure 4.2:** A shows a schematic of the desorption process. The linear polymer is continuously pulled away from the surface in *z* direction. The part of the polymer already desorbed has the contour length *s*, the part still adsorbed *L*-*s*. The desorbed polymer is stretched with force *f*. In B a sample force distance curve is shown with a flat plateau of constant force *f*. At a certain height of the tip above the surface *H* the polymer completely desorbs.

The question arises, at which tip surface distance *H* does the polymer desorb completely from the surface? One approach to this problem is to determine from which point on its energetically favorable for the polymer to desorb. The free energy *F* of the chain consists of the part still adsorbed and the stretched part in solution:

$$F(s,H) = -\lambda(L-s) + \int_0^H f(z,s)dz \tag{4.1}$$

This can be rewritten as:

$$F(s,H) = -\lambda(L-s) + s\int_0^{H/s} f\left(\frac{z}{s}\right) d\left(\frac{z}{s}\right) \tag{4.2}$$

since *f* is a function of *z/s*. The relationship between *f* and *z/s* is given in equation (2.4) for the FJC and in equation (2.5) for the WLC model.

Minimization with respect to *s* gives:

$$\left.\frac{\partial F}{\partial s}\right|_{s_{min}} = \lambda + \int_0^{H/s_{min}} f\left(\frac{z}{s}\right) d\left(\frac{z}{s}\right) - \frac{H}{s_{min}} f\left(\frac{H}{s_{min}}\right) \stackrel{!}{=} 0 \tag{4.3}$$

Multiplying by $s_{min}$, one can insert the integral term in (4.2):

$$F(s_{min},H) = -\lambda L + Hf \tag{4.4}$$

So the free energy of the chain increases linear with increasing height *H*. The free energy is plotted in Figure 4.3 A. Defining the equilibrium height $H_{eq}$ as the height at which the free energy reaches zero, one gets:

$$\frac{H_{eq}}{L} = \frac{\lambda}{f} \tag{4.5}$$

The relation between *λ* and *f* depends again on the polymer model used and can be derived from (4.3) and equation (2.4) for the FJC and equation (2.5) for the WLC model. Equation (4.5) means that at $H_{eq}$ the area under the plateau (plateau force times plateau length) equals the total adsorption free energy of the polymer chain. $H_{eq}/L$ plotted against the dimensionless $fa/k_BT$ is shown in Figure 4.3 B and C for FJC and WLC respectively. For both models the force is normalized by multiplying with the Kuhn length a divided by Boltzmann

constant times temperature $k_BT$. For the WLC model the persistence length is replaced by half of the Kuhn length following equation (2.3).

Another way to look at the problem is to determine how far from the surface the cantilever tip could be maximally pulled before the polymer desorbs. For this it is assumed that before desorption only one monomer remains adsorbed and $s$=$L$. Then $H_{max}$ follows straightforward from the relations for FJC and WLC (2.4) and (2.5):

$$\frac{H_{max}}{L_c} = coth\left(\frac{fa}{k_BT}\right) - \frac{k_BT}{fa} \tag{4.6}$$

$$\frac{fa}{2k_BT} \cong \frac{H_{max}}{L_c} + \frac{1}{4(1 - H_{max}/L_c)^2} - \frac{1}{4} \tag{4.7}$$

Even in this case $H_{max}$ is strictly smaller than the contour length $L$ since at typical plateau below 100 pN the chain is not stretched to its full contour length. $H_{max}/L$ is plotted against force times Kuhn length normalized by the Boltzmann constant times temperature for the FJC and WLC model in Figure 4.3 B and C.

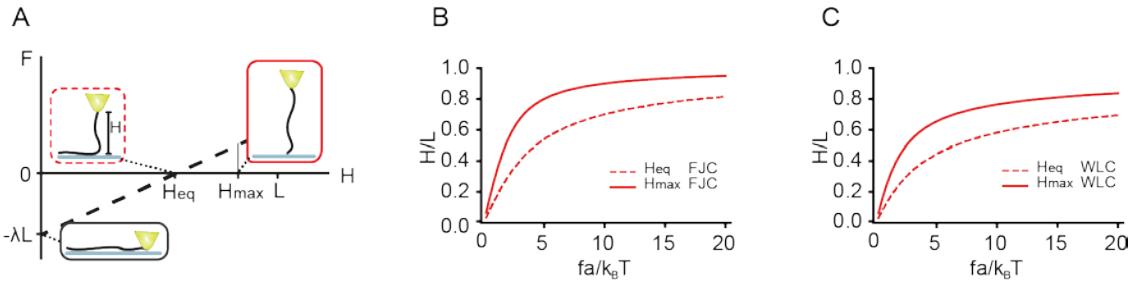


**Figure 4.3:** A shows a schematic of the desorption free energy as a function of pulling height. B and C show $H_{eq}/L$ and $H_{max}/L$ as a function of the force for the FJC and WLC model respectively

As depicted in Figure 4.3 A, while the cantilever is pulled up from the surface the free energy increases linear in height $H$ until it reaches zero at $H_{eq}$. From this point on the polymer on the surface is metastable since it would be energetically be favorable to desorb. It depends on the kinetics of the system how far in the metastable region the polymer is pulled before it desorbs at the latest at height $H_{max}$. In Figure 4.3 B and C it can be seen that both $H_{eq}$ and $H_{max}$ increase with the force. The higher the plateau force in the desorption process the further can the polymer be pulled and the longer is the plateau length. This behavior agrees well with the measured data for polylysine and polytyrosine in the water and water ethanol mixtures depicted in Figure 4.1 C and F.

In the next step $H_{max}$ and $H_{eq}$ as function of the force f are both fitted to the experimentally measured plateau length and plateau force values for different sets of measurements. Fit parameters are the Kuhn length *a* and the contour length *L*. In addition to the two experiments shown in Figure 4.1 two additional measurements for polylysine and polytyrosine each are fitted. The fitting procedure is a simultaneous fitting of the three measurements since the Kuhn length is the same for all three experiments for the same polyhomopeptide. The contour length is fitted to every experimental set separately since the polyhomopeptide samples are polydisperse and each sample has a different contour length. The fits were performed by Susanne Liese in the group of Roland Netz. For the two extra polytyrosine measurements additional to the measurements in water and water ethanol mixtures a measurement in 2 respectively 5 molar monosodium phosphate solution was added. The addition of the monosodium phosphate salt, which is classified as strongly "salting out" in the Hofmeister series strengthens the hydrophobic interaction and increases the adsorption free energy and the plateau force. The fits of $H_{eq}$ to the polytyrosine and polyylysine measurements for the FJC and WLC chain model are shown in Figure 4.4. The fitted Kuhn lengths as well as contour lengths are given in the insets. The fits for $H_{max}$ are plotted in Figure 4.5.

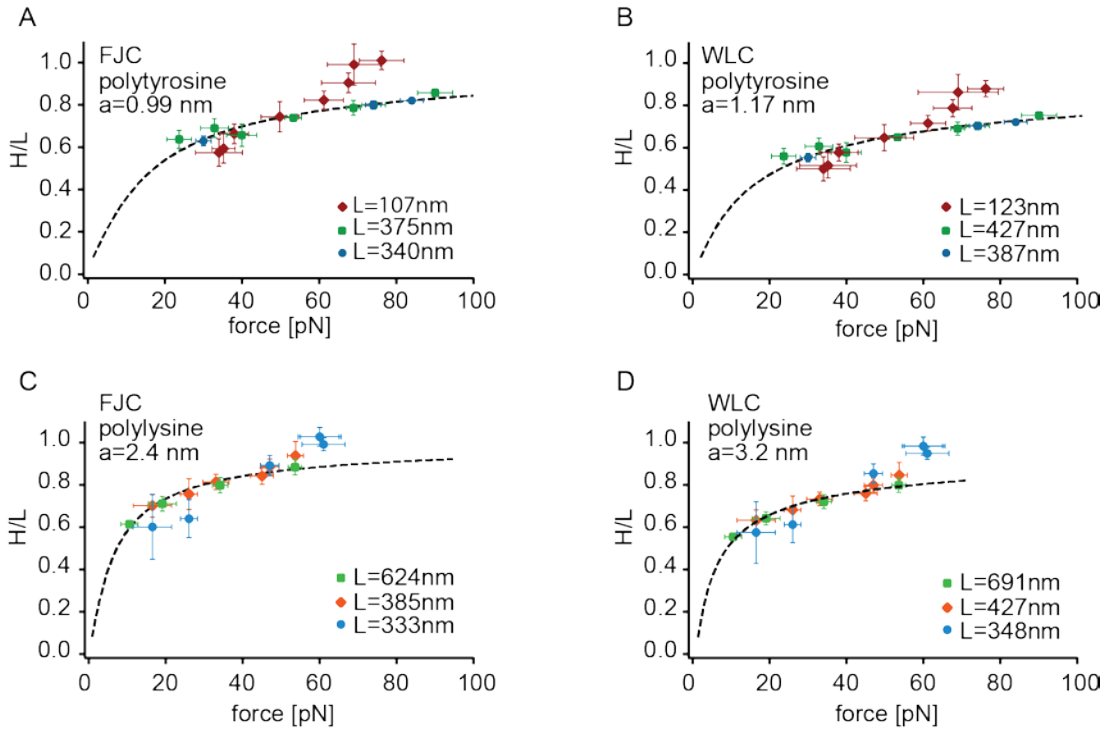


**Figure 4.4:** A and B show three data sets of polytyrosine measurements in different water ethanol mixtures fitted with $H_{eq}$ as a function of force f using the FJC and WLC model respectively. The data set marked with the red diamond is also shown in Figure 4.1 A-C. The highest force point of the green square and blue dot data sets were measured in a monosodium phosphate solution. C and D show three data sets of polylysine measurements in different water ethanol mixtures fitted with $H_{eq}$ using the FJC and WLC model respectively. The data set marked with the light green square is also shown in Figure 4.1 D-F. The fitted contour length *L* and Kuhn length *a* are given as insets.

Both fits of $H_{eq}$ and $H_{max}$ describe the data well. The fitted Kuhn lengths are higher for the WLC than for the FJC chain model in all cases. Furthermore the Kuhn length of polylysine is noticeably larger than the Kuhn length of polytyrosine. In all cases for the shortest of the polypeptide chains the deviations from the fits are most pronounced. This is the measurement denoted with blue dots for polylysine and the measurement marked with red diamonds for polytyrosine.

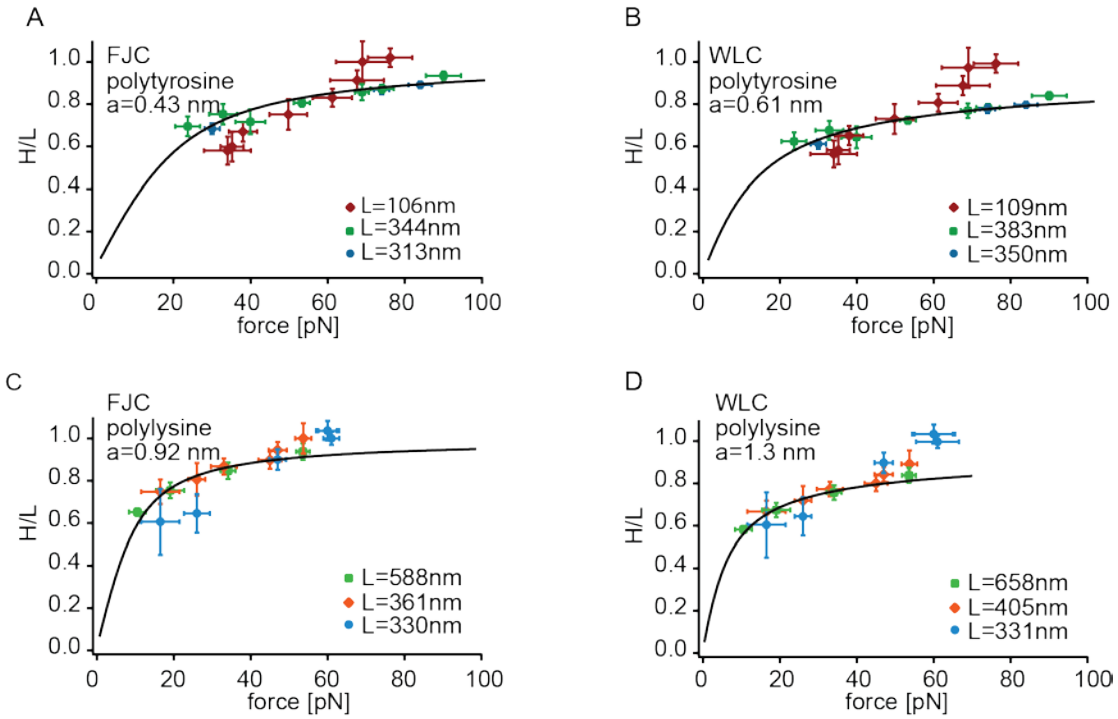


**Figure 4.5:** A and B show three data sets of polytyrosine measurements in different water ethanol mixtures fitted with $H_{max}$ for FJC and WLC respectively. The data set marked with the red diamond is also shown in Figure 4.1 A-C. The highest force points of the green square and blue dot data sets were measured in a monosodium phosphate solution. C and D show three data sets of polylysine measurements in different water ethanol mixtures fitted with $H_{max}$ for FJC and WLC respectively. The data set marked with the light green square is also shown in Figure 4.1 D-F. The fitted contour length $L$ and Kuhn length $a$ are given as insets.

Since both fits of $H_{eq}$ and $H_{max}$ work equally well, from the constant velocity measurements alone, it cannot be judged whether the desorption occurs as soon as energetically possible or the if polymer is pulled into the metastable region. To determine this, a kinetic measurement in a complementary protocol is necessary.

## 4.2 Waiting time - desorption at constant distance

To get more insight on the kinetics of the desorption process the measurement protocol is modified. Instead of retracting the cantilever with a constant pulling speed the retraction is divided into two steps and halted at a distance where the polypeptide is still attached to the surface. Then the distance is held constant for a certain time, for example 10 s. If the

polymer desorbs during this time the force suddenly drops to zero. The waiting time *t* till the desorption occurs is extracted. If no desorption occurs the waiting time is set to the maximal value, in the example 10s. Figure 4.6 A illustrates the measurement in the waiting time protocol. The measurement was done in pure water with polytyrosine on a hydrophobic SAM. In Figure 4.6 B the measured waiting times are plotted against the distance from the surface at which the waiting time occurred. Additionally a plateau length histogram of a standard constant pulling velocity measurement of the same polytyrosine chain is shown.

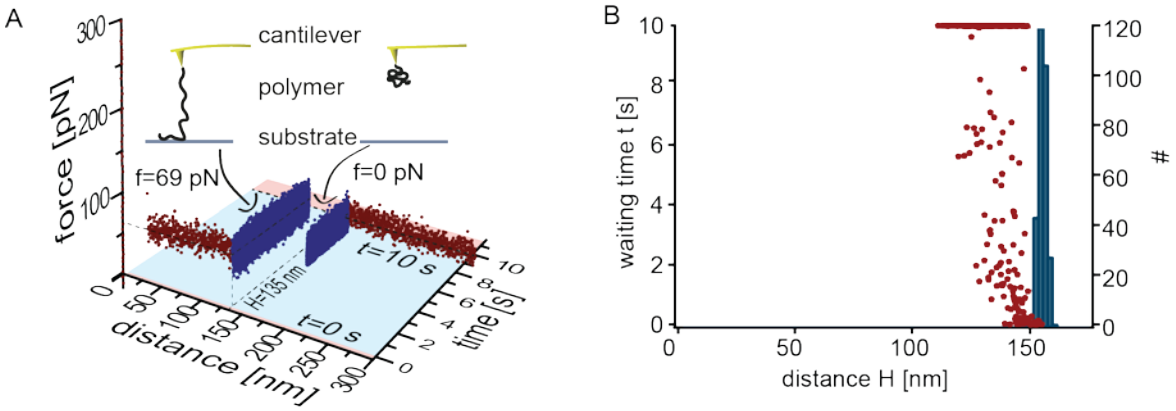


**Figure 4.6:** A illustrates the waiting time measurement. The polytyrosine chain is only partially desorbed from the surface and a waiting period of 10 s is then observed at fixed distance *H*=135nm. During the waiting time the polymer completely desorbs as can be seen from the drop in force to zero. B: in red the waiting times till desorption for 340 force curves are plotted as a function of distance from the surface. In blue the plateau length histogram of a constant pulling speed experiment with the same polytyrosine chain is shown.

For distances close to the peak plateau length the waiting times are shorter than a second. With decreasing distance from the surface the waiting time increases until the point where the polytyrosine chain does not desorb at all during the 10 s waiting time. To be able to extract a kinetic parameter from the data we need to develop a model for the chain desorption. The process is a two state process with an adsorbed and a desorbed state similar to the Bell model described in chapter 2.3.

$$\frac{dP_{ads}}{dt} = -kP_{ads} \tag{4.8}$$

With the probability for the polymer to be adsorbed at time 0 and *H=0* $P_{ads}(0)=1$. Since in experiments no readsorption events were observed we assume that the readsorption rate is negligible. This is a reasonable approximation for large tip-surface distances. Contrary to the simple Bell model discussed earlier instead of a single bond there is a whole chain interacting with the surface. As has been found both experimentally [71] as well as theoretically [72,73] the polymer desorption time on a surface does not scale exponentially in polymer length (and thus the total adsorption free energy) as would be expected from the Arrhenius law. Instead the desorption process is scaling with the diffusivity of the center of mass position

and the desorption time follows a power law in polymer length. In the Rouse model the diffusivity is inversely proportional to the number of monomers in the chain as can be seen from equation (2.10) . The characteristic Rouse time is the time the center-of-mass needs to diffuse a distance on the order of its own size $R$ and it scales as $R^2N$ as in (2.11). In the context of our problem a center-of-mass diffusion in the order of R would mean desorption. This implies the desorption time scales as the Rouse time in polymer length. The chain radius $R$ itself scales as $N^v$ , and $v$=1/2 for ideal chains like FJC or WLC as can also be seen from equation (2.1). In summary the desorption time scales as $N_{ads}^{2v+1}$ or $N_{ads}^{2}$ for ideal chains in the number of adsorbed monomers. The desorption rate $k \propto 1/\tau$ can now be expressed with as a monomeric part in Arrhenius form and the $N_{ads}^{-2}$ scaling in monomer number:

$$k = k_0 e^{-\lambda a/k_B T} N_{ads}^{-2} \tag{4.9}$$

where $k_0$ denotes the effective monomeric desorption rate. The value $N_{ads}$ can be expressed as $N_{ads}=N(1-s/L)=N(1-H/H_{max})=L/a(1-H/H_{max})=L/(H_{max}a)(H_{max}-H)$ where $s/L$ is the already desorbed part and $H/s=H_{max}/L$. The last equation simply states that the ratio between the tip surface distance H and the contour length of the desorbed chain part s remains constant for the whole desorption process. This is true for flat force plateaus where the force is constant. The desorption rate is a function of the pulling height $H$:

$$k(H) = \frac{k_0 e^{-\frac{\lambda a}{k_B T}} \left(\frac{a H_{max}}{L}\right)^2}{(H - H_{max})^2} = \frac{\omega}{(H - H_{max})^2} \tag{4.10}$$

Now that there is an expression for the desorption rate, the rate equation (4.8) can be integrated and the probability for the polymer to be adsorbed at height H for constant pulling $v$=d$H(t)$/d$t$ calculated:

$$P_{ads}\big(H(t)\big) = \exp\left[-\int_0^{\mathrm{H(t)}} \frac{\mathrm{k(H')}}{\mathrm{v}}\,\mathrm{dH'}\right] = exp\left[-\frac{\omega}{v H_{max}\left(\frac{H_{max}}{H(t)} - 1\right)}\right] \tag{4.11}$$

Since the polymer is desorbed with constant pulling velocity prior to the waiting time $P_{ads}(H)$ is the initial adsorption probability at time 0. The probability to detach at a certain time $t$ during the waiting time follows easily from the rate equation (4.8) since $k$ is constant during the waiting time with fixed $H$:

$$p_{des}^{wt}(t) = \frac{d(1 - P_{ads}^{wt}(t))}{dt} = P_{ads}(H)k(H)e^{-k(H)t} \tag{4.12}$$

To compare the model to the experimental data an upper time cutoff *t** is included in the calculation of the mean waiting time:

$$\langle t \rangle = \int_0^{t^*} t p_{des}^{wt}(t)dt + \int_{t^*}^{\infty} t^* p_{des}^{wt}(t)dt = P_{ads}(H)\frac{1 - e^{-k(H)t^*}}{k(H)}$$

$$= e^{-\omega H/H_{max}(H_{max}-H)v}\left(\frac{1 - exp\left[\frac{-\omega t^*}{(H_{max}-H)^2}\right]}{\frac{\omega}{(H_{max}-H)^2}}\right) \tag{4.13}$$

For an infinite time cutoff this simplifies to:

$$\langle t \rangle_{\infty} = \int_0^{\infty} t p_{des}^{wt}(t)dt = \frac{P_{ads}(H)}{k(H)} = e^{-\omega H/H_{max}(H_{max}-H)v}\frac{(H_{max}-H)^2}{\omega} \tag{4.14}$$

The mean waiting time as a function of height *H* can be fitted to the experimental waiting time data. Free fit parameters are $H_{max}$ and $\omega$. The pulling speed *v* and the time cutoff *t** are known. Two polylysine and two polytyrosine waiting time measurements were performed in pure water and the results were fitted with equation (4.13). To calculate $k_0$ out of $\omega$ the adsorption free energy and the Kuhn length have to be known. They can be obtained from a fit of the constant pulling data. The fits of the four measurements are shown in Figure 4.7 as blue curves. The waiting time data which was binned for similar *H* and averaged is shown in red with the standard variation of the mean value as error. The four samples have vastly different lengths ranging from $H_{max}$=158nm to $H_{max}$=865nm and all of them could be fitted with similar kinetic parameter $\omega$. This indicates that we chose the right scaling of the transition rate with polymer length.

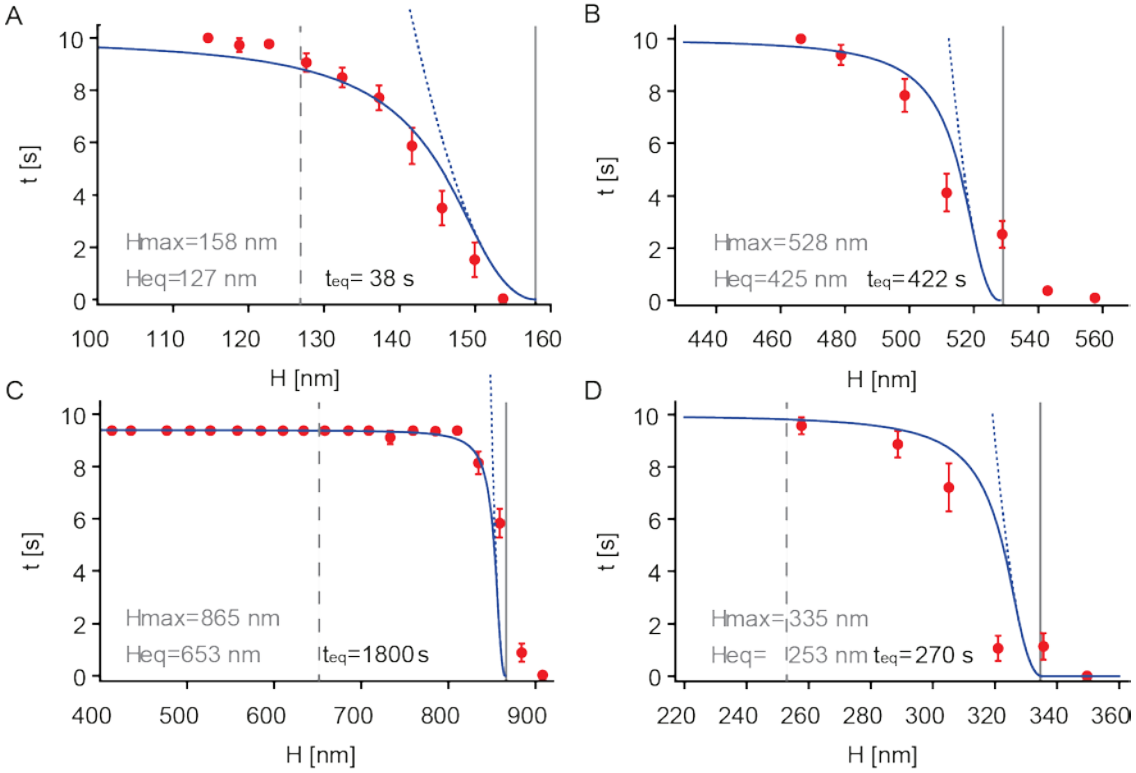


**Figure 4.7:** A and B show waiting time measurements of polytyrosine, C and D of polylysine. In A, B, D the upper time cutoff $t^*$ is 10 s in C it is 9.4 s. The mean waiting time data is shown in red with the standard variation of the mean given as error. The solid blue lines show the fit. The dashed blue lines shows the expected theoretical curve for infinite time cutoff. The fitted $H_{max}$ values are given as insets and denoted by a solid gray line, the fitted kinetic parameters are $\omega$ = 23.81nm$^2$/s (A), 24.7 nm$^2$/s (B), 25.6 nm$^2$/s (C) and 26.65 nm$^2$/s (D). Additionally the value of the equilibrium plateau length $H_{eq}$ (calculated for the FJC model) and the theoretically expected waiting time at this height for an infinite time cutoff $t_{eq}$ are given as inset. The value of the equilibrium plateau length $H_{eq}$ is indicated as dashed grey line.

All fitted values of $\omega$ are in the range 25nm$^2$/s ± 2nm$^2$/s. The values for polytyrosine are slightly lower, corresponding to the on average slightly higher forces for polytyrosine compared to polylysine. The given values for the mean waiting time at the equilibrium height $t_{eq}$ illustrate how far into the metastable region the polymers are pulled in our standard experiments in pure water. The mean waiting time at equilibrium height is 1800s=0.5h for the longest polylysine polymer in Figure 4.7 C. Even for the shortest polytyrosine polymer it still is 38 s (see Figure 4.7 A). For all four measurements in pure water the plateau length in the constant pulling protocol are far longer than $H_{eq}$ and close to $H_{max}$. The range of H for which the waiting time interpolates between zero and the time cutoff $t^*$ has a width of about 50-100 nm and is mostly independent of the polymer length. This implies the adsorbed polymer contour length rather than the total contour length determines the waiting time. This agrees with equation (4.13) which is mostly a function of $H_{max}$-$H$.

## 4.3 Simultaneous fit of measurements

The fit of the waiting time data yielded the kinetic parameter $\omega$. The physical parameters behind $\omega$ are the effective monomeric desorption rate $k_0$, the adsorption free energy $\lambda$ and the Kuhn length $a$. From equation (4.10) :

$$\omega = k_0 e^{-\frac{\lambda a}{k_B T}} \left(\frac{a H_{max}}{L}\right)^2 \tag{4.15}$$

So to get $k_0$ from $\omega$ the Kuhn length a has to be known. Therefore to receive the Kuhn length a the constant pulling data in different solutions has to be fitted. Chapter 4.1 discuses the fitting by $H_{eq}$ and $H_{max.}$ The fit of the waiting time data showed that for high forces in pure water the polypeptides were pulled far into the metastable region and therefore $H_{max}$ describes the experimentally measured plateau length better than $H_{eq}$. This is especially true for longer chains. In the cases of lower forces or shorter chains it is possible that desorption occurs before reaching $H_{max}$. With the help of the determined value for $\omega$ it is possible to calculate the probability of the chain to desorb at a certain height $H$. The probability to be detached at height $H$ is $P_{des}(H)=1-P_{ads}(H)$, the probability to detach exactly at this distance is $p_{des}=\mathrm{d}P_{des}/\mathrm{d}H$. With the expression for $P_{ads}$ from equation (4.11) the mean plateau length can be calculated as:

$$\langle H^* \rangle = \int_o^{H_{max}} H p_{des} dH = H_{max}\left(1 + \frac{\omega}{v H_{max}} e^{\omega / v H_{max}} Ei\left[-\frac{\omega}{v H_{max}}\right]\right) \tag{4.16}$$

The value of $\omega$ for measurements in pure water is found to be approximately 25 nm$^2$/s. With this measured value and equation (4.15), $k_0$ can be expressed as a function of $\lambda$, $L$ and Kuhn length $a$. $\lambda$ can be calculated from the measured plateau force $f$. Thus the mean plateau length from equation (4.15) can be fitted to the constant pulling data with only two free parameters $a$ and $L$. Those fits (done by Susanne Liese in the group of Roland Netz) are shown in Figure 4.8. For the longer polylysine chains the fit is very close to $H_{max}$, for the shorter polytyrosine chains the fit deviates from $H_{max}$ for lower forces. For very low forces and short chains the fits are even below $H_{eq}$ indicating a breakdown of the model. In this cases a nonzero re-adsorption rate should be considered. The Kuhn lengths from the fit of the kinetic model are for the FJC model $a_{Tyr}$=0.73nm, $a_{Lys}$=0.63nm and for the WLC model $a_{Tyr}$=0.77nm, $a_{Lys}$=0.69nm. The values for polytyrosine are only slightly larger than for polylysine and the Kuhn length differs only slightly between the two models. Those fitted Kuhn lengths correspond to about 1.5 to 2 times the contour length per amino acid of 0.4 nm measured by

single molecule force spectroscopy or approximately twice the end-to-end length of 0.36 nm obtained from the crystal structure. [74,75]

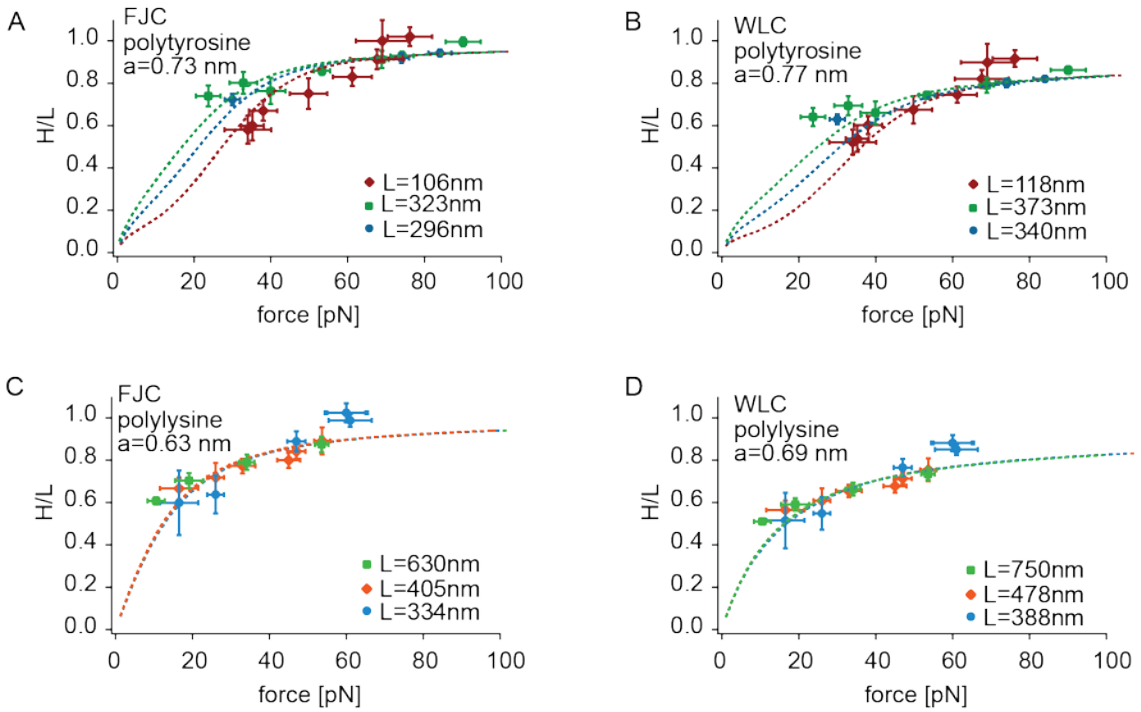


**Figure 4.8:** This figure shows the kinetic fit of equation (4.16) to the plateau length *H* and force *f* of the constant pulling data in the water ethanol measurements. The measured plateau length is normalized to the fitted contour length *L*. Values for *L* and Kuhn length *a* are given in the insets. A and B show the three datasets of polytyrosine fitted with the FJC and WLC model respectively. C and D show the same for the three polylysine measurements.

With those values of the Kuhn length, the pulling force in water of 70 pN for polytyrosine and of 60 pN for polylysine and $\omega$ =25nm$^2$/s, $k_0$ can be calculated. For the FJC model one gets 5.2*10$^5$ Hz for polytyrosine and 4*10$^4$ Hz for polylysine. Those values are considerably smaller than the relaxation rate of a single monomer in the order of 10$^{10}$ Hz. [76] This indicates that the connectivity of the monomer in the chain leads to hindered kinetics that slow down the desorption process compared to an isolated monomer. This is also relevant to understand the kinetics of other peptide chain systems like protein folding.

## 4.4 Effect of a readsorption rate and velocity dependence

During all experiments a re-adsorption after the polypeptide completely desorbed was never observed. Still it is interesting to analyze in which situations a re-adsorption rate could have an influence on the measurement. If readsorption is considered detailed balance defines the ratio between desorption rate $k_{off}$ and readsorption rate $k_{on}$. With the free energy difference between the states given in equation (4.4) one gets:

$$\frac{k_{on}}{k_{off}} = e^{-\Delta F/k_B T} = e^{-(-\lambda L + fH)/k_B T} \tag{4.17}$$

Using $k_{off}$ from equation (4.10) :

$$k_{on}(H) = k_{off} e^{-\frac{\Delta F}{k_B T}} = \frac{\omega}{(H_{max} - H)^2} e^{-\frac{\Delta F}{k_B T}} \tag{4.18}$$

Below $H_{eq}$ no desorption occurs, above $H_{eq}$ $\Delta F$ is positive and $k_{on}$ rapidly decreases with increasing separation $H$. As a consequence, $k_{on}$ is negligible for fast pulling velocities. $k_{on}$ decreases faster with $H$ in the case of high desorption force. So the re-adsorption rate has to be considered for low pulling velocities and low forces. The probability to be adsorbed depends now on both $k_{on}$ and $k_{off}$:

$$\frac{dP_{ads}}{dt} = -k_{off}(H)P_{ads} + k_{on}(H)P_{des} = -k_{off}(H)P_{ads} + k_{on}(H)(1 - P_{ads}) \tag{4.19}$$

For constant height $H$ and thus time independent on and off rates the equation can be solved analytically:

$$P_{ads}(t) = \frac{k_{on}}{k_{on} + k_{off}} + \left( P_{ads}(0) - \frac{k_{on}}{k_{on} + k_{off}} \right) e^{-(k_{on} + k_{off})t} \tag{4.20}$$

For constant pulling speed and time dependent rates the differential equation has to be solved numerically.

To investigate the effect of pulling speed on the plateau length for one polylysine sample, also used in the constant pulling protocol (Figure 4.8. C, D light blue dot) as well as the waiting time protocol (Figure 4.7 D) the plateau length was measured for three pulling velocities namely 10 µm/s, 1 µm/s and 100 nm/s. Results were compared to the theoretical prediction for the plateau length as a function of pulling speed both for the model with and without re-adsorption rate. To calculate the theoretical prediction for the model with no re-

adsorption from equation (4.16) the fitted values of $\omega$=25nm$^2$/s and $H_{max}$=335nm from the waiting time measurement for the sample are taken. The force $f$=60pN is known as well as the Kuhn length of polylysine as 0.63 nm in the FJC and 0.69 nm in the WLC model. With this (4.19) can be numerically solved for the WLC and FJC model. From $H_{max}$ , $f$ and Kuhn length a the equilibrium height $H_{eq}$ for WLC and FJC can be calculated as well. This is plotted in Figure 4.9.

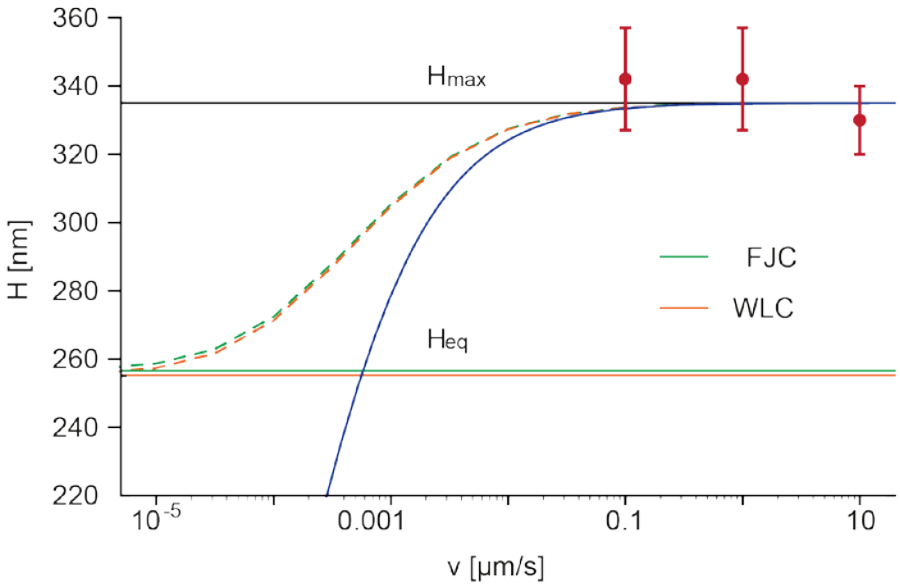


**Figure 4.9:** Plateau length measurement (red circles) for three pulling speeds are plotted together with the theoretically calculated plateau length without a re-adsorption rate (solid blue line) and with a re-adsorption rate (dashed green line for FJC, dashed orange line for WLC) $H_{eq}$ and $H_{max}$ are marked with solid lines.

For pulling speeds in the normal regime of 100 nm/s to 10 µm/s the model without re-adsorption rate describes the data well and there is no effect of pulling speed on the plateau length. This is because in all those cases the polymer is pulled close to $H_{max}$. Even considering a re-adsorption rate makes no difference in the predicted plateau length. For lower velocities of the order of 1 nm/s the plateau length falls below $H_{max}$ and gets shorter and closer to $H_{eq}$. Here taking into account the re-adsorption rate makes a difference. For the same pulling velocity in this range the plateau length is longer in the model with re-adsorption rate than without. At velocities below 1 nm/s the plateau length in the model with zero re-adsorption rate drops below $H_{eq}$, and thus the model breaks down. In this regime the re-adsorption rate has to be considered. At the pulling speed of 0.01 nm/s the plateau height would equal the equilibrium height. Those regimes are experimentally hard to achieve. At 1 nm/s with a force distance of 1 µm/s it would take 56 hours to collect 100 force curves. For

shorter chains and lower forces an effect of pulling velocity on plateau length could already be observed for higher velocities.

## 4.5 Conclusion

With the help of the two complementary protocols it is possible to determine all relevant parameters of the desorption process of polypeptides on hydrophobic surfaces. The kinetics of the desorption process are governed by the center-of-mass diffusion. Accordingly the waiting time data could be fitted with a model assuming a power-law dependence of the desorption rate on monomer number. An exponential dependence of the desorption rate on polymer length and thus the number of monomers cannot describe the experimental data.

Using the determined kinetic parameters to describe the dependence of plateau length on plateau force for the constant pulling protocol showed that in most cases for fairly long polymers (contour length of the order of 300 nm) and fairly high desorption forces (around 50-100 pN) the plateau length can be well described by $H_{max}$. This means that for most experiments the plateau length can be assumed to be $H_{max}$ and the contour length $L$ can be calculated with the WLC or FJC model if the Kuhn length a is known. $H_{max}/L$ as a function of $fa/k_BT$ is a universal curve for FJC or WLC independent of polymer length and pulling speed. Through this universal curve it is possible to determine the actual contour length $L$ of a single polymer with known Kuhn length a from a single standard desorption measurement on a hydrophobic surface in water. The plateau length is with good approximation $H_{max}$ and with the plateau force $f$ and Kuhn length $a$, $L$ can be determined. This is useful since determining the length of polymers accurately is not an easy feat. Furthermore to calculate the adsorption free energy one just has to calculate the corresponding $H_{eq}$ as a function of $fa/k_BT$ or read it from Figure 4.3 and multiply by the plateau force $f$. That $H_{max}$ describes the plateau length of long polymers better than $H_{eq}$ illustrates how far into the metastable region long polymers are pulled in typical AFM force spectroscopy measurements. The mean waiting time at equilibrium height for the longest polylysine polymer in this study was determined to be half an hour.

For slow pulling, low forces and short polymers $H_{eq}$ is a better description of plateau length and a nonzero readsorption rate has to be considered.

The fits yielded Kuhn length of polylysine of 0.63 nm for the FJC and 0.69 nm for the WLC model. For polytyrosine the fitted Kuhn length is slightly longer with 0.73 nm for the FJC and 0.77 nm for the WLC model. Those values agree well with previously published ones from theoretical calculations. [77]

Typical adsorption free energies per monomer $\lambda$ for polytyrosine on a hydrophobic SAM in water were 9.1 $k_BT$ for the FJC model and 8.2 $k_BT$ for the WLC model. Polylysine had an adsorption free energy per monomer $\lambda$ of 6.2 $k_BT$ for the FJC model and 5.8 $k_BT$ for the WLC model.

With those parameters it was possible to calculate the effective monomeric desorption rate of polylysine and polytyrosine. They are in the order of $10^5$ Hz. This is considerably smaller than monomer desorption rates which indicates a high level of cooperativity. The kinetics of the desorption of the monomer is hindered by its connection to the neighbors in the chain. This has significance for all system in which the kinetics of polymers play a role like in protein folding.

# 5 Polypeptide desorption experiments on supported lipid bilayers [78]

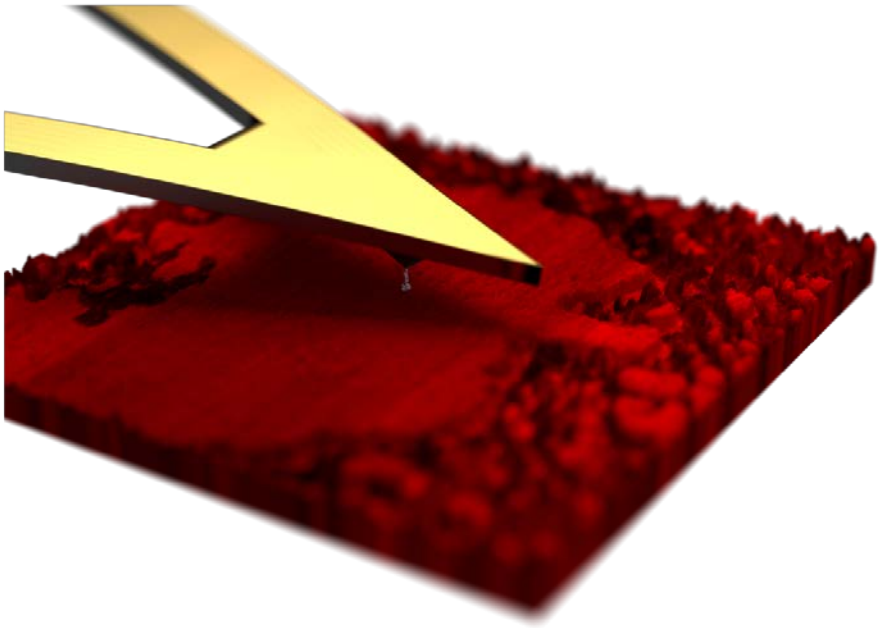

**Figure 5.1:** AFM cantilever tip functionalized with a polyhomopeptide on a supported lipid bilayer.

In the previous chapter, it was determined that the polymer desorption from hydrophobic surfaces occurs in a cooperative manner with a relatively slow monomeric desorption rate. The polymers exhibited a high mobility on the surface and as a result the force was constant during the desorption process. For this study a very well defined system was chosen. For more complicated ones like the desorption of polyhomopeptides from a lipid bilayer (illustrated in Figure 5.1) the behavior could be completely different. The lipid bilayer has a highly polarized structure that consists of two outer interfacial regions and an inner hydrocarbon core. The hydrocarbon core has a comparable width as both interfacial regions combined (30 Å) as depicted in Figure 5.2. The interfacial regions themselves have a heterogeneous chemical composition; they consist of water molecules, lipid backbone phosphate groups, the headgroups and the polar portion of the alkyl chains. This heterogeneous structure makes it possible for proteins to interact in a range of different ways depending on their location in the lipid bilayer. [27,79] Different amino acids are also expected to

have different affinities to different parts of the membrane. White et al. studied the affinity of a range of peptides to the interfacial region of the lipid bilayer by measuring the partitioning between water and unilammelar vesicles of POPC (1-palmitoyl-2-oleoyl-sn-glycero-3-phosphocholine). They found that aromatic residues are energetically favored to partition into the membrane while charged residues and the peptide bond itself are unfavored. [80] Furthermore, the lipid bilayer is not static but rather quite fluidic.

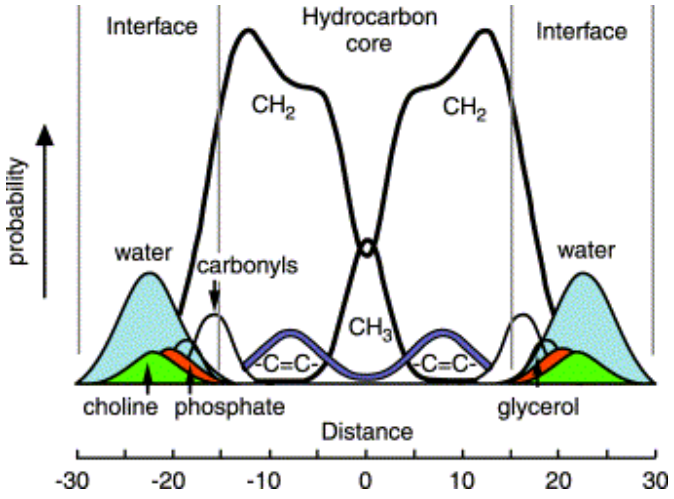


**Figure 5.2:** The figure shows the structure of a 1,2-dioleoyl-sn-glycero-3-phosphocholine (DOPC) bilayer in the liquid crystalline phase at relatively low hydration that has been determined by a combination of X-ray and neutron diffraction methods. Reproduced with permission [81]

Compared to measuring the desorption of polyhomopeptides from solid hydrophobic surfaces, single molecule desorption measurements on lipids pose additional challenges. In the case of high forces between the polypeptides and the bilayer it is possible that instead of desorbing the polypeptide from the bilayer one or more lipids are partially extracted from the membrane. So the interpretation of the force-distance curves is much more challenging.

## 5.1 Desorption forces of different polyhomopeptides on DOPC

To better understand the adhesion of proteins to membranes, measurements of different polyhomopeptides on a zwitterionic DOPC (dioleoylphosphatidylcholine) bilayer were performed. The tips were functionalized a day in advance with polyglutamic acid, polytyrosine and polytryptophan respectively. A DOPC membrane on mica was prepared and placed in a fluid cell together with a solid hydrophobic surface, e.g. PTFE or H-terminated diamond as a test surface. The test surface is necessary to calibrate the AFM cantilever. Otherwise the determination of the InVOLs on the soft lipid bilayer would not be correct. The calibration is done before and after the measurement to be able to eliminate errors in

determining the force due to change in the InvOLS over time. As a control also tips with PEG only were prepared to be able to exclude unspecific adhesion effects of the tip and the effects of the PEG linkers from the measurements of the polypeptides. As a measurement buffer 10 mM Hepes with 50 mM NaCl at pH 7 was prepared for all measurements. First force spectroscopy measurements were performed on the solid hydrophobic surface. It was checked that the known constant force plateaus are observed. This shows that the tips were functionalized successfully. Tips that showed no force plateaus were discarded. Furthermore from this measurement the plateau force and plateau length of the attached polypeptide can be determined. Then the tip is moved to the lipid bilayer and the lipid bilayer is imaged by tapping mode. This is necessary as the mica is normally not completely covered by the bilayer and holes are present. A spot on the bilayer is chosen and force distance curves are taken.

The tip is moved towards the surface until a certain trigger force value is reached and the tip stays at this point for a certain surface dwell time until retraction (Figure 5.3 B, grey). The desorption force is extracted from the retraction curve (Figure 5.3 B, red). If a high trigger force value is chosen it is possible that the tip not only deforms the bilayer but that it punctures through the bilayer. This is shown in the inset in Figure 5.3 B. Lower trigger forces of 300-500 pN were chosen to prevent puncturing the membrane and measuring interactions with the underlying mica instead of the lipid bilayer. For the effect of trigger value on the measurement see chapter 5.4. A dwell time of 4 s was chosen to give the polypeptide time to interact with the lipids and to increase the likelihood of measuring desorption events. The force curves were recorded with a cantilever speed of 1 µm/s.

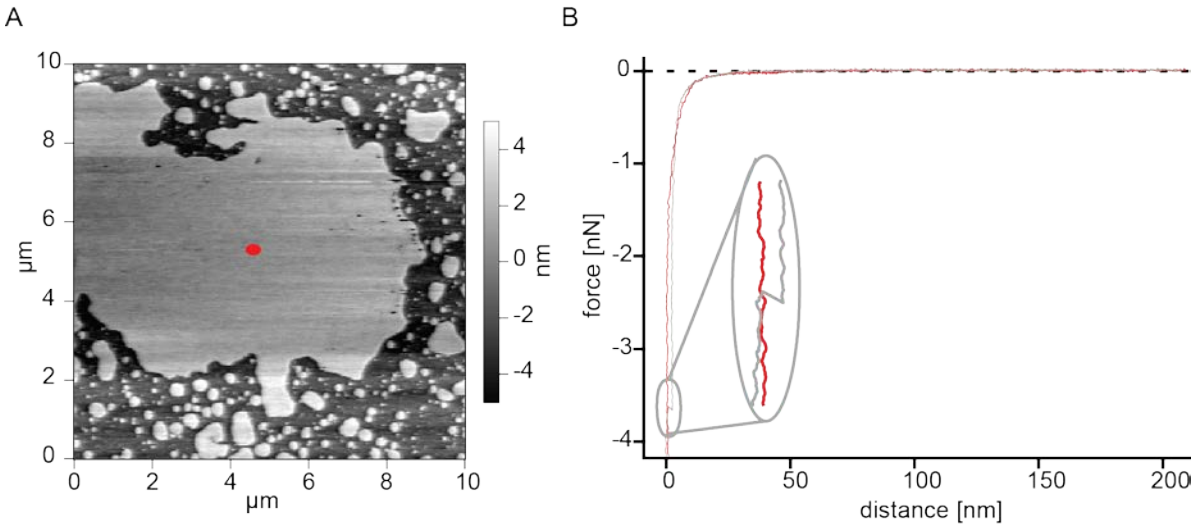


**Figure 5.3:** A shows a 10µm*10µm AFM image of a DOPC bilayer on mica. A spot for force spectroscopy measurements on the bilayer is chosen (depicted in red). B shows a extension (grey) retraction (red) force distance curve on the lipid bilayer. Due to the high trigger force the lipid bilayer is punctured. The puncturing is shown as zoomed in inset.

After the force distance curves are recorded the area is imaged again and it is confirmed that the spot is still covered by the bilayer and no drift occurred. This procedure is repeated for different measurement spots. Since it is necessary to make tapping mode images and take force spectroscopy data with the same tip a compromise on the cantilever properties has to be found. The best force resolution is achieved with larger soft cantilevers; the best tapping mode imaging quality is achieved by a high resonance frequency for which small levers are needed. On the MLCT chips the B, D, and E levers are a good compromise, for the F lever the force resolution is not good enough and with the C lever the tapping mode imaging quality is not sufficient.

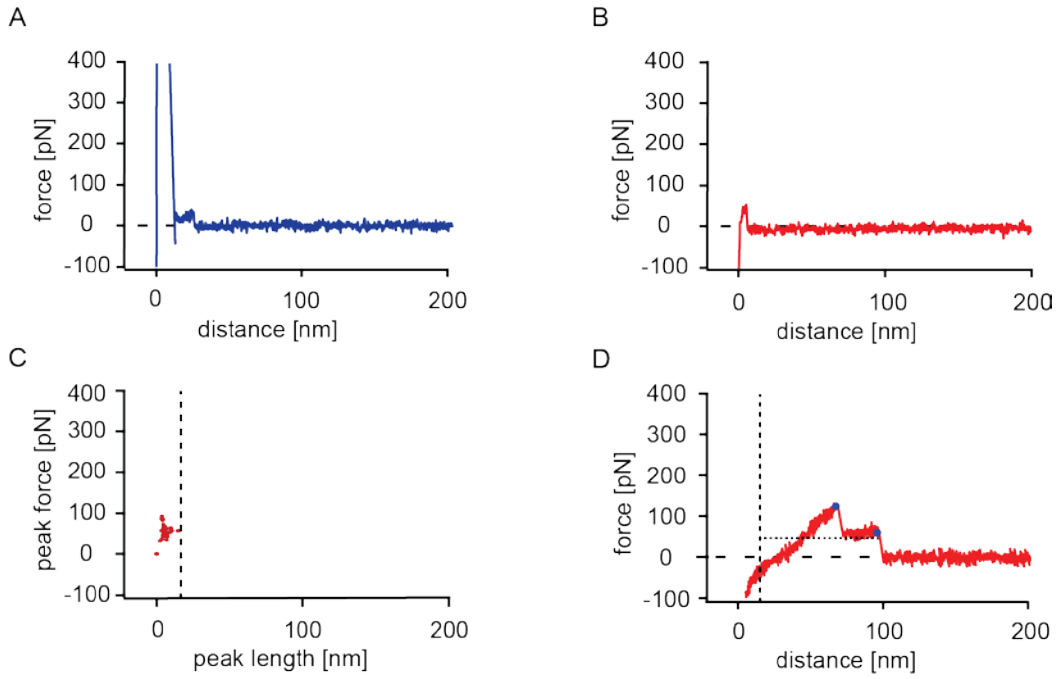


**Figure 5.4:** A and B show a sample retraction force distance trace of a 6 kDa PEG functionalized tip on PTFE and DOPC respectively. The collected sample traces of the PEG tip on DOPC were analyzed for force peaks. C shows the maximal force peaks of PEG on DOPC plotted against the peak length. No peak was further away from the surface than 15 nm. This was taken as cutoff value separating unspecific interaction from specific interactions. D illustrates how the polypeptide desorption curves are analyzed. Peaks with a distance larger 15 nm (15 nm cutoff denoted as dotted line) are determined. The peak with the highest force is extracted as maximal force (blue dot), the value of the max force is averaged over 10 measurement points to make it independent of the noise level. The last peak (largest distance to the surface) is extracted as detach peak (blue dot). The distance of the detach peak to the surface is called detach length. An average force value is extracted averaging the force over the distance beginning at the 15 nm cutoff until the detach length, the average force value is denoted by a dotted line.

Figure 5.4 shows sample retraction curves of the PEG functionalized control tip on PTFE (A) and DOPC (B). The retraction curve of PEG on PTFE shows a high force unspecific adhesion peak followed by a short low force interaction of the 6 kDa PEG. On DOPC no high force unspecific adhesion peak is observed only a short range interaction of PEG with the surface. The force retraction curves of the PEG tip on DOPC were analyzed for force peaks larger than the noise level (app. 20pN). Out of 433 curves with the standard experimental

parameters (300-500 pN trigger force, 4 s dwell on the surface, 1µm/s retraction speed) 21 desorption events were found and peak force and length were extracted. Those are plotted in Figure 5.4 C. The longest peak length out of those 21 events was 14.8 nm. To exclude unspecific adhesion effects of the tip and the effects of the PEG linkers from the measurements taken with polypeptides functionalized to the AFM tip, force peaks of less than 15 nm distance from the surface are classified as unspecific adhesion and only force peaks further than 15 nm from the surface were recorded as desorption events of the polypeptides. For the highest force peak an average over 10 data points was calculated to average out the effect of thermal noise and classified as maximal peak force. The maximal peak force and length are recorded for each curve. Additionally the last peak furthest away from the surface is extracted as detach force and the distance at this point is called detach distance. In Figure 5.4 D a sample force curve of polytryptophan on DOPC is shown and the maximal peak force and the detach peak force are marked with blue dots, the 15 nm cutoff is shown as a dashed line. Furthermore an average force was calculated over the distance starting with the 15 nm cutoff and ending at the detachment as illustrated in Figure 5.4 D.

Before and after the measurement on DOPC the polypeptides were desorbed from a hydrophobic control surface. This was hydrogen terminated diamond for polyglutamic acid and PTFE for polytryptophan and polytyrosine. Sample force curves are shown in Figure 5.5 D (polyglutamic acid), E (polytyrosine) and F (polytryptophan). All show a high force adhesion peak (less pronounced for H-terminated diamond than for PTFE since H-terminated diamond is less hydrophobic) followed by a flat force plateau. Most of the measured force distance curves on the solid hydrophobic surface have a force plateau (61% polyglutamic acid, 57% polytyrosine, 80% polytryptophan), the rest show no interaction besides the adhesion peak. On the lipid DOPC bilayer interactions were more seldom, with 32% (227/718) of polytyrosine and 17% (172/994) of polytryptophan force curves showing any specific interactions. This is especially true for polyglutamic acid with force events in only 1.7% (11/644) of the measured force curves. The shape of the force distance retraction curves on DOPC for all three polypeptides is not as clearly defined as on the hydrophobic surfaces, rather the curve shape shows large variations from one curve to the next.

The occurring motives in the force distance traces are shown for polyglutamic acid (Figure 5.5 G), polytyrosine (Figure 5.5 H) and polytryptophan (Figure 5.5 I). The percentage of each curve shape is given in the insets. For comparison known force distance motives are depicted in (Figure 5.5 A), (Figure 5.5 B) and (Figure 5.5 C). Flat force plateaus as shown in (Figure 5.5 A) often occur when desorbing linear polymers off hydrophobic solid surfaces. In the preceding chapter it is described that for plateaus of constant force the ratio between tip-surface distance and desorbed length of the polypeptide has to be constant. For this the

polypeptide needs to have a high mobility on the surface so it can be "peeled off". This is the case for the three polypeptides on the hydrophobic control surfaces but on DOPC only a few curves show flat force plateaus. This is especially true for the hydrophobic polypeptides. In case of polytryptophan and polytyrosine in only 2% of the force curves with a force event a constant force plateau was observed. For polyglutamic acid there were three force plateau curves out of 11 observed interactions. Examples of those force plateaus on DOPC are shown in the first line of Figure 5.5 G, H and I.

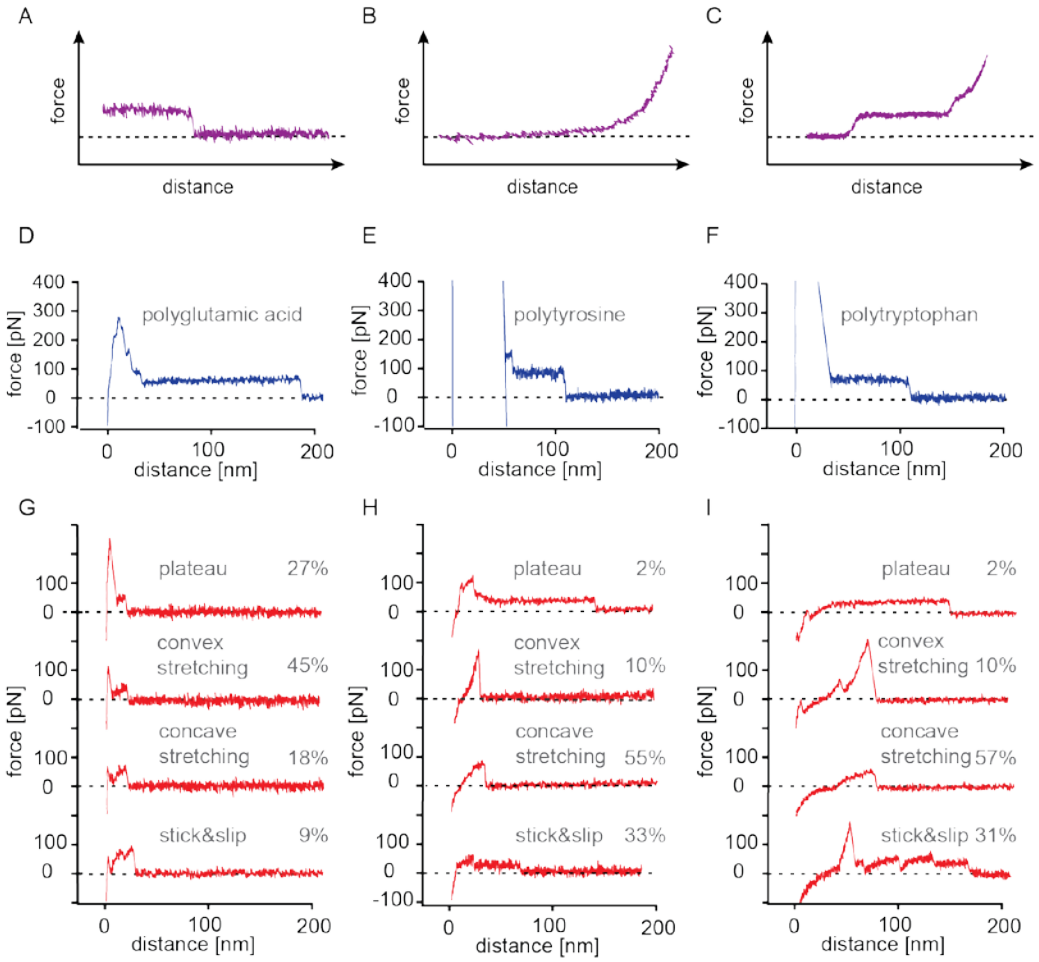


**Figure 5.5:** A, B, C illustrate the typical curve shape of a mobile polymer chain on a hydrophobic surface, of the stretching of a polypeptide chain and of the stretching of double stranded DNA respectively. A shows a flat force plateau, in B the slope of the stretching increases with distance as can be described with a WLC or FJC model, C diverges from the WLC/FJC stretching and two conformational transitions are visible. In D,E,F a sample retraction curve on a hydrophobic control surface of the tips functionalized with polyglutamic acid, polytyrosine and polytryptophan respectively is plotted. G, H and I show the different curve shapes of the desorption curves on DOPC measured with the same tips. The percentage of each curve shape is given in the insets.

If the polypeptide is bound to the surface by a strong directional force for example a covalent bond it is not mobile anymore, a peeling off is not possible and the chain between bond and tip is stretched. The stretching can be described by the FJC or WLC model. The stiffness of the elastic response increases with increased stretching. A typical WLC stretching is shown

in Figure 5.5 B. As can be seen the slope increases with distance which results in a convex curve shape. A third type of force distance curve shape is shown in Figure 5.5 C. Here also a stretching can be seen but the shape deviates from the WLC model. This is the case if conformational changes of the stretched biomolecule occur. In this example a BS transition of a stretched DNA molecule is shown. This behavior was described by Rief et al. [18] The part of the force distance curve where conformational changes occur is concave in shape in contrast to the convex WLC stretching. Other conformational transitions in force distance traces have been observed for polysaccharides or PEG chains. [19,82]

For all three polypeptides the typical convex WLC form was observed as shown in the second line of Figure 5.5 G, H and I. In case of polyglutamic acid convex stretching was observed in 5 respectively 45% of the curves. For the hydrophobic polypeptides only 10% of the force curves showed convex stretching. In case of the hydrophobic polypeptides far more often (by more than a factor of 5) the shape of the stretching is concave as in the examples plotted in the third line.

Sometimes even various motives can be seen in the same force distance curve as in the examples in the fourth line of Figure 5.5 G, H and I. The sample traces for the polypeptides on DOPC show a mix of flat force parts and parts were the force increases, e.g. the polypeptide is stretched. This could be explained by a stick slip mechanism. Periods of high mobility lead to flat or nearly flat force plateaus while a stronger directional interaction leads to stretching of the chain und thus increased force until the bond breaks. Some of the stretching parts in the force curves seem to be roughly in WLC shape. Others show a concave shape that could be an indication of a conformational change. Desorption of polypeptides from a DOPC layer is far more complex than from a solid surface. Not only the peptide could change its conformation, also the lipids could be affected by the desorption and the orientation between polypeptides and lipids could change. The force needed to fully extract a POPE lipid from a POPC bilayer is approximately 50pN. [83] It is in a comparable range to our desorption forces of the hydrophobic polypeptides from the bilayer, so it is possible that lipids could be partially extracted from the bilayer during the desorption of the polypeptide. This could be one explanation for the unusual shape of the desorption curves.

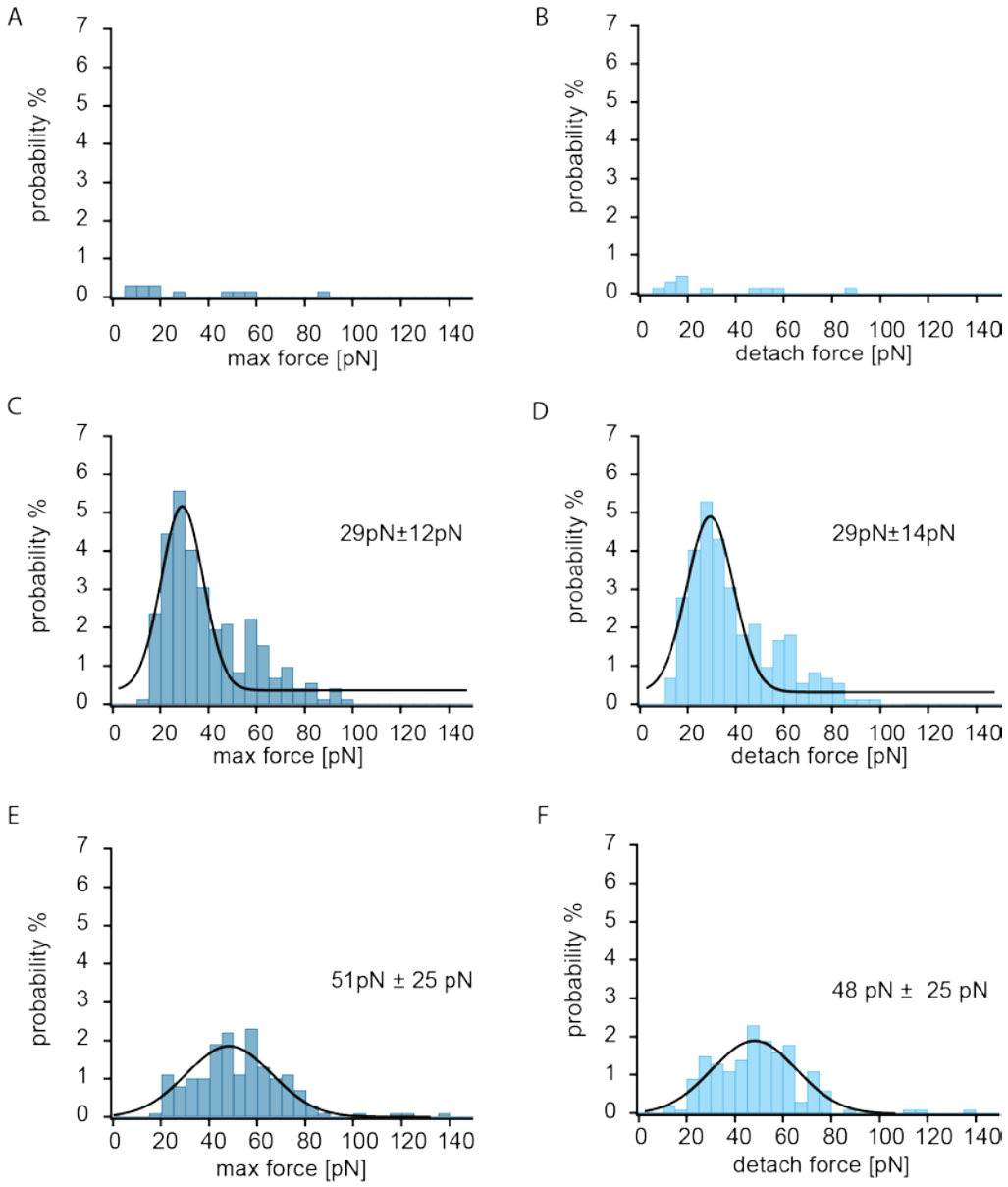


**Figure 5.6:** Histograms of the maximal force normalized to the number of collected force curves are shown for polyglutamic acid ( A), polytyrosine ( C), and polytryptophan (E). In B,D and F the detach forces of the same force curves are shown in light blue.

The extracted maximal peak forces as well as detach forces are shown in Figure 5.6 for polyglutamic acid (A, B), polytyrosine (C, D) and polytryptophan (E, F). The plots are normalized to the number of curves measured. This was 644 for polyglutamic acid, 718 for polytyrosine and 994 for polytryptophan. For polyglutamic acid adhesion events occurred very seldom. Only in 1.7% of the force curves any desorption force above the noise level could be observed. For polytyrosine and polytryptophan the probability of an event is an order of magnitude higher with 32% for polytyrosine and 17% for polytryptophan. Polytryptophan has the highest maximal force of 51 pN (as fitted by a Gaussian), followed by polytyrosine with 29 pN. For polyglutamic acid a fit of the data is not possible with just 11

data points. Most of the data points (6) are below 20 pN but there are some events of higher force. The approximate force of about 13 pN for polyglutamic acid is probably an overestimation. The small number of force events indicate that probably most events are of a magnitude too small for our setup to measure (<10 pN) and we can only see the high force tail of the distribution. This indicates that hydrophobic amino acids (tyrosine and tryptophan) are important for the adhesion of proteins to zwitterionic bio membranes. Especially the desorption force of polytryptophan from the DOPC bilayer is as high as the force needed to extract a lipid from a bilayer. The high affinity of polytryptophan to zwitterionic bilayers has been noted in the literature. [80,84,85] Interestingly, it has been observed that polytryptophan does not mainly interact with the hydrocarbon core of the bilayer but the interfacial region. [32] This is surprising considering the hydrophobic nature of polytryptophan. The nature of the attraction of polytryptophan to the interfacial region is not fully understood. Additionally to the hydrophobic effect and hydrogen bonds a cation-π interaction between the aromatic rings of the polypeptide and the sodium ion has been suggested. [31]

## 5.2 Desorption length of different polyhomopeptides on DOPC

The distance between the surface and the detach peak is determined for every force event of the polypeptides on DOPC. This detach length is compared to the plateau length of the force plateaus on the hydrophobic control surface. The length histograms normalized to the number of measured force curves are shown in Figure 5.7 B (polyglutamic acid), D (polytyrosine) and F (polytryptophan). In Figure 5.7 A, C, E the corresponding histograms of the plateau force on the hydrophobic surface and the averaged force on DOPC are plotted. The data on the hydrophobic surface is shown in blue and on DOPC in red.

For polyglutamic acid on H terminated diamond the plateau length histogram has two peaks (Figure 5.7 B) with plateau length 115 nm and 188 nm. On DOPC only one peak at 17 nm is seen in the length distribution. The reasons that not two peaks are observed could be either the low number of force events (11) or that the detach length of one polypeptide was shorter than our cutoff of 15 nm. While it is not clear which of the peaks on the hydrophobic control surface corresponds to the peak on DOPC, in both cases the length is much shorter on DOPC by a factor of about 7 respectively 11.

For polytyrosine on both surfaces only one length peak is present (Figure 5.7 D), indicating that only one polypeptide was bound to the tip. The detach length on DOPC is drastically shorter (factor of about 5) than the plateau length on PTFE.

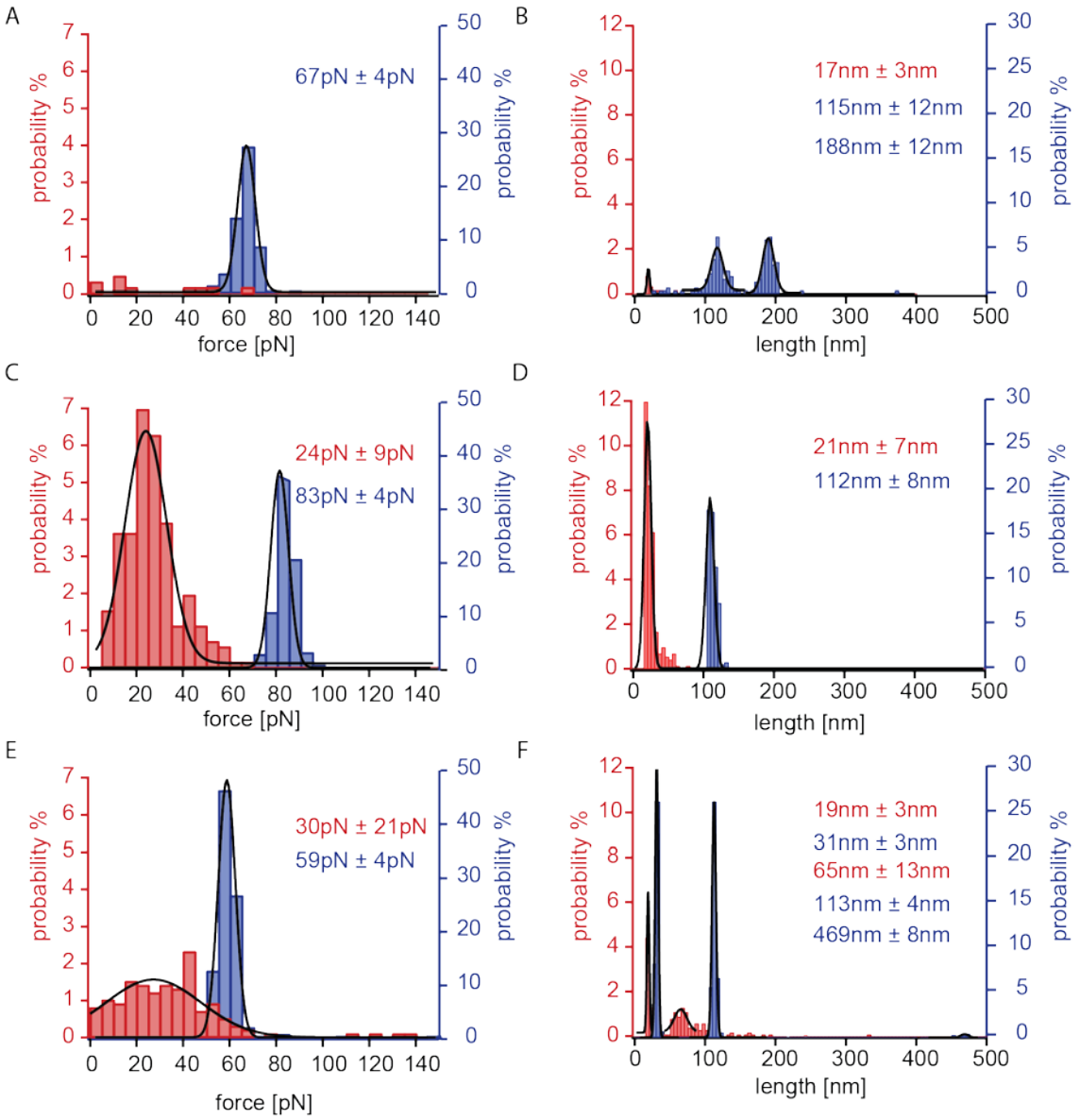


**Figure 5.7:** The histograms of plateau forces on a hydrophobic control surface as shown in blue are compared to the average force histograms on DOPC shown in red for polyglutamic acid (A), polytyrosine (C) and polytryptophan (E). For the same experiments the plateau length (blue) and detach length (red) are shown in D,B and F. The insets give the peak values as well as standard variations of the gauss fits to the peaks.

In the case of the polytryptophan functionalized tip the plateau length histograms show two peaks at 31 nm and 113 nm and more seldom a length of 469 nm (Figure 5.7 F). On DOPC two peaks with 19 nm and 31 nm corresponding to the shorter two polypeptides can be clearly identified. The length peaks of polytryptophan on DOPC are only a factor of 1.6 to 1.7 shorter than on PTFE. No clear length peak corresponding to the length of 469 nm on PTFE is observed but there are some individual events with high detach length above 100 nm on DOPC.

One possible explanation for the shorter detach length on DOPC could be due to a change in the secondary structure of the polypeptide chains. That this is caused by solvent conditions is unlikely, since the experimental conditions like pH and salt concentrations are the same on

the different surfaces. The secondary structure would have to be surface induced. Estimating the difference in detach length due to a possible secondary structure yields only about a factor of 3, when comparing for example the α-helix translation per monomer (1.5 Å) to the contour length per amino acid of 4 Å. The larger differences in length are hard to explain with secondary structure.

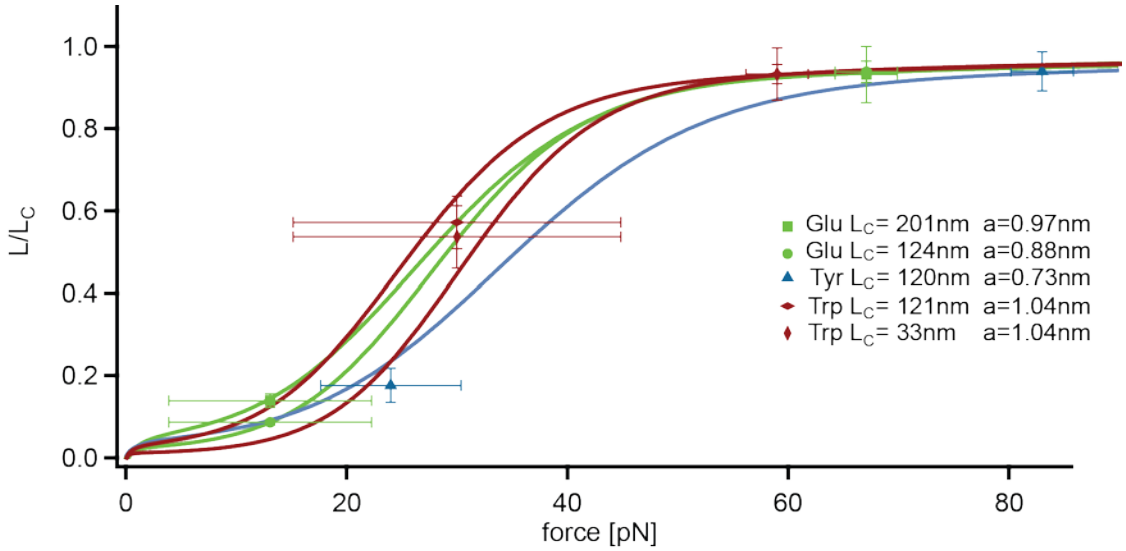


**Figure 5.8:** The detach length on DOPC as well as the plateau length on a hydrophobic surface are plotted against the average respectively the plateau force. The data belonging to the polyglutamic acid measurements are depicted in green, for polytyrosine in blue and for polytryptophan in red. Curves describing the dependence of plateau length on plateau force are calculated from equation (4.16) for the respective contour length $L_c$, pulling velocity and Kuhn length *a* given in the inset.

A simpler explanation would be to consider the energy arguments made in chapter 4 for plateau forces. At which distance it is energetically favorable to desorb, depends on the plateau force of the chain. For a lower force detachment occurs at a shorter length. In the case of the DOPC measurements the force traces only rarely showed plateaus. But since the interaction is not purely a stretching but shows stick-slip behavior, the average interaction force should influence the interaction length. When comparing force and length for the measurements on both surfaces for the different polypeptides it becomes apparent that the biggest change in length (factor of 7-11 for poly glutamic acid) corresponds to a large difference (at least a factor 5) between the average force on DOPC compared to the plateau force on the hydrophobic surface. For polytyrosine a factor of 3.5 in force corresponds to a factor of 5 in length. In the case of polytryptophan the smallest change in force (factor of 2) corresponds to a change in length of only 1.6 to 1.7. To test if the desorption process can be treated in a similar manner as plateau forces the data is plotted in Figure 5.8 together with the calculations of the detachment length according to equation (4.16). For $H_{max}$ the plateau length of the measurement on the hydrophobic control surface is taken and the kinetic

parameter $\omega$ = 25nm$^2$/s, determined in chapter 4 for polytyrosine and polylysine on a hydrophobic surface in water, is used. Using the force on the hydrophobic control surface and the known force dependence of ω as well as the pulling velocity and the Kuhn length a the detachment length can be calculated for the whole force range. For polytyrosine the Kuhn length is determined in chapter 4 to be 0.73 nm in the FJC model. The calculated curve for the polytyrosine chain is shown in Figure 5.8 in blue. The measured average force and detachment length on DOPC lies on this curve within the accuracy of the measurement. This means that the kinetic diffusivity parameter determined on a hydrophobic surface can also describe the data on the DOPC bilayer.

For polyglutamic acid as well as polytryptophan the exact Kuhn lengths are not known. Because of this the Kuhn length was treated as a free parameter and the formula (4.16) was fitted to the data points. For polyglutamic acid it is not clear which peak on the hydrophobic surface corresponds to the peak on DOPC. Both possibilities are fitted as shown in green. For polytryptophan it is unambiguous which peak corresponds to which. Both sets of data points are fitted and the Kuhn length of the two fits averaged. The calculated graphs with the averaged Kuhn length are plotted for the two chains with differing length as shown in red. The contour lengths calculated from $H_{max}$ and the force on the hydrophobic surface as well as the Kuhn lengths for the different polypeptide chains are given in the inset of Figure 5.8. The fitted Kuhn lengths lie in a reasonable range of 0.88 nm to 1.04 nm. This means that all three data sets, measured with different polypeptides of different lengths can be described reasonably well with the theory developed in chapter 4. This indicates that the magnitude of the kinetic parameter, the scaling of the kinetics with polymer length and the cooperativity of the polypeptide chain on DOPC is roughly comparable to those of the polypeptides on a hydrophobic surface. Additional experiments on DOPC in the manner of the waiting time measurements made for polypeptides on solid hydrophobic surfaces could give further insight into similarities and differences in the kinetics on the different surfaces.

## 5.3 Velocity dependence of most probable desorption forces on DOPC

According to the Bell model discussed in chapter 2.3, the rupture forces of bond stretching are dependent on the force loading rate and thus on the pulling speed of the AFM experiment. To test the velocity dependence of the polypeptide desorption from the bilayer, measurements with three different pulling velocities 0.1 µm/s, 1 µm/s and 10 µm/s were

performed with polytyrosine and polytryptophan. Due to the low number of desorption events this measurement was not possible in a reasonable time frame with polyglutamic acid. The dwell time on the surface was chosen to be 4 s and the trigger force 500 pN. As discussed in chapter 5.1, the desorption force-distance traces of polypeptides on DOPC show a variety of curve shapes. This can be explained by a stick-slip interaction of the polypeptide on DOPC. During a stick event the force on the bond increases. How fast the force increases with time is called the force loading rate. Since the shape of the curves in the experiment is not uniform, the loading rate of different curves measured with the same pulling velocity is not the same. To account for this the instantaneous loading rate is determined for every force curve at the maximal force of the curve. The highest force peak, with the maximal force, is the part of the curve where a bond was stretched and broken and the force subsequently decreased. This can be the last interaction of the trace (detach force) or it can be followed by a stick or slip of lower force. The analysis of the force curves is illustrated in Figure 3.13 A in the methods section. It shows how the highest force peak of the force distance curve is determined. Then the same curve is plotted as force time trace (Figure 3.13 B) and the instantaneous loading rate is determined as the slope of the linear fit to the 50 measurement points before the maximal force peak. 50 measurement points are chosen so that the fit is independent of the noise level. 50 points corresponds to a tip travel distance of 10 nm.

This analysis is performed for the 0.1 µm/s, 1 µm/s, 10 µm/s pulling speed measurements of polytyrosine and polytryptophan on the DOPC bilayer. The maximal force and corresponding loading rate of each curve are plotted in a linear against logarithmic graph in Figure 5.9 for polytryptophan and in Figure 5.10 for polytyrosine. The 10 µm/s measurement points are depicted as green squares, the 1 µm/s as yellow squares and the 0.1 µm/s as blue squares. The loading rates for the different pulling velocities are broadly distributed and even overlap. The data points are sorted into 4 groups depending on loading rate ($<10^{-10}$ N/s, $10^{-10}$-$10^{-9}$ N/s, $10^{-9}$-$10^{-8}$ N/s, $>10^{-8}$ N/s). Histograms of the maximal forces are plotted for each loading rate range as shown in Figure 5.9 for tryptophan and Figure 5.10 for tyrosine with histograms in the range $<10^{-10}$ N/s (B) , $10^{-10}$-$10^{-9}$ N/s (C) , $10^{-9}$-$10^{-8}$ N/s (D) and $>10^{-8}$ N/s (E). From each force histogram the most probable force is extracted. When the statistics are sufficiently good for a fit, the most probable force and its standard variation are determined by a Gaussian fit to the data and in other cases the value of the highest peak in the histogram is taken and the standard variation calculated.

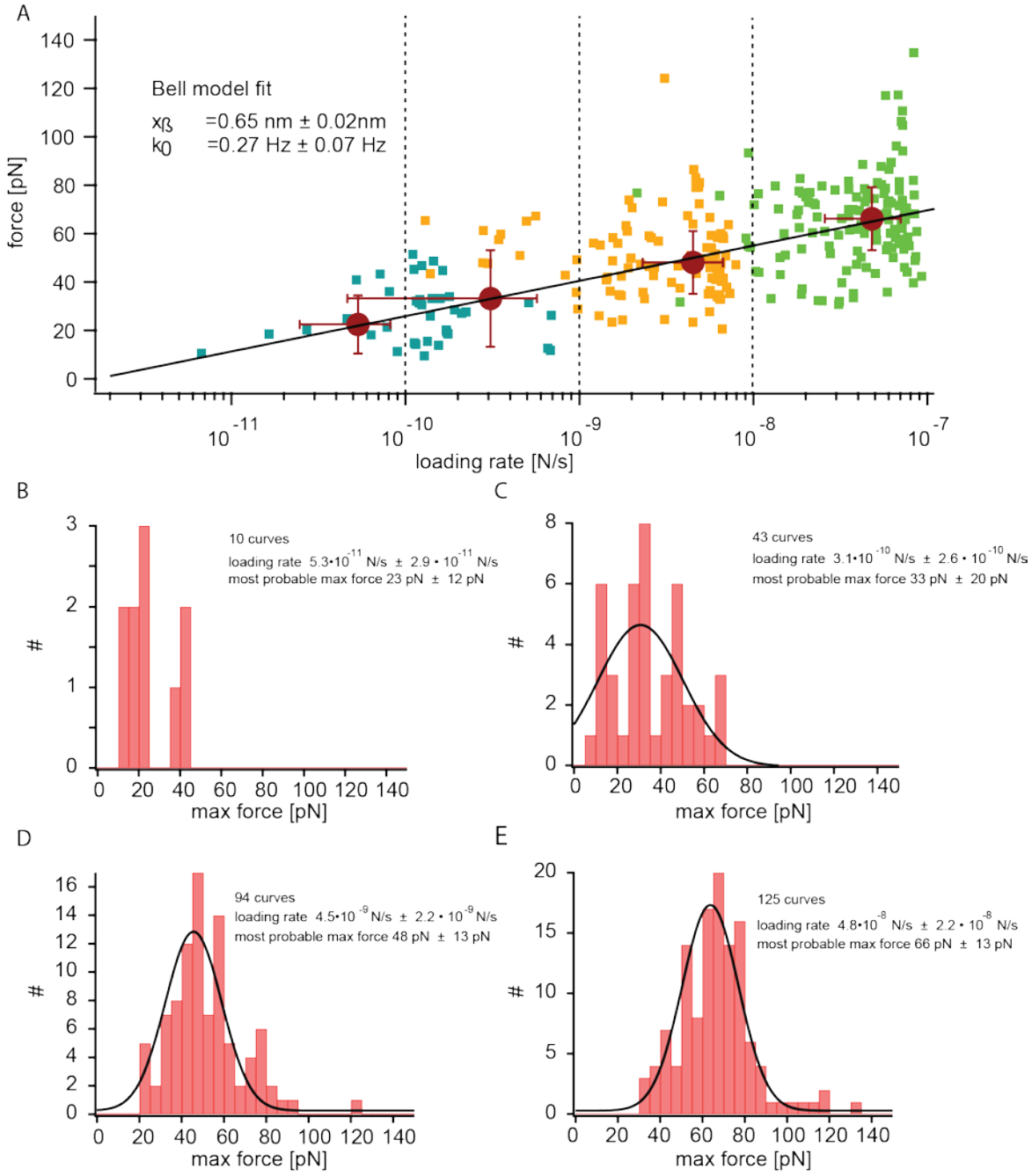


**Figure 5.9:** The maximal force and corresponding loading rate of polytryptophan on DOPC of each curve are plotted in a linear against logarithmic graph in A. The data collected with pulling velocity 0.1µm/s is plotted in blue, the 1µm/s data in yellow and the 10µm/s in green. The data points are sorted into 4 groups depending on loading rate (<$10^{-10}$ N/s, $10^{-10}$-$10^{-9}$ N/s, $10^{-9}$-$10^{-8}$ N/s, >$10^{-8}$ N/s) as denoted by dotted lines. Histograms of the max forces are plotted for each loading rate range. In B the max forces for loading rate range <$10^{-10}$ N/s are plotted, in C for $10^{-10}$-$10^{-9}$ N/s, D for $10^{-9}$-$10^{-8}$ N/s and E for >$10^{-8}$ N/s. The most probable force is extracted for each histogram and plotted against the average loading rate of the range in A, both are given in the insets of the histograms. The standard deviation of the most probable forces and loading rates are taken as errors. The four data points are fitted with the Bell model and the fit values for bond rupture distance and transition rate are given as insets in A.

The average loading rate for the data points in each group is calculated together with the standard variation. Four values for the most probable force at a certain loading rate are plotted in Figure 5.9 A for polytryptophan and Figure 5.10 A for polytyrosine with the standard variation as error and fitted with the Bell model.

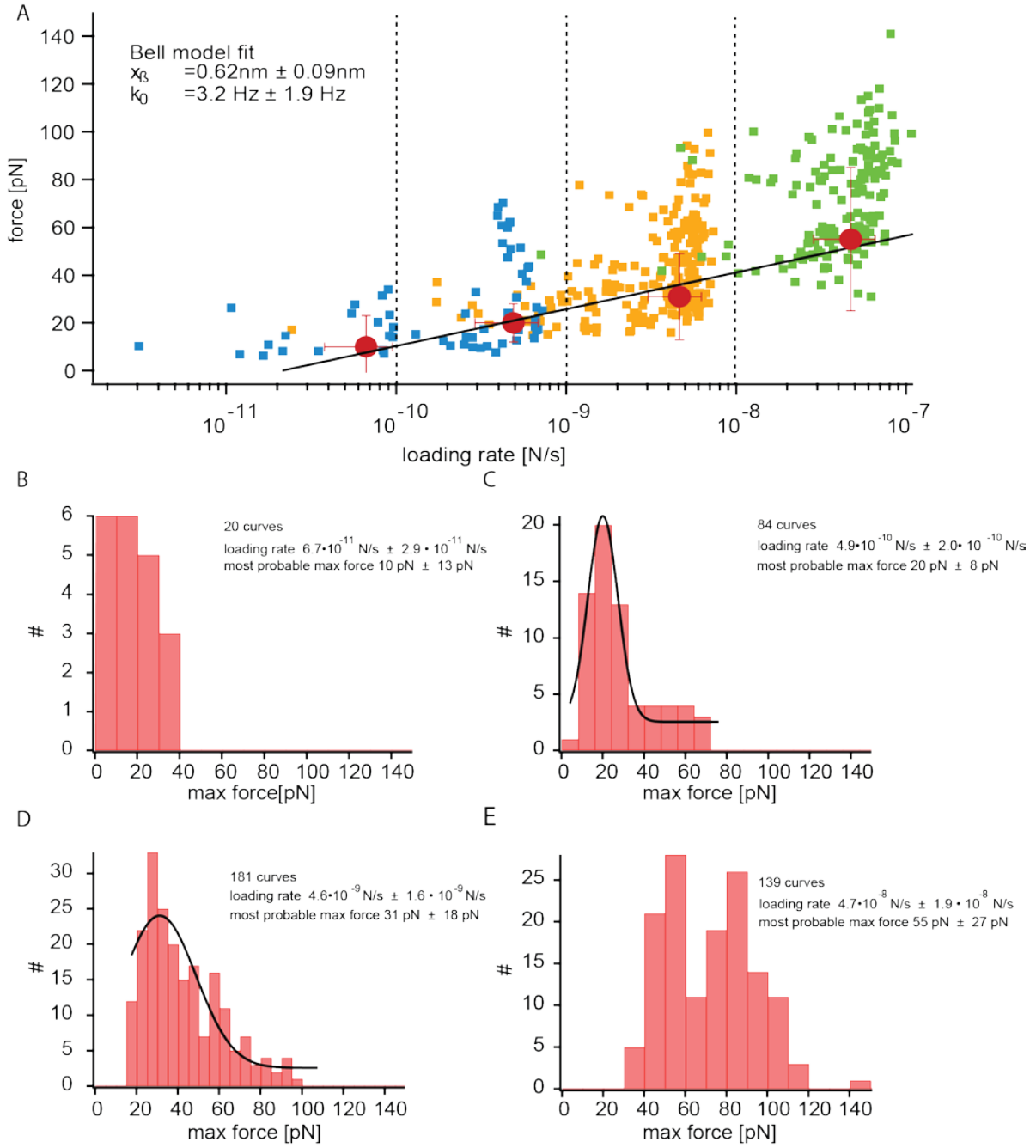


**Figure 5.10:** The maximal force and corresponding loading rate of polytyrosine on DOPC of each curve are plotted in a linear against logarithmic graph in A. The data collected with pulling velocity 0.1 µm/s is plotted in blue, the 1 µm/s data in yellow and the 10 µm/s in green. The data points are sorted into 4 groups depending on loading rate (<$10^{-10}$ N/s, $10^{-10}$-$10^{-9}$ N/s, $10^{-9}$-$10^{-8}$ N/s, >$10^{-8}$ N/s) as denoted by dotted lines. Histograms of the max forces are plotted for each loading rate range. In B the max forces for loading rate range <$10^{-10}$ N/s are plotted, in C for $10^{-10}$-$10^{-9}$ N/s, D for $10^{-9}$-$10^{-8}$ N/s and E for >$10^{-8}$ N/s. The most probable force is extracted for each histogram and plotted against the average loading rate of the range in A, both are given in the insets of the histograms. The standard deviation of the most probable forces and loading rates are taken as errors. The four data points are fitted with the Bell model and the fit values for bond rupture distance and transition rate are given as insets in A.

The Bell model is described in chapter 2.3. An applied force tilts the energy landscape and thus the transition rate from bound to unbound state depends on the magnitude of the force applied. In an experiment were a stick occurred the applied force is not constant but

increases with time. While the probability to desorb only depends on the instantaneous force the probability to be still bound at this point depends on the force in the past and thus the loading rate. In an ideal case the force-stretch response of the linker is exactly known and is the same for all force curves. Then the loading rate at each time and the probability to be bound can be calculated for each point of the curve. This is not the case here. Due to the varying curve shape the instantaneous loading rate at rupture is determined by a linear fit as discussed previously. This is a valid approximation since the highest probability for the bond to break is at higher forces, so the last part of the curve is most important. A constant loading rate (force ramp) is assumed and by setting the derivative of the probability to be bound at force *f* to zero, an expression for the most probable rupture force is derived in equation (2.28) as $f^* = \frac{k_B T}{x_\beta} ln\left[\frac{r_F x_\beta}{k_0 k_B T}\right]$.

This logarithmic function is fitted to our four data points of polytryptophan and polytyrosine. Free fit parameters are $x_\beta$ and the transition rate $k_0$. The results of the fits are given as insets in Figure 5.9 and Figure 5.10 A. For polytryptophan the fitted unbinding distance is 0.65 nm and for polytyrosine 0.62 nm. Those values are large compared to typical values for covalent bonds (0.1-0.2 nm) and are more consistent with longer range interactions like the hydrophobic effect. They are also of a comparable size to the Kuhn length of polytyrosine (0.7 nm). The fit showed that the values for the transition rate are different by about a factor of 10. The fitted $k_0$ equaled 0.27 ± 0.07 Hz for polytryptophan and 3.2 ± 1.9 Hz for polytyrosine. From these values it is possible to estimate the activation free energy or energy barrier $\Delta U$ of the bond. In order to do that one has to know the Arrhenius prefactor A. In chapter 4 the effective monomeric desorption rate was determined to be in the order of $10^5$ Hz for polytyrosine. A monomer here means a unit of the size of the Kuhn length that is about 1.5-2 residues on a polypeptide chain. Using this value as the Arrhenius prefactor yields activation free energies of 13 $k_BT$ for polytryptophan and 10 $k_BT$ for polytyrosine. It should be noted that those values have a high uncertainty due to the fit procedure and the choice of the Arrhenius prefactor.

## 5.4 Variation of dwell time and trigger force for polytryptophan on DOPC

Besides the pulling velocity two additional parameters of the measurement could influence the results. The first one is the trigger force, which determines how much the membrane is deformed by the tip and with how much force the polypeptide on the tip is pushed into the membrane. The trigger force has to be chosen in a way that the tip does not puncture the membrane. This puncturing of the membrane is apparent in the extension force trace by a sudden reduction of the repulsive force combined with change in distance of about 4 nm. With high trigger forces in the nanonewton regime puncturing of the membrane occurs. The other parameter is the dwell time which describes for how long the tip is kept in contact with the membrane at the trigger force.

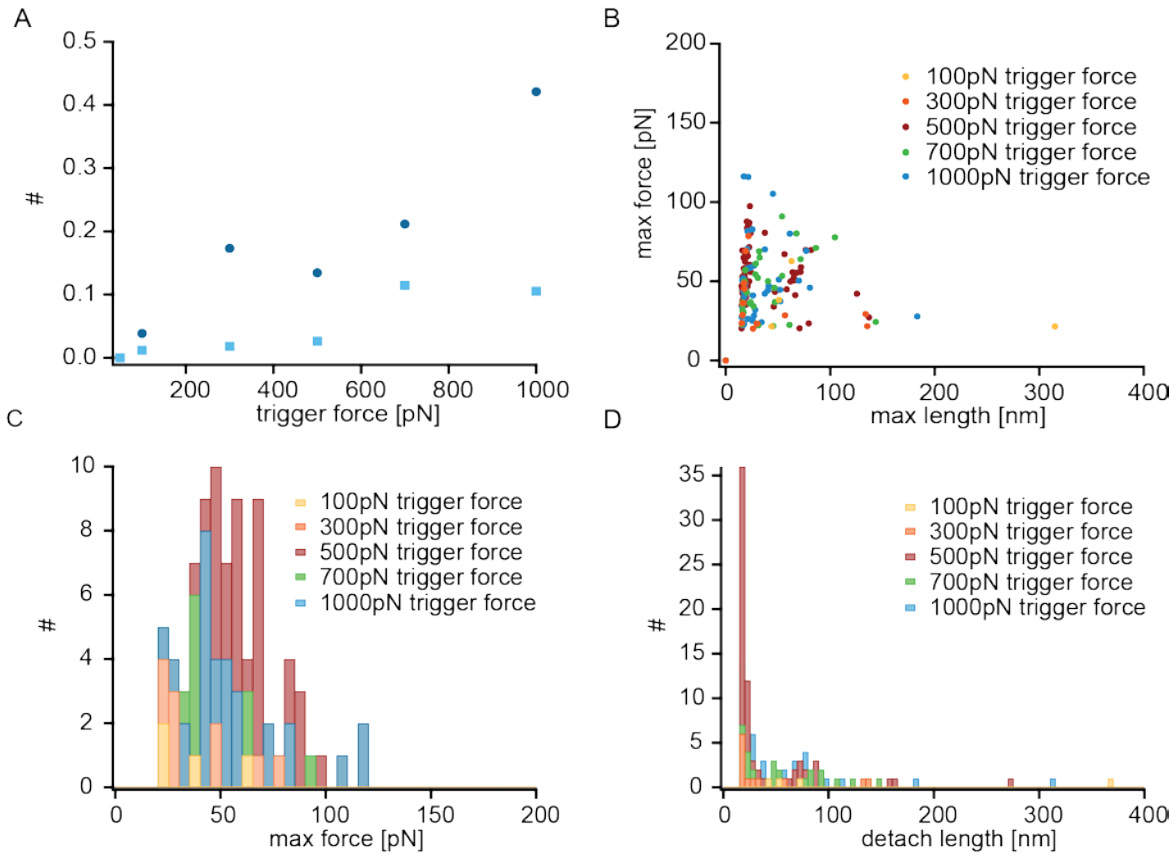


**Figure 5.11:** The polytryptophan desorption experiments were repeated for different trigger forces on the DOPC membrane with constant dwell time (4 s) and constant pulling velocity (1 µm/s). A shows the probability to observe a desorption event for the different trigger forces. Two measurement series with the same tip at different times on different spots on the same sample are shown in light and dark blue. B shows a scatter plot of the maximal force versus length at maximal force with the different trigger forces depicted in different colors (see inset). C shows the histogram of maximal force for each trigger force. In D the histograms of the detach length for different trigger forces are shown.

In the experiments mentioned in the previous section the trigger force was chosen to be 500 pN and the dwell time 4 s. Now those two parameters are systematically varied. To avoid time effects a number of curves are collected for each parameter in a random order. This is

repeated again in a different order, at a different time and on a different spot on the membrane.

The results for the trigger force measurement series are shown in Figure 5.11. As can be seen in Figure 5.11 A the probability for the polypeptide to adhere to the membrane, so that a desorption event can be observed, depends strongly on the trigger force. For a very low trigger force of 50 pN no desorption events were observed for either of the two measurements. While the probability of a desorption event differs quite strongly between the two measurements series, within each series there is the trend of a higher event probability with an increasing trigger force. In Figure 5.11 B a scatter plot of max force against length is shown. No distinct difference between the trigger forces can be observed. They have similar max forces and similar detach lengths, as can also be clearly seen in the histograms in Figure 5.11 C and D. To summarize the trigger force has a strong influence on the number of desorption events but seems to have no effect on the maximal desorption force and the detach length.

In a similar manner the dwell time at constant trigger force of 500 pN was systematically varied. The results are plotted in Figure 5.12. Here again the probability to observe a desorption event strongly depends on the dwell time. In both measurements (shown in light and dark blue in Figure 5.12 A) the probability to observe an event increases linearly with the dwell time. In the scatter plot in Figure 5.12 B differences between the dwell times can be observed. Some of the 4 s measurement curves depicted as green dots show uncharacteristically large forces at similar max length of nearly 100 nm. Those values belong to a batch of WLC like, stick type curves. As reported earlier this type of curves is relatively seldom observed as can also be seen in the green 4 s dwell time max force histogram depicted in Figure 5.12 C. The forces bigger than 150 pN are individual values and a clear force peak can be observed for lower force values. More interestingly, there seem to be differences in force and length as a function of the dwell time which can be seen in the scatter plot as well as the max force (Figure 5.12 C) and detach length histograms (Figure 5.12 D). The longer the dwell time, the higher the max force and the longer the max as well as the detach length. The max force histograms for 1 s, 4 s and 10 s dwell time show distinct peaks with increasing max force values. The peaks have been fitted with a Gaussian. In Figure 5.12 C the fit is depicted in black and the peak values as well as the standard variations are given in the inset. The difference in max force between 1 s (41 pN ± 16 pN) and 4 s (58 pN ± 17 pN) dwell is bigger than between 4 s and 10 s (69 pN ± 26 pN) indicating that the increase in force is not linear in dwell time at least for larger dwell times. The max force distribution for 10 s is broader than for 1 s and 4 s. In the detach length distributions shown in Figure 5.12 D the peaks are not so well defined. Still it can be observed that for

longer dwell times the detach lengths are shifted to longer lengths. In summary for longer dwell times more events at higher force with a longer detach length can be observed, as discussed later.

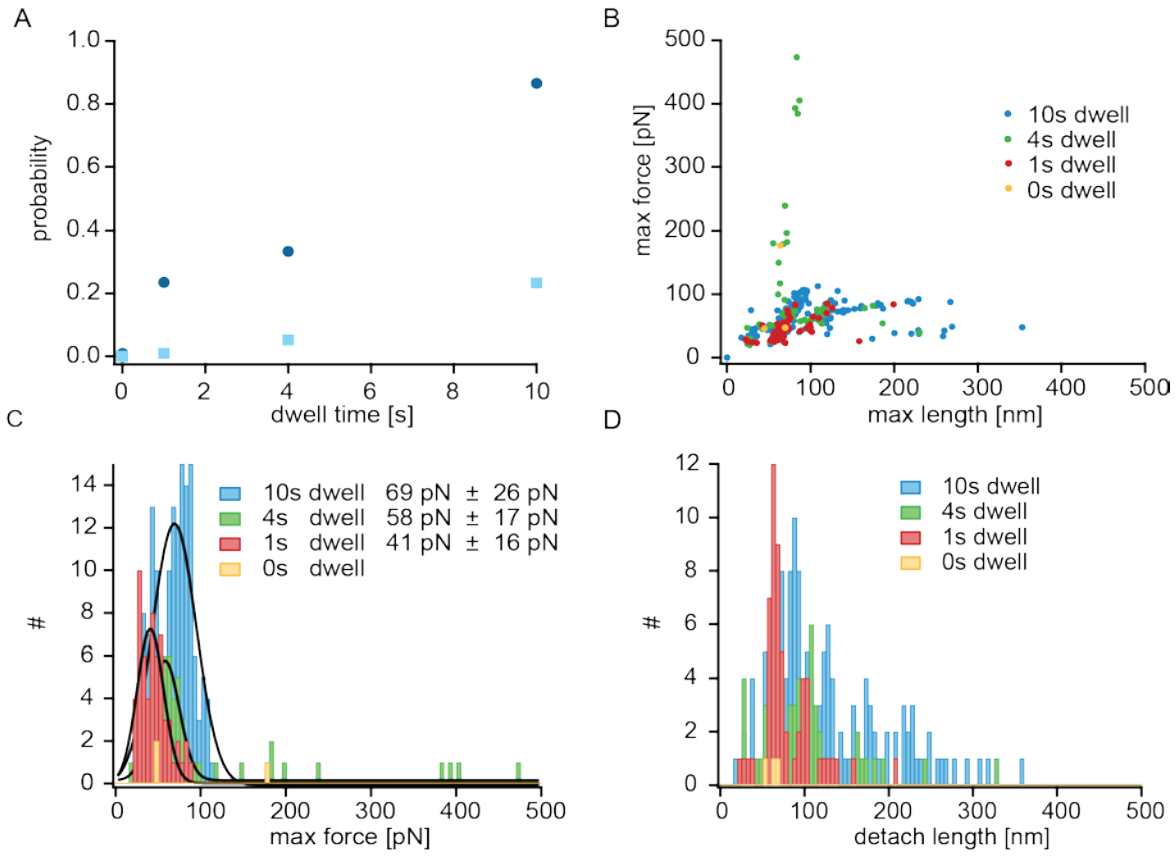


**Figure 5.12:** The polytryptophan desorption experiments were repeated for different dwell times on the DOPC membrane with constant trigger force (500 pN) and constant pulling velocity (1 µm/s). A shows the probability to observe a desorption event for the different dwell times. Two measurements with the same tip at different times on different spots on the same sample are shown in light and dark blue. B shows a scatter plot of the maximal force versus length at maximal force with the different dwell times depicted in different colors (see inset).C shows the histogram of maximal force for each dwell time. A Gaussian fit is shown in black where possible, the values of the peak force and standard variation are given as insets. In D the histograms of the detach length of the dwell times are shown.

That no desorption events could be observed for the smallest trigger force of 50 pN indicates that polytryptophan in our system cannot spontaneously adhere to the DOPC headgroups from solution during the 4s dwell time with a desorption force measurable in our setup (>10pN). That the probability of the desorption events strongly depends on trigger force and dwell time supports the assumption that polytryptophan needs to be incorporated into the membrane to observe desorption events and that it is interacting with the interfacial region and the hydrocarbon core. A difference in the probability of the desorption events as well as the maximal force between 4 s dwell time and 10 s dwell time indicates that some adhesion

processes occur on a slow time scale. This could be the diffusion into the membrane or the relaxation to an energetically favorable conformation in the membrane. The change in detach length could be explained in two different ways. The polytryptophan tip used in this experiment has 3 polytryptophan chains of different contour lengths (app 33nm, app 121nm and > 469 nm as determined in chapter 5.2). It is plausible that the interaction with the longest polymer can be more often observed at longer dwell times since the diffusion into the membrane is slower for longer polymers. This explains why most of the detach length larger than 121 nm belong to the 10 s and 4 s dwell measurements. Furthermore for each polypeptide the part of the contour length that can be observed as detach length depends on the desorption force as discussed in chapter 5.2. Since the max force changes with dwell time, this explains why each polypeptide chain shows varying detach lengths for different dwell times.

## 5.5 Desorption of Phospholipase A2 from DOPC/DOPS

After studying the adhesion of polyhomopeptides on a DOPC membrane the next step to understanding protein membrane interactions is to bind a protein to the tip and measure the interaction with the DOPC zwitterionic membrane. The phospholipases A2 are a relatively well studied and commercially available group of enzymes that reversibly bind to phospholipid membranes and can catalyze their hydrolysis. It has been proposed that secreted phospholipases A2 share a structurally similar interfacial binding surface surrounding the active center. While the structure is similar the amino acid sequence varies quite a lot between the different phospholipases. [36] The sPLA2 of cobra venom and of honey bee venom have several hydrophobic aromatic residues in the vicinity of the interfacial binding surface. Considering the measured high desorption forces for polytryptophan and polytyrosine on DOPC similar high desorption forces of sPLA2 from cobra venom and honey bee venom can be expected. The measurements were performed in the same way as the polypeptide experiments. The functionalization was tested on a hydrophobic PTFE surface, the DOPC surface was imaged and spots on the membrane chosen for force spectroscopy measurements. The measurements were performed with a pulling velocity of 1µm/s, a dwell time of 4s and a trigger force of 100-500 pN. As a measurement buffer 10 mM Hepes and 50 mM NaCl at pH 7 was used. The measurements were performed at room temperature.

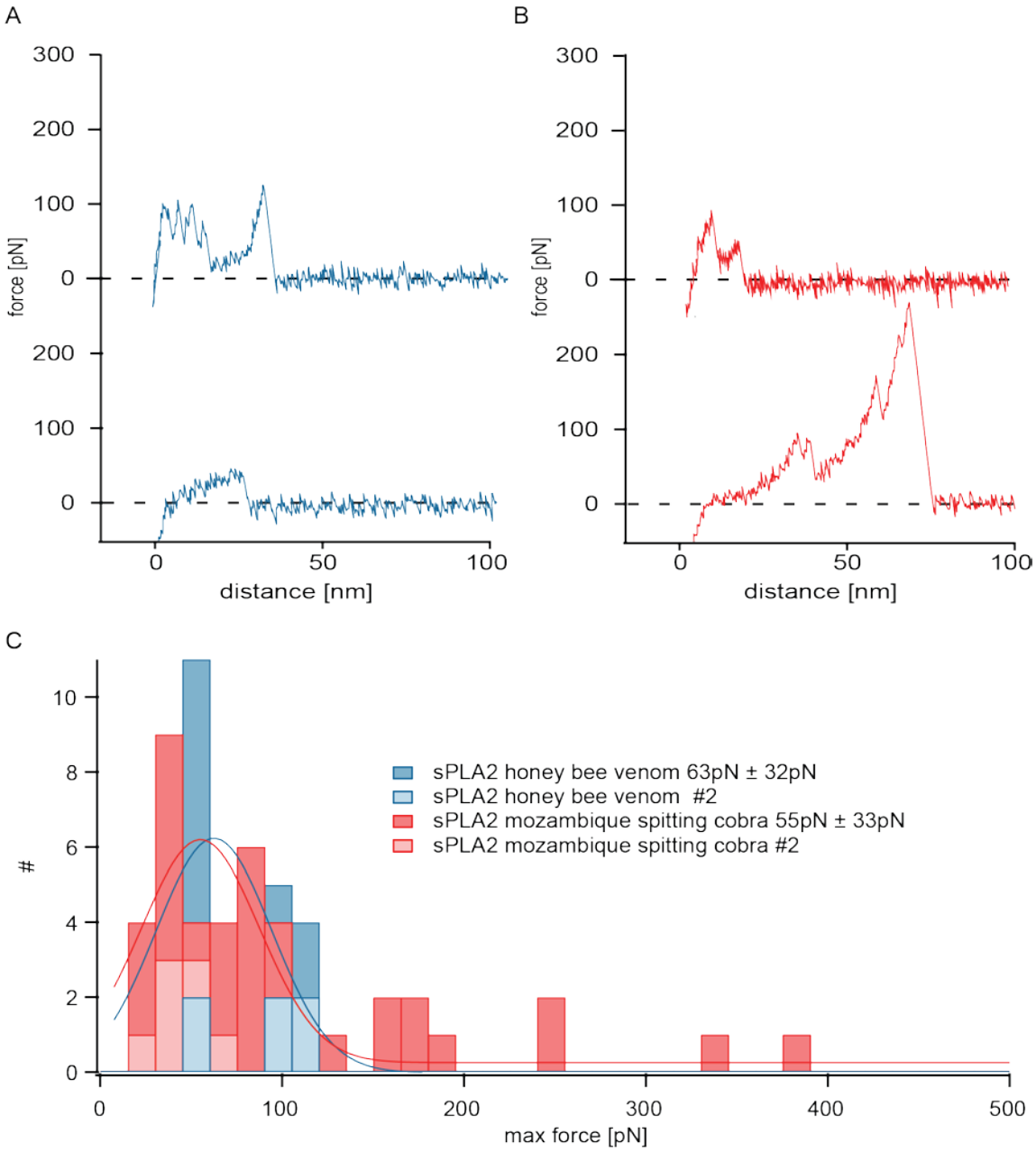


**Figure 5.13:** A shows two sample force distance traces of sPLA2 from the honey bee venom on DOPC, in B traces from sPLA2 from the mozambique spitting cobra are shown. In C the histograms of the max forces for two measurements each for both sPLA2s on DOPC are shown. The measurements with the better statistic were fitted with a Gaussian and the values are given in the inset.

In Figure 5.13 the results for two measurements each with sPLA2s from honey bee venom (depicted in blue) as well as the Mozambique spitting cobra (depicted in red) are shown. Contrary to the polyhomopeptide experiments the WLC stretching motive was observed more often as can be seen in the above trace in Figure 5.13 A for the honey bee sPLA2 and in B for the cobra sPLA2. Sometimes non WLC stretching events like in the second trace of Figure 5.13 A were seen. For the cobra venom sometimes exceptionally high forces were measured as seen in the second trace of Figure 5.13 B.

Most of the traces show max forces between 20 pN and 120 pN. The gauss fit of the honey bee venom sPLA2 measurement gives 63 pN ± 32 pN, for the cobra venom sPLA2 55pN ± 33pN. Those values are somewhat higher than the maximal desorption forces of polytryptophan on DOPC and the 50 pN needed to extract a POPE lipid from a POPC membrane. Only in the case of the cobra venom occasional high force events with forces in the range of 150-400 pN were observed. The corresponding curves were all of a WLC stretching shape and show a structure of smaller ruptures that could be caused by domain unfolding. The probability to observe a desorption event was low for all measurements making it hard to obtain sufficient statistics.

It has been found that $Ca^{2+}$ is necessary for the activity of secreted phospholipase A2 while there are other results that indicated that $Ca^{2+}$ is not necessary for the binding of the sPLA2 to membranes. [34] To test the dependence of the adhesion on $Ca^{2+}$ the measurements with the same functionalized tip of sPLA2 from cobra venom was performed in a 10 mM Hepes 50 mM NaCl buffer without $Ca^{2+}$ and again with a very high concentration of 50 mM $CaCl_2$. The histograms for the maximal force values are depicted in Figure 5.14. No significant difference is observed in the desorption forces supporting the findings that $Ca^{2+}$ is only necessary for activity and not for binding.

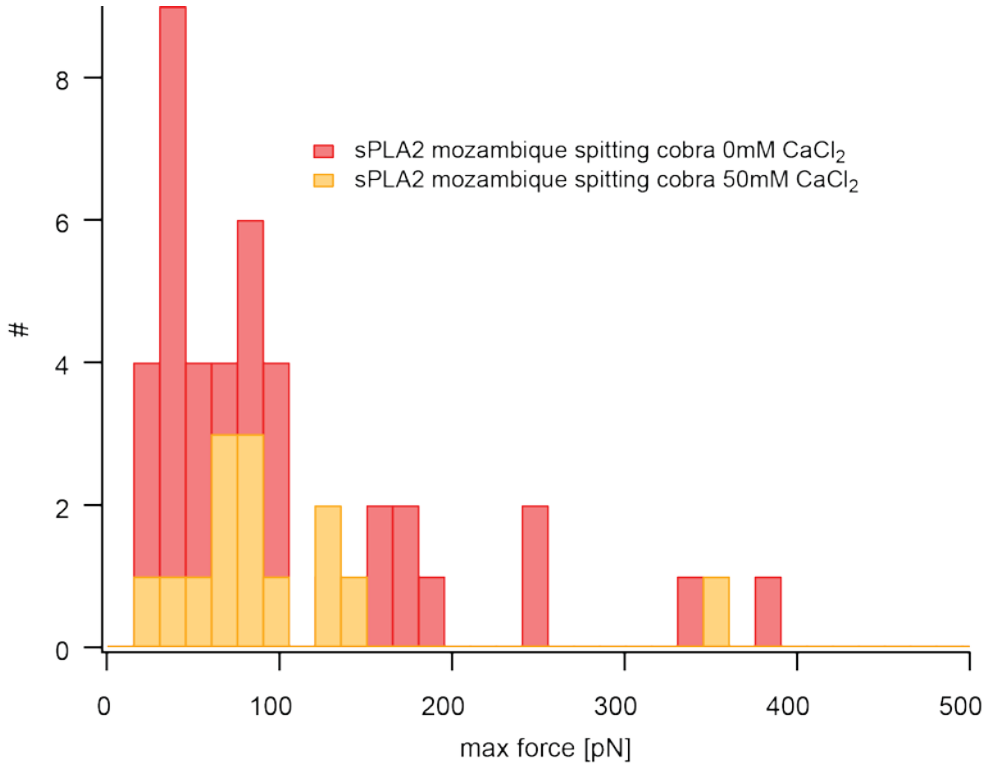


**Figure 5.14:** Force spectroscopy measurements of a tip functionalized with sPLA2 from cobra venom were performed on DOPC in measurement buffers containing 0mM $CaCl_2$ (max force histogram shown in red) and 50mM $CaCl_2$ (max force histogram shown in yellow).

Numerous individual phospholipases have been identified and they show varying degrees of affinity for anionic or zwitterionic membranes. The sPLA2s from honey bee venom and from cobra venom have shown a much higher affinity to zwitterionic than to charged membranes. Therefore we performed experiments to compare the desorption forces on pure zwitterionic DOPC membranes with forces on membranes containing 20 molar% charged DOPS. Figure 5.15 contrasts the measured maximal forces on 20% DOPS with two measurements containing only DOPC for both sPLA2s. Surprisingly the forces on DOPC and DOPS/DOPC are very similar. A possible explanation for this could be an asymmetric distribution of DOPS in the two bilayer leaflets. It has been described that the negatively charged PS lipids can accumulate in the leaflet proximal to the mica surface and thus are depleted in the distal leaflet. [86] That indicates that the added DOPS has a much smaller concentration than 20% on the distal leaflet and only a negligible effect on the adhesion of the sPLA2s. Repeating the measurements on a different support surface than mica (for example $SiO_2$) could give more insight on this.

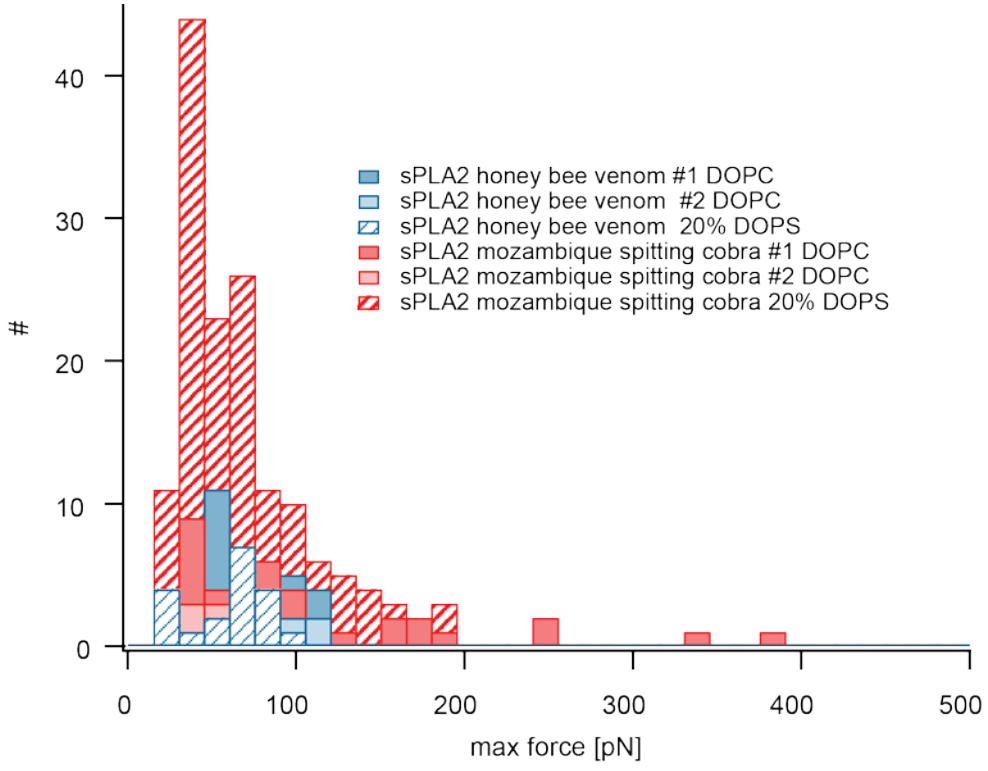


**Figure 5.15:** The maximal force histograms of 3 measurements each of sPLA2 from honey bee venom (blue) and mozambique spitting cobra venom (red) are shown. The two measurements each on DOPC show very similar values to the measurements on DOPC mixed with 20 molar % of DOPS. The honey bee sPLA2 measurement #1 on DOPC was performed with the same tip as the measurement on 20% DOPS. The cobra sPLA2 measurement #2 on DOPC was performed with the same tip as the measurement on 20% DOPS.

## 5.6 Conclusion

The experiments with the three polyhomopeptides showed that the chains with hydrophobic aromatic residues polytyrosine and polytryptophan have a much higher affinity for the zwitterionic lipid bilayer than the charged polyglutamic acid. This could not only be observed in the form of lower forces for polyglutamic acid but mainly by the one order of magnitude lower probability to observe a desorption event. Of all three polypeptides polytryptophan clearly showed the largest desorption forces. This agrees well with the partitioning hydrophobicity scale developed by White et al. [80] and underscores the special relevance that tryptophan has for the interaction with the interfacial region in the lipid bilayer.

The shape of the force distance traces itself gives valuable information on the adhesion mechanism of polypeptides on the lipid bilayer. The overall mobility of the polypeptides on the lipid bilayer was lower than on solid hydrophobic surfaces since the force distance traces did not show exclusively force plateaus, as was the case on hydrophobic solid surfaces, but a mix of stick and slip.

The maximal peak forces of the “sticking” interactions for the aromatic polypeptides show a logarithmic dependence on the loading rate as described in the Bell model. Fitting the model to the data gives distances between the bound and transition state in the order of 0.6 nm. This is significantly longer than for covalent bonds and it could hint towards a more long range hydrophobic interaction between the aromatic residues and the lipid bilayer.

The differences between detach length on DOPC and plateau length on the hydrophobic control surfaces can be explained using the same kinetic two state model as in chapter 4 with the determined kinetic parameters. That the model fits the data well could indicate that the scaling of the desorption rate with chain length and the cooperativity of the chain is similar on the lipid bilayer and on the hydrophobic surfaces.

Using the monomeric desorption rate in the range of $10^5$ Hz determined in chapter 4 as the Arrhenius factor in the Bell model yields activation free energies of approximately 10 $k_BT$ respectively 13 $k_BT$ for polytyrosine and polytryptophan.

The high desorption forces of phospholipase A2 from the honey bee venom and the mozambique spitting cobra on DOPC showed the expected high affinity for the zwitterionic membrane and underline again the importance of aromatic residues in the adhesion of proteins to zwitterionic membranes. In the future it would be interesting to compare those

results with additional experiments with the phospholipase A2 from group IIA which instead of aromatic residues contains charged residues on the interfacial binding surface.

# 6 Desorption of biomimetic dendritic adhesives

*Part of this chapter is published in the following publication: Krysiak, S.; Wei, Q.; Rischka, K.; Hartwig, A.; Haag, R.; Hugel, T., Adsorption mechanism and valency of catechol-functionalized hyperbranched polyglycerols. Beilstein J. Org. Chem.,* ***2015****, 11, 828* [87]

While the adhesive properties of mussels inspire the design of new biomimetic adhesives it can in some cases be unwelcome. The biofouling of marine vessels leads to high cost because of increasing drag. This is one case where an affordable and nontoxic antifouling coating is desired. The design of a good antifouling coating has to satisfy several specifications. There have to be functional groups that facilitate a strong adhesion under the needed circumstances, here underwater. The long term stability has to be high, that means the use of reformable bonds that show a degree of self healing is desirable. Those properties are well fulfilled by catechol groups. Furthermore for self healing to work molecules have to be attached via several bonds. Here a branched design with several catechol groups is a promising solution. As an added benefit the oxidation of catechol to quinons makes crosslinking possible and leads to a good cohesion of the layer.

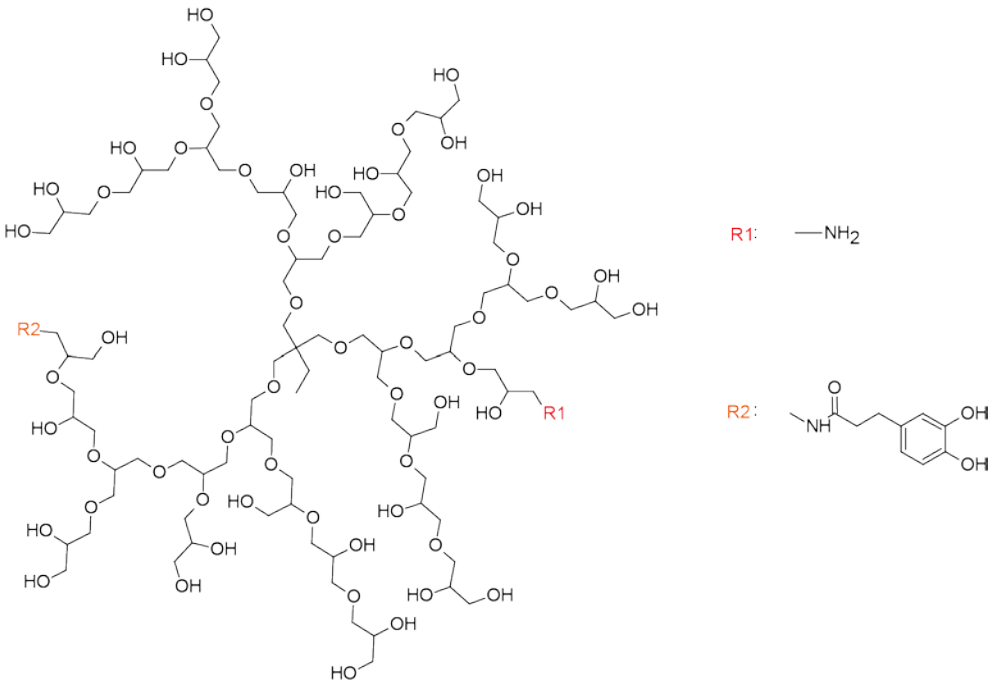


**Figure 6.1:** Schematic of a hyperbranched polyglycerol**.** hPGs are functionalized with differing amounts of amino groups for attachment to the tip and catechol groups for better adhesion.

To develop such an antifouling coating hyperbranched polyglycerol was functionalized with catechol groups as depicted in Figure 6.1. Hyperbranched polyglycerol was prepared by Qiang Wei in the group of Prof. Haag. The hyperbranched polyglycerol was prepared with a

molecular weight of 5kDa. This construct contains about 100 -OH endgroups. Those endgroups were substituted for different numbers of amino and catechol groups.

## 6.1 Desorption force of dopamine from $TiO_2$

The publication by Lee et al. [8] sparked considerable interest and since then several research groups have published results of single molecule atomic force measurements of dopa or dopa containing constructs on metal oxide surfaces. The forces reported show large variations between 67 pN and 805 pN. The reasons for this are unclear and this underscores how little is known about the nature of the interaction between the catechol group of dopa and metal oxide surfaces.

Table 6.1 summaries the published force values and gives some detail on the constructs and the measurement conditions. It is striking that both research groups using polymers with dopa sidechains measured relatively small desorption forces of 67 pN and 77 pN respectively. The other two labs measured with single dopa residues on a linker respectively a peptide containing dopa. They reported forces in the range of 640 pN to 805 pN. The histograms of those force measurements were very broad with standard deviations of about 150 pN. Some of the listed publications do not state all measurement parameters like the surface dwell time which could have an influence on the force. All give either the pulling velocity or the force loading rate in the moment of rupture.

| Research group | Construct | Buffer | Surface Dwell [s] | Loading rate or velocity | Force [pN] | Surface |
|---|---|---|---|---|---|---|
| Messersmith [8] | Single DOPA PEG linker | $H_2O$ | ? | 6e-8 N/s | 805 ± 131 | $TiO_2$ |
| | | pH 8.3 20mM Tris HCl | ? | | 206 ± 66<br>759 ± 88 | |
| Butt [88] | Polymer with DOPA sidechains | 1mM $KNO_3$ pH 6.8 | ? | 1µm/s | 67 | $TiO_2$ |
| Wang [89] | Polymer with DOPA sidechains | 100mM Tris 50mM NaCl pH 7.2 | 1s | 1µm/s | 77 | $TiO_2$ |
| Börner [90] | Spacer 12mer peptide containing two dopa | 0.8mM potassium phosphate pH 6.7 | 4s | 0.1µm/s | 640 ± 140 | $Al_2O_3$ |

**Table 6.1:** The table summarizes the published values for single molecule desorption forces of dopa constructs from metal oxides measured with AFM single molecule technique.

To determined the force of a single catechol group on titanium dioxide we performed AFM single molecule force spectroscopy measurements with tips functionalized with dopamine. Dopamine is derived from L-Dopa by removing the carboxyl group. This leaves an amine group which was used to couple the probe molecule covalently to the tip via a PEG linker using NHS-ester chemistry as illustrated in Figure 6.2 A. A sample force distance trace showing the retraction of the tip from the $TiO_2$ surface is shown in B.

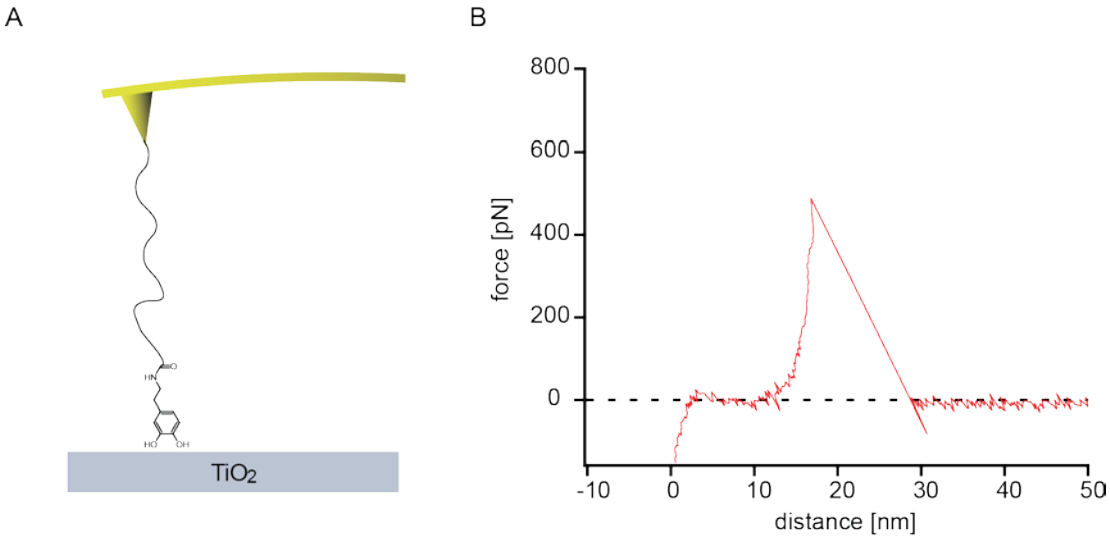


**Figure 6.2:** A shows a schematic of the dopamine desorption experiment. The dopamine is covalently coupled to the tip with a PEG linker using NHS ester chemistry and desorbed in buffer from $TiO_2$. In B a sample retraction force distance trace of the desorption of dopamine from $TiO_2$ is shown.

The experiments were performed at room temperature with a constant pulling velocity of 1µm/s and a dwell time on the surface of 1 s. Different buffers were used for the measurements. McIlvaines buffer solutions (a mix of 100 mM citric acid and 200 mM $Na_2HPO_4$) at pH values between 3 and 8 were used as well as phosphate buffered saline (PBS) and ultrapure water. Maximal peak forces (max force) as well as detach forces were extracted.

Figure 6.3 A shows max force histograms of measurements for one dopamine functionalized tip on $TiO_2$ in buffer solutions of different pH. For low pH 3 and pH 4 a large number of curves showed high force events and clear high force peaks are visible in the histograms. For higher pH values desorption events were more seldom observed and mostly at lower forces. For all pH values occasional high force (>300 pN) events were observed but for measurements in pH 5-8 not enough were recorded to see a clear high force peak in the histograms. The pH 8 measurement shows a small peak at 300 pN. Figure 6.3 B shows measurements with a second dopamine functionalized tip in ultrapure water, PBS and in citric acid/phosphate buffer at pH 3. The measurement in ultrapure water shows a very broad distribution of desorption forces with no distinct peak. There are small peaks at approximately 40 pN, 140 pN and 320 pN as well as occasional high force events up to 750

pN. The measurement with the same tip in PBS at pH 7.4 shows a clear bimodal force distribution with peaks at 290 pN and 410 pN and a shoulder at approximately 650 pN. With the same tip at pH 3 a high force peak at 500 pN with a force shoulder at about 700 pN is measured.

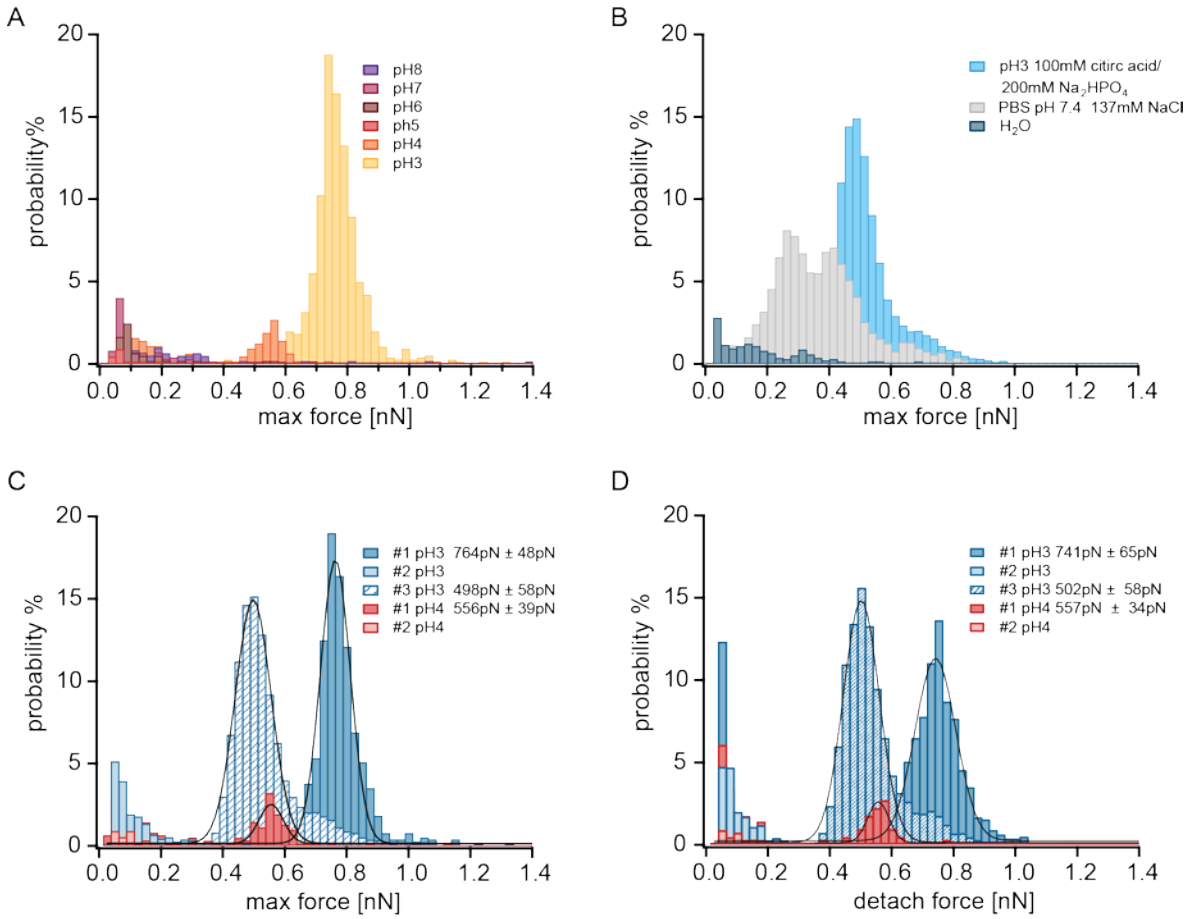


**Figure 6.3:** A shows the maximal desorption forces of a dopamine functionalized tip on $TiO_2$ in citric acid/phosphate buffers of different pH. The histograms plotted in yellow to violet belong to pH values raging from 3 to 8 as depicted in the inset. In B histograms of max forces for a second dopamine functionalized tip with the three measurement buffers ultrapure water (dark blue), PBS (grey) and citric acid/phosphate buffer pH3 (light blue). C and D show the max respectively detach force histograms of 3 dopamine tips, 2 in buffer solutions of pH3 and pH4, 1 only at pH3 as described by the insets. 3 measurements had good enough statistics to fit a Gaussian to a high force peak, peak value as well as standard variation are given in the insets.

With the two dopamine tips a variety of force values were measured. This is further proof that the catechol group can interact in a number of different ways with the titanium dioxide surface. While the original measurement of 805pN by Lee et al. was performed in water, our measurement in water showed no high force peak. Due to the missing buffering capacity of ultrapure water, small contaminations can change the pH in unpredictable ways. This and the strong pH dependence of the high force interaction make it hard to reproduce the measurement in ultrapure water. The measurement in PBS shows a bimodal distribution similar to the bimodal distribution measured by Lee and coworkers in buffer of pH 8.3. They attributed the high force peak (759 pN ± 88 pN) to unoxidized dopa and the lower force peak

(206 pN ± 66 pN) to oxidized dopa-quinon. Similar to the measurement of Lee et al. the higher forces in our measurement occurred at the beginning of the measurement and the lower ones towards the end. This would point to oxidation over time. An increasing pH shifts the equilibrium between dopa and dopa-quinon towards the oxidized quinon. Other theories describe two different pH dependent interactions involving “lying down” and “standing up” conformations of the catechol on $TiO_2$. Another possibility is the oxidation to a semiquinon radical. While the lower force peak values are roughly comparable (290 pN vs. 206 pN) our high force peak is considerably smaller than the one of Lee et al. (410 pN vs. 759 pN). Reasons for this could be differences in experimental parameters like force loading rate or surface dwell time. In the pH measurements the low pH 3 and pH 4 showed clear high force peaks and a high probability of a desorption event. At this pH one can be reasonably sure that the dopa is not oxidized. The peaks at pH 3 and pH 4 have different forces at 760 pN and 560 pN.

Since the force histograms at low pH give clear high force peaks and the interaction can be associated with the unoxidized dopa, comparing several measurements in the pH range 3-4 is a good way to identify the high force interaction between a single dopa and the titanium oxide surface. Of the five measurements with three tips at pH3 and 4, three show clear high force peaks in max and detach force (Figure 6.3 C and D). One tip showed interactions at low forces but only very seldom interactions at high forces. Maybe the dopamine on this tip got oxidized during the tip functionalization procedure. The other three measurements give max forces of 498 pN ± 58 pN, 556 pN ± 39 pN and 764 pN ± 48 pN. It is a reasonable assumption to identify the first two as single dopa $TiO_2$ interactions and the second one as the interaction of two dopas on two PEG linkers with $TiO_2$. Slightly different linker length would mean that the force of two dopa, on two linkers is less than double the force of one. Further indication that the 760 pN peak is the result of two catechol groups, is the high force shoulder of the 560 pN measurement. This could mean that in this measurement occasionally also multiple dopamines ruptured. While the detach force did not change from the max force for the other two measurements the detach force of the higher force measurement is slightly shifted to lower forces (740 pN instead of 760 pN).

Some of the measured force distance curves did not show the expected WLC stretching shape but a more complex shape that indicated several interactions with tethers of differing length. One such curve is shown in Figure 6.4 A. The rupture is not smooth but interrupted by another interaction with a longer tether (see circle). All curves of the measurement were analyzed for inter rupture forces. The average value of the inter rupture forces is smaller than the average value of the detach forces as can be seen in Figure 6.4 B. Figure 6.4 C illustrates how the interaction of several dopamine add up to a combined force. The detach

force is larger than the inter rupture force but in most cases less than 1.5 the inter rupture force. This means that the forces add up not ideally since the tethers have different length and the force load is not distributed equally. This proves that the force peak is higher due to interactions with more than one dopamine.

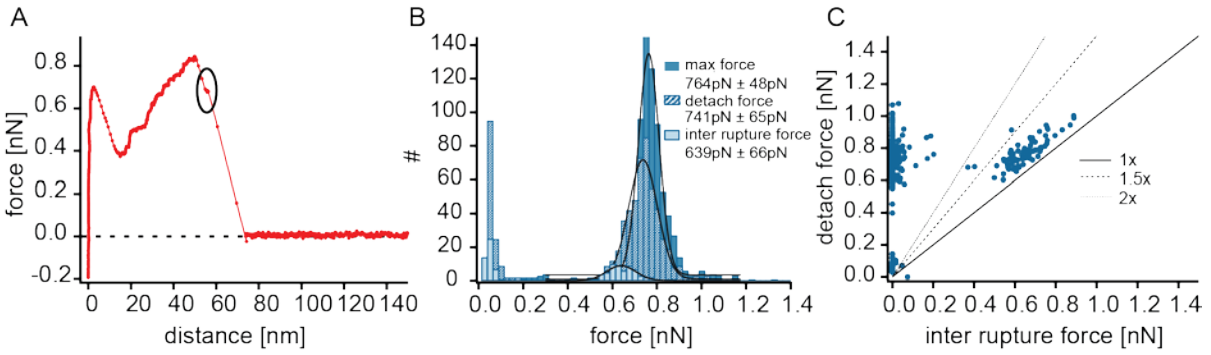


**Figure 6.4:** A shows a force distance traces of the pH 3 dopamine measurement on $TiO_2$ with a small cluster of measurement points during the rupture indicated by the circle. B shows different force histograms for the measurement with gauss fit values given in the inset. C plots the detach force of each measured force event against the inter rupture force.

In summary for ultrapure water no clear peak was observed, in PBS at pH 7.4 interactions of oxidized and unoxidized dopa were measured and measurements in the range of pH 3-4 showed forces between a single unoxidized catechol group and the titanium dioxide surface in the range of 530 pN ± 140 pN for a pulling velocity of 1µm/s and a surface dwell of 1s. The measured forces that are even lower than the 200-300 pN associated with the dopa-quinon titanium dioxide interaction could be due to a single hydrogen bond or a weak hydrophobic interaction of the aromatic ring or even some interaction of the PEG linker.

## 6.2 Desorption of different catechol functionalized architectures from $TiO_2$

For a good coating it is beneficial to have several anchor points of a macromolecule on the surface. This makes it possible that if one bond fails, the macromolecule is held in place by the other bonds and gives the bond the chance to reform. This is at least possible for reversible binding as was demonstrated for catechol and titanium oxide. [8] Furthermore a branched structure gives the possibility of increased cohesion due to possible crosslinking and it is possible to introduce additional chemical groups for engineered functionalities. It is interesting to study how the functional catechol groups are best incorporated in a macromolecule to ensure good adhesion.

For this reason the desorption of single catechol groups on a flexible linker from titanium dioxide is compared to the desorption of a linear chain containing 45% catechol sidegroups (app 12 kDa) and to a hyperbranched polyglycerol with 40% catechol endgroups (app 10

kDa). Since the cleanest desorption peaks for catechol groups in chapter 6.1 were observed for measurements at low pH, Mc Ilvaines buffer at pH 3 was used for all measurements.

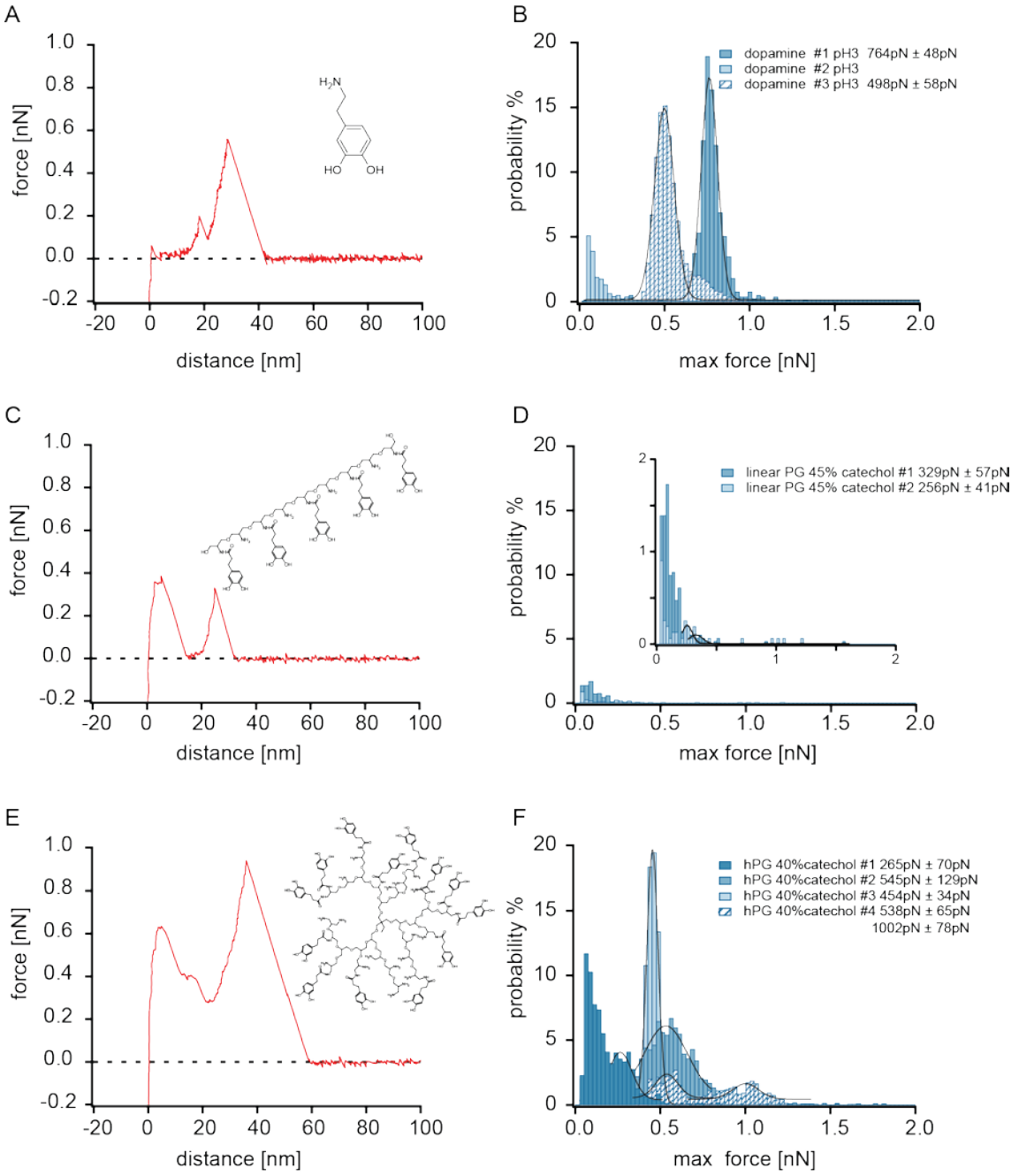


**Figure 6.5:** In A, C, E sample force distance curves and schematics of the different catechol constructs are shown. In B, D and F the corresponding histograms of the maximal force during desorption is depicted. The force histograms are normalized to the number of measured curves. 2 to 4 measurements were made for the different constructs and are labeled in different shades of blue. If possible, peaks with forces over 200 pN were fitted with a Gaussian and the peak values as well as the standard deviation are given in the insets.

Figure 6.5 shows sample force distance curves for the different constructs with a schematic of the construct as inset. A shows the single catechol group, C the linear polyglycerol (PG) and E the hyperbranched polyglycerol (hPG). In B the histograms for the maximal forces for the 3 measurements of the single catechol are plotted. The histograms are normalized to the

number of measured curves. Two of the three measurements show high force peaks. One measurement shows only small forces. In D the force histograms of the linear catechol functionalized polyglycerol are shown. It is striking that the probability to observe an event is about an order of magnitude lower. A zoom in to the histogram is shown as inset. In addition to the low probability to observe any desorption event the observed forces were mostly smaller than 200 pN for both measurements. A small number of curves form a peak at about 300 pN and there are occasional cases of high force events at 500 pN, 1 nN and one event even above 1.5 nN. In F the force histograms of four measurement of the catechol functionalized hyperbranched polyglycerol are depicted. Three of the four measurements show clear high force peaks at 545 pN, 454 pN and 538 pN. This is consistent with a single catechol titanium dioxide interaction. One of those shows an additional high force peak at about 1 nN. This indicated that more than one catechol interact with the surface. This could either be polyvalent or multivalent, that means a second attached hPG molecule stretched between tip and surface or two catechol endgroups on one hPG that interact with the titanium dioxide surface. One of the four measurements show a peak at 265 pN indicating oxidized catechol.

In summary the high force peaks of catechol metal oxide interaction was observed for 2 of 3 measurements with a single catechol on a linker, in none of the two measurements with linear catechol functionalized hPG and in 3 of 4 of the measurements with hyperbranched catechol functionalized polyglycerol. The probability to observe a desorption event of any force was significantly lower for the linear polymer. One of the measurements with dopamine showed a even higher force peak at 764 pN indicating the adhesion of 2 dopamines and one of the hyperbranched polyglycerol measurements shows a second high force peak at 1 nN indicating either two hPG molecules or the multivalent adhesion of two molecules of the same hPG.

One explanation for the missing high force catechol peaks for the two measurements with linear polyglycerol is that the samples were oxidized during tip functionalization. This is in line with the existing small peaks of about 300pN (256 pN and 329 pN) that are in the force range for the proposed quinon titanium dioxide interaction. However if all catechols are oxidized a larger peak at 300 pN would be expected and no occasional high force events would be observed. So oxidation alone is probably not a sufficient explanation. This indicates that maybe the architecture of a linear polymer with catechol sidechains sterically limits how the catechols can orientate themselves relative to the surface. This could lower the probability to observe a high force catechol titanium dioxide interaction and together with some oxidized sidegroups can explain the missing peak for the two measurements. Interestingly in the

literature two publications also describe measuring mostly low force interactions (below 100 pN) with their catechol functionalized linear chains as listed in

Table 6.1. This implies that for the design of coatings hyperbranched or star shaped structures featuring catechols as endgroups should be preferred compared to linear structures with short catecholic sidechains.

## 6.3 Desorption force of catechol functionalized hPG from $TiO_2$

In a next step hyperbranched polyglycerols with different amounts of catecholic endgroups were desorbed from $TiO_2$. The measurements were again performed with a pulling speed of 1µm/s and a dwell time of 1s. The measurements were done with three constructs depicted in Figure 6.6 B, D and F with 0%, 8% and 40% catecholic endgroups respectively. For the catechol containing constructs McIlvaines buffer at pH 3 was used as measurement solution, for the hPG without catechol different buffers were used. In Figure 6.6 A the max force histograms of the four measurements in different buffers as described in the inset with non catecholic hPG are shown. Most of the force events for all four measurements were smaller than 200 pN. Occasional events of higher force occurred, and one measurement in MES pH5 even showed a small peak at 280 pN. Since the endgroups of the construct are to 88% hydroxyl groups as depicted in Figure 6.6 B the higher forces are probably caused by multiple hydrogen bonds.

The construct with 8% catecholic endgroups is depicted in Figure 6.6 D. Besides the 8% catechol endgroups most endgroups (90%) are hydroxyl groups. Of the five measurements three show mostly small forces below 200 pN and occasional events at 200-300 pN. Two measurements of five show broad high force peaks (310 pN ± 229 pN, 324 pN ± 157 pN) containing events in the force range of the high force catechol $TiO_2$ interaction as well as events of lower force. The events of lower force could be due to hydrogen bonds of the hydroxyl endgroups. One of the measurements showed occasional events of forces in the range of 700 pN to 1.2 nN indicating that several catechols participated in the interaction. That could be either two catechol groups of one constructs or two constructs with catechol groups. That only two of the five measurements show peaks of high force interactions could be explained by geometrical constraints. The construct is covalently attached to the tip by a PEG tether. This limits the ability of the construct to rotate. With only 8% catechol of the endgroups, it depends on the position of the catechols relative to the tether whether an interaction of the catechol groups with the surface is possible. In Figure 6.6 D an example is shown were it is unlikely for the catecholic endgroups to interact with the surface. Since the position of the tether (coupled to an amino functionalized site) and the catechols on the hPG

is random, in some measurements it will be possible to observe catechol $TiO_2$ interactions and in others it is not.

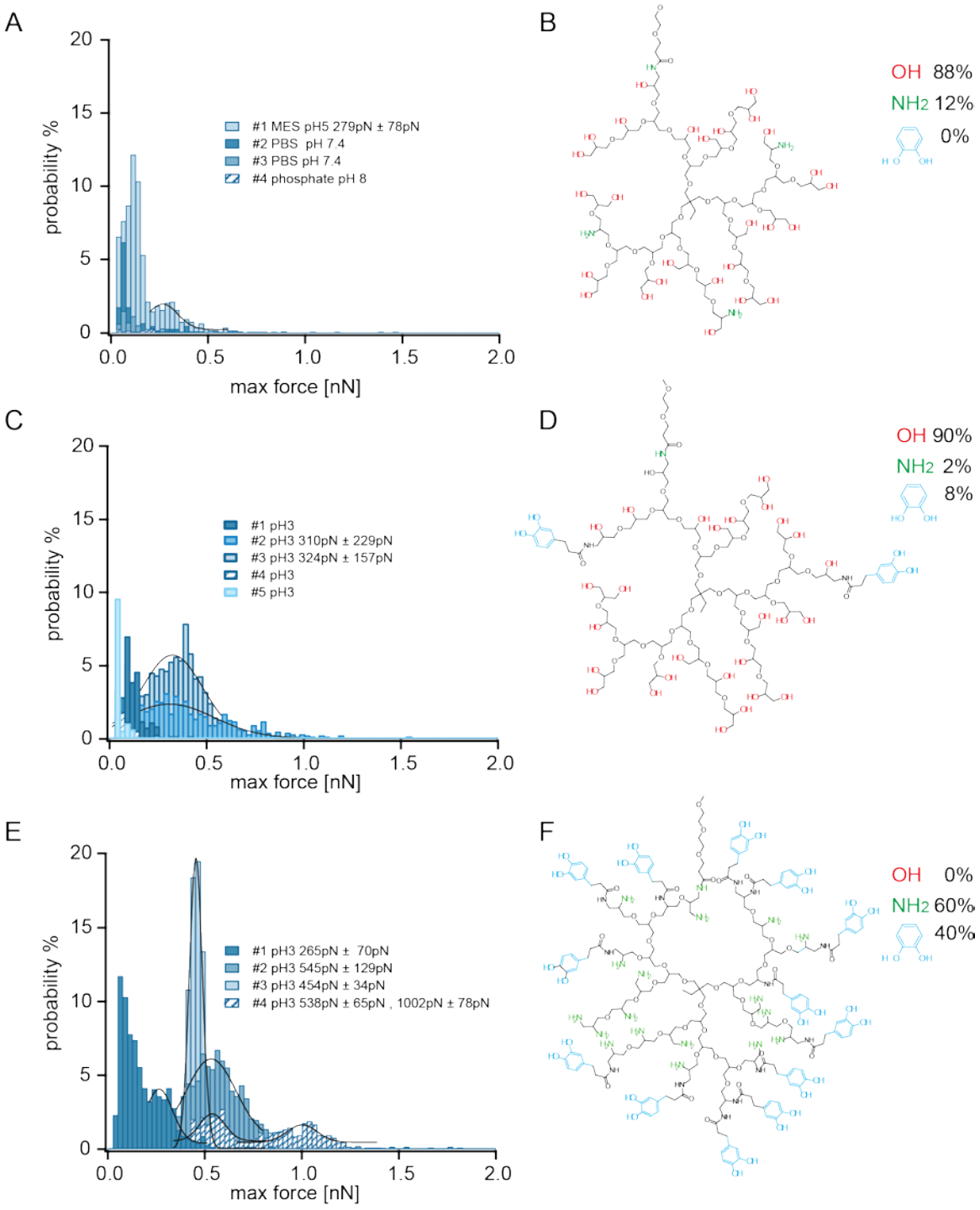


**Figure 6.6:** The maxforce histograms of several measurements with hyperbranched polyglycerol on $TiO_2$ are depicted. The histograms belonging to the hPG without catechol are shown in A. The four measurements were performed in different buffer solutions as described in the inset. B shows a schematic of the attached hPG. In C the max force histograms of 5 measurements of hPG with 8% catecholic endgroups at pH 3 are depicted, in D s schematic of the construct is given. In E the max force histograms of 4 measurements at pH 3 of the hPG with 40% catecholic sidechains is shown. In F the corresponding schematic is depicted. Where possible peaks in the max force histograms were fitted and the peak value as well as standard deviation are given in the insets.

The last construct has catecholic functionalization at 40% of its endgroups and all other endgroups are amino groups. This is depicted in Figure 6.6 F. The max force histograms are shown in Figure 6.6 E. Three of the four measurements show clear high force peaks at 545 pN, 454 pN and 538 pN. One shows a lower force peak at 265 pN that could indicate oxidation. Two measurements show occasional events at even higher forces above 700 pN and another has even a second high force peak at 1 nN. This is due to the interaction of two catecholic groups, either multivalent as two catechols on one construct or polyvalent as two constructs with one catechol interaction each.

The measurement showed that functionalizing hPG endgroups with catechol strongly enhances the adhesion to $TiO_2$. Adding more catecholic endgroups increases the likelihood of catecholic titanium dioxide interaction. Measurements of the construct with 8% catechol showed high desorption forces for two out of five measurements while for 40% catechol three out of four measurements showed high forces. Multiple catechol titanium dioxide interactions were occasionally observed in one of the five measurements with 8% catechol and in two out of four measurements with 40% catechol. Additionally one of the four measurements with 40% catechol showed a clear second high force peak with forces corresponding to roughly twice the catechol titanium dioxide desorption force.

## 6.4 Dwell time effect

The measurements so far have been performed with a surface dwell time of 1s. In the one measurement with hPG functionalized with 40% catechol that showed a double dopa peak, the dwell time on the surface was varied to study the effect that surface contact time has on the probability and force of desorption events. When considering surface contact time not only the dwell time at the trigger force value has to be considered but also the time that is needed to reach the trigger force. Dwell times of 0 s, 1 s, 4 s and 10 s have been measured and at 0s additionally to the normal trigger force a smaller trigger force was used as well. For the small trigger force the tip needed 30 ms from first surface contact to reach the trigger force and retract again until contact with the surface is lost. With the larger trigger force this value was 160 ms. So the total surface contact time in the measurement serried was 30 ms, 160 ms, 1.16 s, 4.16 s and 10.16 s. Each dwell time measurement was repeated in different order so that no time effect biased the result. Figure 6.7 summarizes the results of the measurement. In A the max force histograms belonging to the different dwell times are plotted in different colors. The number of events is normalized to the number of measured force curves. The 30 ms (yellow), 160 ms (red), 1 s (light blue), and 4 s (dark blue) measurements show two clear peaks each corresponding to interactions of one and two

catechol groups with the titanium dioxide surface. The longest 10s dwell time measurement even has three clear peaks. Two interesting points can be made from the data. Multiple catechol events become more likely with increased dwell time and interestingly the single catechol interaction force increased with increasing surface contact time. Figure 6.7 B shows the max force of each curve plotted against the curve number. The data points are again color coded. This figure illustrated that the force is not changing over time. The probability to observe an event is low for the first 1500 force curves (measured with 1 s dwell time) and then very high until the end of the measurement. Due to the low probability of events at the beginning of the measurement the overall probability to measure an event is with 42% the lowest for the 1 s dwell measurement. The 61% probability of an event for the measurement with the smaller trigger force and only 30ms of contact time however is not caused by time effects. This is a markedly lower probability compared to the 99.6% for the higher trigger force and 160 ms contact time. For the 4 s and 10 s dwell times 99.8% respectively 100% of the curves showed events.

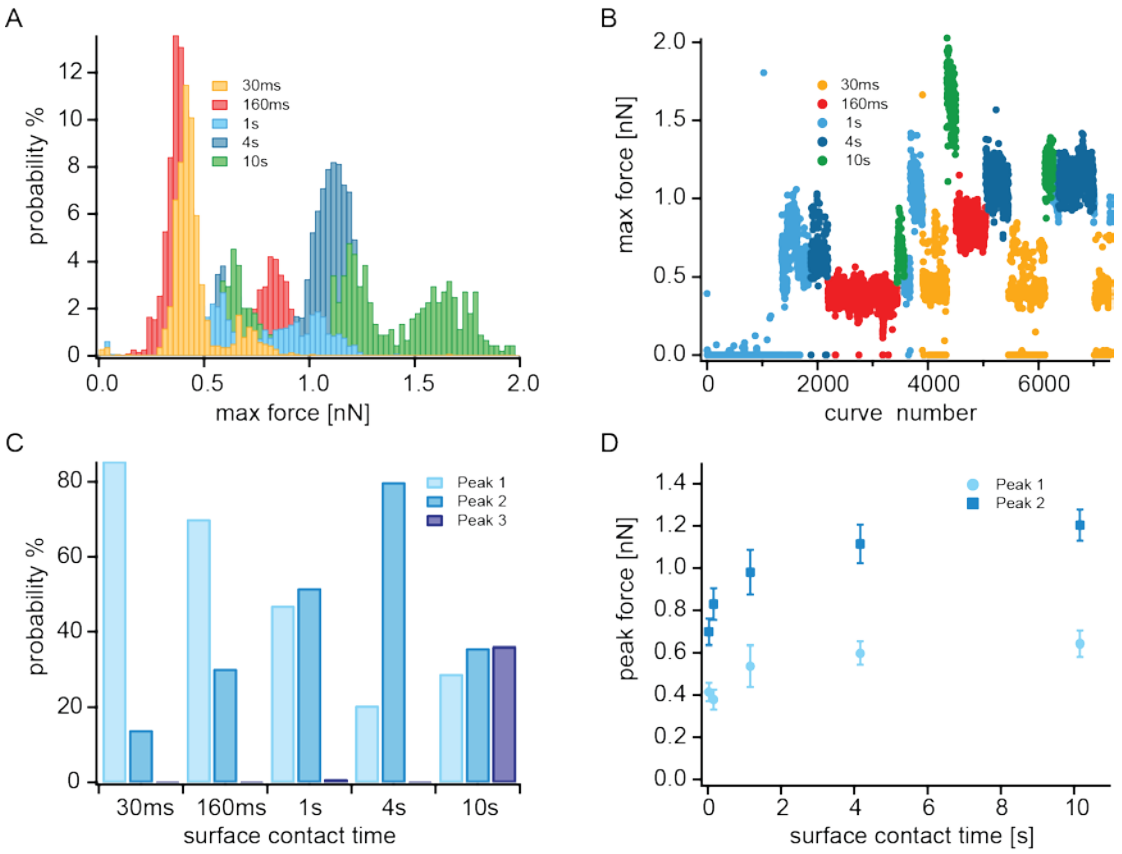


**Figure 6.7:** A shows max force histograms for the different surface contact times (color code given as inset) normalized to the number of measured force curves. In B the max force is plotted against the curve number. C shows which fraction of the force events belongs to force peak 1, 2 or 3 for the different surface contact times. In D the peak values of the max force histograms for the first and second peak are plotted against the surface contact time. The standard variation of the gauss fit is given as error.

At lower surface contact time the first peak indicating a single catechol interaction is more prominent than the second peak. This is changing with increasing dwell time. This is

illustrated in Figure 6.7 C. The probability of a single, double or triple interaction in relation to the total number of events is plotted for the different surface contact times. For 30 ms and 160ms contact time a single interaction is more probable. At 1 s dwell time single and double events have a similar probability, at 4 s the double catechol interaction is more likely. For the 10s measurement the interaction of one, two or three catechol groups with the surface is all of approximate equal probability. Besides the shift to multiple interactions with increased dwell time, it seems that the force of a single interaction increases with increasing dwell time. The max force peaks in Figure 6.7 A are fitted with a Gaussian and the peak values as well as the standard variation are extracted. These values are plotted in Figure 6.7 D against the surface contact time. The forces of the single peak as well as the double peak increase with increasing contact time. The increase is largest between zero dwell time and 1 s dwell time but there is still some measurable increase in force between 4 s and 10 s dwell time indicating a slow process in the adhesion of hPG-catechol on titanium dioxide.

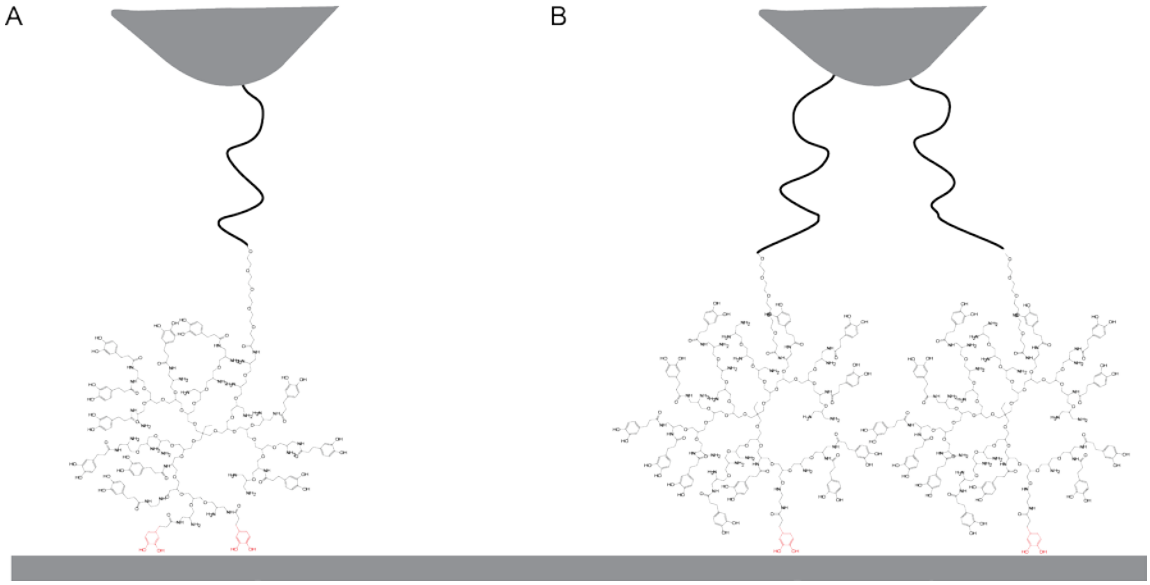


**Figure 6.8:** A schematic of the different possibilities for attachment via multiple catechols is depicted. A shows a multivalent attachment were one hPG molecule is attached to the surface via two catecholic surface anchors. B shows a polyvalent attachment were two hPG are attached to the surface with one catechol each and they are attached to the tip via two different PEG linkers.

The double peaks in the measurement could be multivalent as illustrated in Figure 6.8 A or polyvalent as in Figure 6.8 B. In a multivalent interaction more than one catechol group of the same hPG molecule interacts with the surface. For this to be possible the orientation of the catechol endgroups on the surface has to be correct for more than one catechol group. With 40% catecholic endgroups this should be possible. The other possibility is that more than one functionalized hPG is covalently attached to the tip and that two hPGs can interact with the surface simultaneously.

The 10kDa PEG linker is not completely monodispersive, thus the length is a little different for each linker. Because of this it is sometimes possible to distinguish interactions of different linkers when looking at the length scale of interactions. In Figure 6.9 A the max force of each measured curve is plotted against the max length. It is possible to distinguish two clusters in the scatterplot. The cluster belonging to higher forces at a certain distance are associated with a shorter PEG tether, the ones with lower forces to a longer tether. A partition of the data point in the two groups shows that the multiple desorption events belong to the shorter tether as can be seen in the force histograms in Figure 6.9 B. So there are two PEG linkers of different length with catecholic hPG on the tip. The higher forces belong to the force-extension profile of the shorter linker. This could either mean that the hPG on the shorter linker attaches via two catechol groups and the one on the longer linker only via one catechol group. Or both catecholic hPG attach via one catechol and the force is distributed on both linkers with the shorter linker taking more of the force load. Then as soon as the hPG on the shorter linkers ruptures from the surface the full force is on the longer linker leading to a rupture in the second catecholic hPG soon after. Depending on how fast the second hPG ruptures from the surface this can be seen in the shape of the force distance curves.

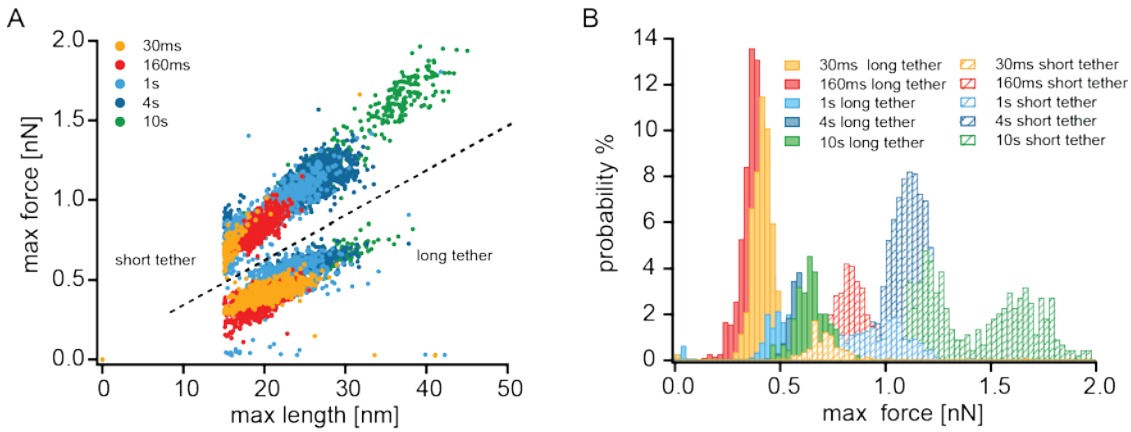


**Figure 6.9:** In A the max force is plotted against the distance at max force for each force distance curve. The different measurements are depicted in different colors. The measurement points form two large clusters belonging to PEG linkers of different length. The data points are sorted into the two groups and in B the max force histograms of those groups are plotted. The shorter linker is associated with the higher forces.

It is possible to distinguish between different kind of curves as shown in Figure 6.10. In A the max force and the detach force are not the same. First one hPG on a shorter linker ruptures than a second linker to a second hPG is stretched and ruptures. In B there is no second peak just a cluster of measurement points in the rupture of the shorter linker. This cluster of points indicates that there is a second hPG on a different linker and the hPG catechol bond can hold the force for a short time before rupture. The cluster of mesurement points is called inter rupture force. In the third kind of curve shown in C only one peak is visible and the rupture occurs fast without any observable force cluster. This could mean only one linker with one hPG is involved in the interaction or that the second linker ruptures too quickly for the

measurement to resolve a cluster. The force histograms grouped into the three different types are shown in Figure 6.10 D for all measurements and in Figure 6.10 E for the 1 s dwell measurement only. At lower forces most curves show clean ruptures. At the higher force peaks a significant part of the curves show a second peak or a cluster in the rupture indicating that two hPGs interact with the surface. Intersestingly for the 1 s dwell measurment the double catechol peak is bimodal with the peak of the clean looking high force ruptures a little lower than the peak of the curves with inter rupture force. This could be a hint that sometimes the double catechol interaction is multivalent with two catechols on one peak (lower of the two peaks) and sometimes the inteaction is polyvalent with two hPGs (higher part of the peak). The forces are slightly different since the force distribution between the two catecholic interactions can be different in those cases. In Figure 6.10 F the detach force is plotted against the inter rupture force illustrating how the forces on the two tethered hPGs add up in the polyvalent case. The detach force is about 1.5 times the force of the corresponding inter rupture force in this case.

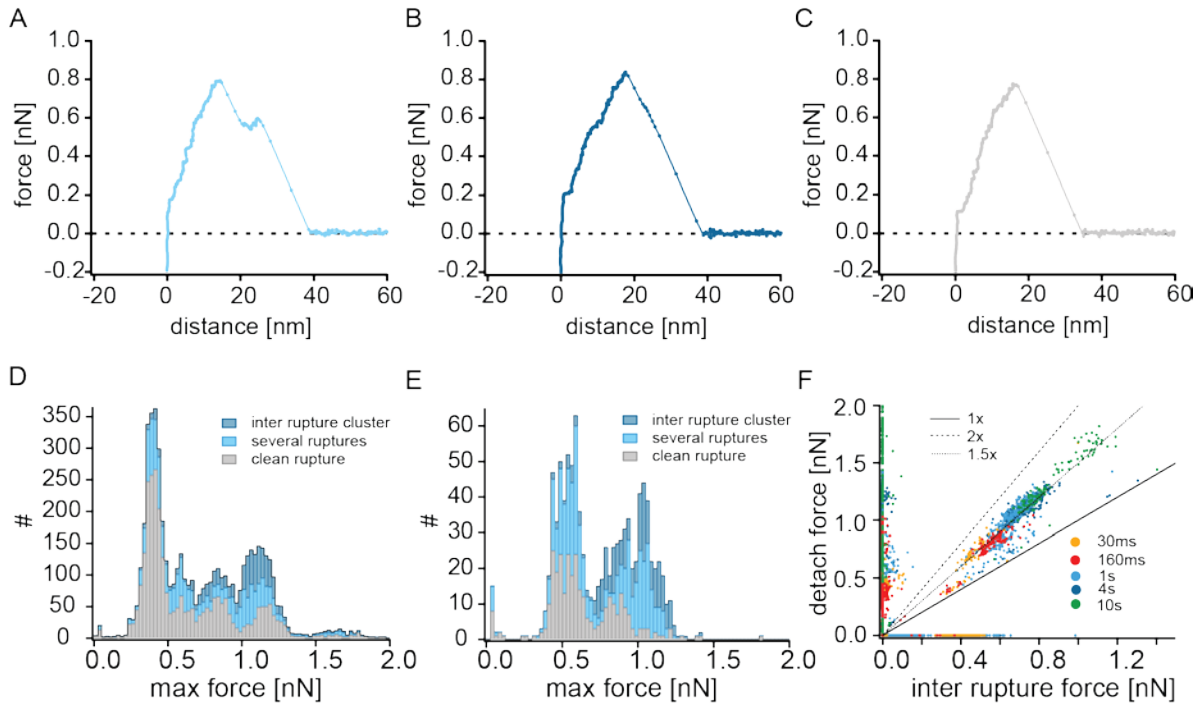


**Figure 6.10:** A, B and C depict three different types of observed force curves. In A the max force peak is not the same as the detach peak, two peaks are clearly visible. In B only one peak is visible but the rupture is not smooth but interrupted by a cluster of measurement points, the inter rupture force. C shows a single peak with a clean rupture. In D the max force histograms is given for the different curve types. Clean ruptures are shown in grey, ruptures were max peak and detach peak are distinct in light blue and ruptures with inter rupture clusters in dark blue. The same is plotted in E just for the 1 s dwell measurement. In F the detach force of each force curve is plotted against the inter rupture force. The different dwell parameters are depicted in different colors.

In a number of force distace curves it is apparent that more than one hPG is part of the interaction. Excluding the visible polyvalent events from the force histograms yields the plot in Figure 6.11 A. Only the max forces of curves with clean ruptures and no second peak like in Figure 6.10 C were extracted. For Figure 6.11 B the detach forces of curve types Figure

6.10 A and C with clean ruptures were collected. In Figure 6.11 C the values of the inter rupture forces were collected in histograms. Here is was confirmed that the given inter rupture force value is the last interaction before the force drops to zero. All those histograms were fitted with gaussians and the extracted values were plotted against the surface contact time in Figure 6.11 D.

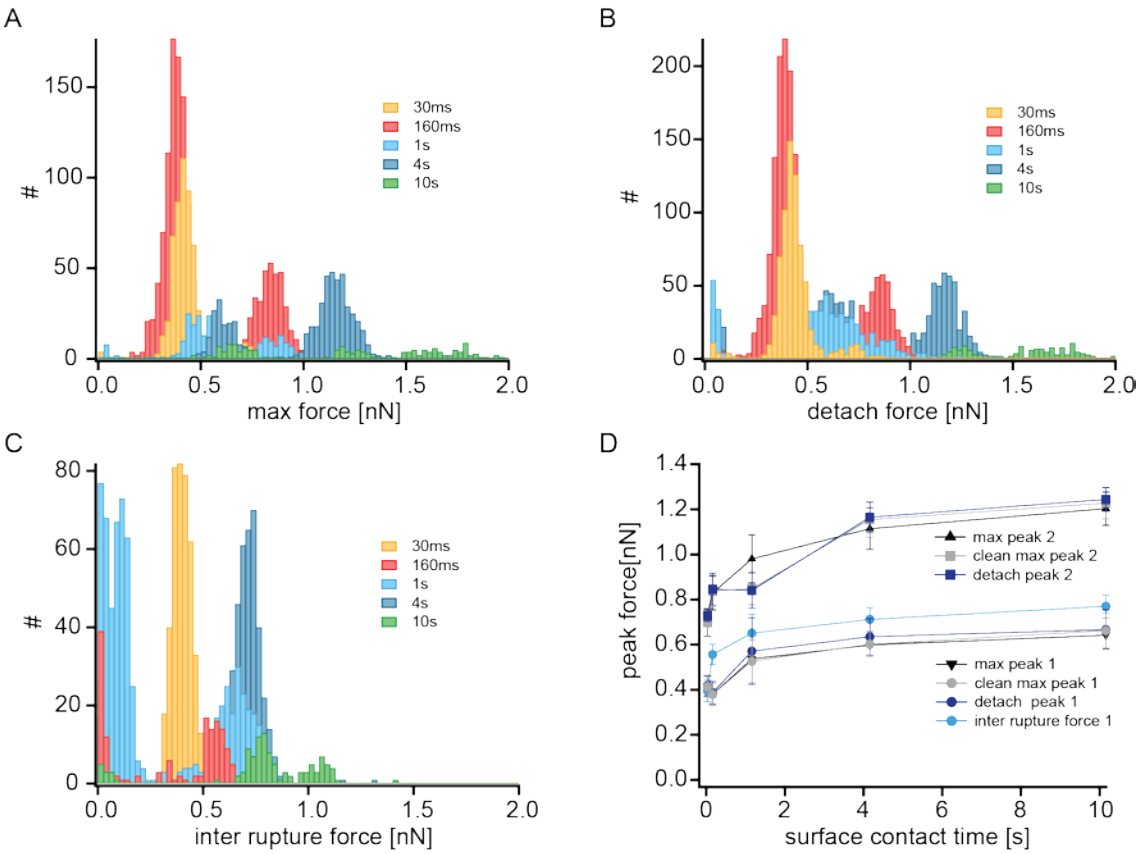


**Figure 6.11:** In A the maximal force values of the curves in which detach peak and max peak coincide and there is a clean rupture are collected in histograms. Different dwell times are plotted in different colors as described in the inset. In B all detach forces of force curves with clean ruptures are plotted in histograms. In C the inter rupture force histograms are shown. In D the peak values of the force peaks depicted in A, B and C are plotted against surface contact time. The peak values of all max forces are given as comparison. The error bars are the standard variation of the gauss fit.

The max force peak values including all kind of curves from Figure 6.7 A are given as comparison. For the lower force peak the max force peak for all curves,the max force peak for clean ruptures and the detach force peak match for all surface contact times. For the second force peak all forces for all surface contact times except 1 s overlap. For 1 s dwell time the second peak seems to be in part due to multivalent and in part to polyvalent interactions with different force values. Because of this the values for the clean rupture max and detach forces are lower than for those with inter rupture force clusters. It is interesting to have a closer look at the inter rupture forces. They follow the same trend of increasing force with surface contact time but are about 100 pN higher than the max forces. The reason for the slightly higher forces is that the force load is shared with another hPG and the full force is

only experienced for a short time after the rupture of the second hPG. For the 10 s dwell measurement there is a second peak of inter rupture forces above 1 nN. Indicating one hPG with two catecholic interactions. This means that in the case of the triple max force peak two hPGs are involved. One with a single catecholic anchor and the second with two catecholic anchors.

In summary one can say that the increased surface dwell time increased the probability of catecholic interactions. With increasing dwell time it was more likely that more than one catechol interacted with the surface. In a large number of curves two different catecholic hPGs interacted simultaneously with the surface in a polyvalent manner as can be seen by the inter rupture forces. But sometimes also two catechols of one hPG bound to the surface in a multivalent manner. In the case of the 10 s dwell measurements there was even a triple interaction involving both poly- and multivalent anchoring.

Furthermore, increasing the surface contact time leads to higher interaction forces for the single catecholic hPG surface interaction. As the nature of the interactions is not fully understood the reasons for this are not clear. There are several possible explanations. The slow relaxation of the interaction could involve only the catechol or the whole hPG. The catecholic group could take different conformations of the aromatic ring on the surface [91] or it could “roll” [92] from one titanium dioxide lattice site to the next and find the energy minimum on the surface.

## 6.5 Conclusion

The desorption of different hyperbranched polyglycerols constructs from a titanium dioxide surface showed very high forces around 500 pN and a reversible bond formation at low pH. A higher amount of catecholic functionalization led to an increased probability to observe high force events. For the 8% catecholic hPG 20% of the tips showed a large number of high force events, for the 40% catecholic hPG 75% of the tips. Sometimes even poly- and multivalent attachment of multiple catechol groups could be observed. The desorption of linear polyglycerols with catecholic side chains showed no high force peaks. While some of the catechol groups may have been oxidized during functionalization this could be a hint that the attachment as sidechains to a linear polymer chain sterically limits the conformation of the catechols on the surface. Increasing the surface dwell time increases the probability of multiple desorption events. Furthermore increasing the surface dwell time increases the catechol titanium dioxide desorption force. Most of the details about the nature of the interaction are not known. Lee et al. explained the pH dependence with auto-oxidation of the catechol groups to quinons and assigned the catechol a high force interaction and the quinons an interaction of lower force. Further theories have been proposed including pH

dependent “standing up” or “lying down” conformations [91]. Diebold et al. observed different mobility, via “rolling” of the catechol on the surface, depending on hydroxyl concentration. [92]

The measured high desorption forces and the branched structure with the possibility of multivalent surface anchors make catecholic hPGs a good candidate for surface coatings. This has been recently demonstrated by Wei et al. [49] hPGs with just 5% of catecholic endgroups formed a stable monolayer of a titanium dioxide surface that was resistant to fibronectin adhesion as can be seen in Figure 6.12 A. hPG with 10% catecholic endgroups were as stable against oxidative detachment as constructs that were additionally crosslinked by vinyl groups. That 16 h in oxidative environment has the same degrading effect on the surface as 30 days in Hepes buffer underscores again how sensitive the interaction is to oxidation.

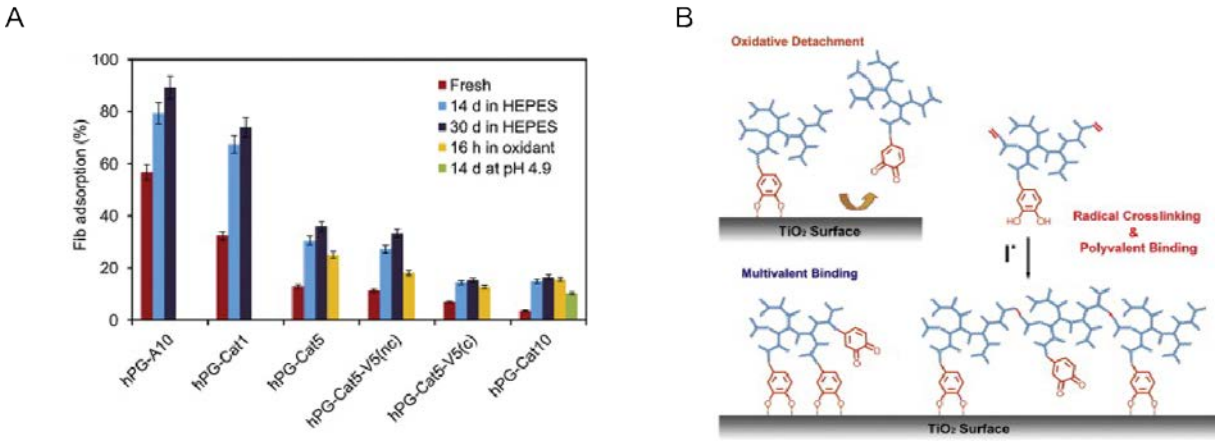


**Figure 6.12:** A shows the fibronectin adsorption to surfaces coated with different hPGs. hPG A10 contains no catecholic endgroups, Cat1 1%, cat5 5% and cat10 10% of catecholic endgroups. Cat5 V5 is additionally functionalized with 5% vinyl groups for crosslinking. B shows how the hyperbranched polyglycerol can adhere poly- or multivalently to the titanium dioxide surface. Adapted from [49]

That the antifouling performance of 10% catecholic hPG was comparable to the construct with additional covalent crosslinks shows that multivalent as well as polyvalent binding as illustrated in Figure 6.12 B is possible for the construct. Besides the use as antifouling coatings the constructs could be employed as medical adhesives.

# 7 Conclusion and Outlook

The presented single molecule AFM desorption experiments gave new insight into the molecular mechanisms of adhesion. For the dynamics of desorption of polypeptides a high cooperativity and center of mass diffusion scaling was found. The effective monomeric desorption rate is several orders of magnitude lower than for single peptides, indicating that the cooperativity of the chain slows down the desorption. The slow dynamics are reflected in the fact that long polymers in the metastable state would need about half an hour to spontaneously desorb.

For surface coatings that have to be stable for extended periods of time, high force interactions combined with a branched structure are needed. Hyperbranched polyglycerols functionalized with catecholic endgroups satisfy those requirements. Desorption measurements showed high force interaction between the catechol endgroups and titanium dioxide. The construct with 40% catecholic sidechains even exhibited sometimes very strong multiple catechol interaction events that were more frequent with an increased surface dwell time. The possibility of multivalent anchoring and the reformable high force catecholic interaction makes this construct very promising as antifouling coating and underwater adhesive.

In a next step desorption from supported lipid bilayers instead of the well defined solid hydrophobic substrates was investigated. While surprisingly the time scale of desorption seems to be comparable for lipid bilayers and solid hydrophobic surfaces, the desorption is far more complex on lipid bilayers involving also rearrangements of the lipids. This is apparent in the unusual curve shapes seen in the desorption experiments. The experiment showed that the aromatic hydrophobic residues of tyrosine and tryptophan have a high affinity for the zwitterionic phospholipid membrane.

Advancing to a more medically relevant system, the phospholipase A2s from naja mozambiqua and the honey bee were desorbed from the zwitterionic bilayer and showed high desorption forces. The family of phospholipases A2 give the interesting opportunity to study the relationship between the adhesive properties of the enzymes and their function. Several homologous phospholipases A2 are structurally conserved but are not conserved in amino acid sequence at the interfacial binding surface. [36] The amino acids in the vicinity of the interfacial binding surface correlate with the affinity to different kinds of membranes. This membrane specificity influences the different functions of the phospholipases which is relevant for the development of drugs. In a recent study it was found that the phospholipase

A2 IIA with many charged residues in the interfacial binding surface was pro-inflammatory while the phospholipase A2 V with far less charged residues and a tryptophan at the binding surface [93] has an anti-inflammatory function. [38]

Here additional experiments comparing the adhesion of phospholipase A2 from group IIA to group V on zwitterionic and charged lipid bilayers would be promising. Furthermore with the new possibilities of fast AFM imaging, experiments combining imaging of the activity of phospholipases on lipid bilayers with force spectroscopy measurements are feasible.

Altogether this work showed how AFM-based methods can yield unprecedented insights into molecular mechanisms of biopolymers at interfaces.

# Appendix

## A1 Elastin like polypeptides (ELPs) [94]

ELP monomers and ELP trimers were characterized by AFM force spectroscopy. MGHK$(GVGVP)_{80}$C and MGH$(GVGVP)_{40}$-Foldon-C were covalently coupled to the AFM cantilever tips (MLCT, Bruker SPM probes, Camarillo, USA) and a maleimide surface was prepared to allow covalent binding between the cystein groups of the ELP constructs and the surface.

The measurements are performed with a MFP-3D SA (Asylum Research, Santa Barbara, USA, now part of Oxford Instruments) in a temperature controlled fluid cell at room temperature (25°C) or 55°C. Extension-retraction cycles are measured with a constant pulling velocity of 0.5 µm/s and a dwell time on the substrate of 1 s. During the dwell time the maleimide on the surface can form covalent bonds with the cystein groups of the ELP on the functionalized tip. During the retraction worm like chain (WLC) stretching of PEG chains and rupture are observed in the force-distance curves. For the measurement of hysteresis a smaller retraction distance is chosen and the starting point of the force curve is slowly moved away from the surface when an ELP is stretched between tip and surface. Several extension relaxation cycles are recorded until a rupture occurs.

In the force distance traces the stretching and rupture of ELP constructs is clearly visible and can be fitted with a WLC model. From the fit of the five overlaid force curves persistence length of 0.27 nm and 0.13 nm for MGHK$(GVGVP)_{80}$C (Figure A1 A) and MGH$(GVGVP)_{40}$-Foldon-C (Figure A1 B) are obtained. This shows that in the case of MGH$(GVGVP)_{40}$-Foldon-C several sequences are stretched in parallel.

The trimer MGH$(GVGVP)_{40}$-Foldon-C was then several times stretched and relaxed in succession before it ruptured. Neither for temperatures below $T_t$ (25°C, Figure A1 C) nor for temperatures above $T_t$ (55°C, Figure A1 D) a distinct hysteresis between stretch and relax curve could be observed, indicating that no folding transition occurred for an isolated ELP trimer.

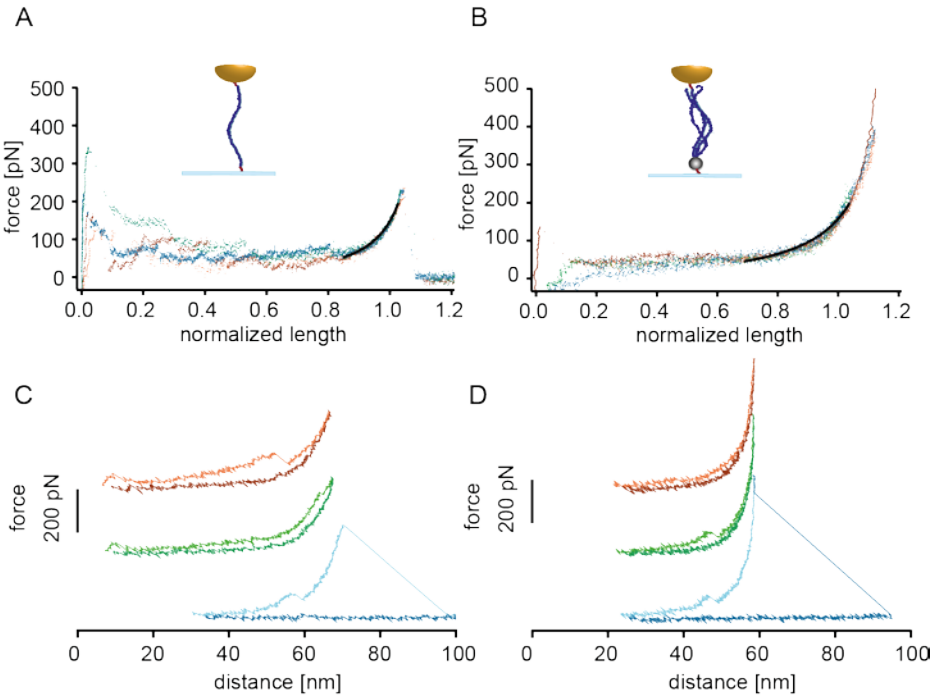


**A 1:** A normalized force-distance curves of MGHK(GVGVP)$_{80}$C and of MGH(GVGVP)$_{40}$-Foldon-C in B. For each construct 5 curves are overlaid and normalized to one at a force of 150 pN. The curves are then fitted with a wormlike chain fit (shown in black) in the force range 50-200 pN. The resulting persistence lengths are 0.27 nm (MGHK(GVGVP)$_{80}$C), 0.13nm (MGH(GVGVP)$_{40}$-Foldon-C), indicating that for MGH(GVGVP)$_{40}$-Foldon-C several sequences in parallel are stretched. Successive stretch-relaxation curves of MGH(GVGVP)$_{40}$-Foldon-C in water are shown in C below $T_t$ and in D above $T_t$ have no distinct hysteresis.

## A2 Synthesis of hyperbranched polyglycerols

*This synthesis was performed by Qiang Wei in the group of Prof. Rainer Haag at the FU Berlin. The following protocol is published as part of the publication: Wei, Q.; Krysiak, S.; Achazi, K.; Becherer, T.; Noeske, P.-L. M.; Paulus, F.; Liebe, H.; Grunwald, I.; Dernedde, J.; Hartwig, A.; Hugel, T.; Haag, R., Multivalent anchored and crosslinked hyperbranched polyglycerol monolayers as antifouling coating for titanium oxide surfaces. Colloids and Surfaces B: Biointerfaces,* ***2014****, 122, 684.* [49]

All of the synthesized catecholic hPGs were dried under high vacuum, and then stored in argon atmosphere in freezer.

1. O-Mesylpolyglycerol (hPG-OMs)

The reaction was carried out under Argon atmosphere and exclusion of water. Hyperbranched polyglycerol (10.0 g, 135 mmol OH-groups) was dissolved in abs. pyridine (60 ml) in a Schlenk flask with drop funnel magnetic stirrer. The solution was cooled down to 0 $^{o}$C in an ice bath. The solution of MsCl (1.2 eq.) in abs. pyridine (20 ml) was added dropwise so that the temperature did not exceed 5 $^{o}$C. The mixture was stirred for 16 h in the thawing ice bath. After the reaction period, solvent was evaporated by rotary distillation, and the residue was dissolved and dialyzed in $H_2O$ for 24 h to give a brown honey-like product.

2. Polyglycerylazide (hPG-$N_3$)

O-mesylpolyglycerol was dissolved in p.a. DMF upon ultrasonification in a one-necked flask with reflux condenser and magnetic stirrer. After addition of $NaN_3$ (3 eq.), the resulting suspension was heated at 65 $^{o}$C for 3 days. After cooling, the mixture was filtrated by Celite to move away the excess $NaN_3$. The filtrate was concentrated in vacuo at temperatures below 40 $^{o}$C and only handled with plastic spatula to avoid the potentially explosive degradation of the polyazide. Then the residue was further purified by dialysis in $H_2O$ for 24 h to give a brown paste-like compound.

3. Polyglycerylamine (hPG-$NH_2$)

Polyglycerylamine was synthesized by Staudinger reaction. Polyglycerylazide was dissolved in enough p.a. MeOH with 10 ml water and 1.2 eq of $PPh_3$ in a one-necked flask. After stirring for 2 days, the MeOH was distilled and the residue was dissolved in water. After filtrating most of the $PPh_3O$, the rest small amount could be purified by dialysis in MeOH for 20 h.

4. Catecholic polyglycerol (hPG-Cat)

Polyglycerylamine was dissolved in DMF, to which a solution of 3,4-Dihydroxyhydrocinnamic acid (DHHA, 1.5 eq.), (benzotriazol-1-yloxy) tris(dimethylamino) phosphonium hexafluorophosphate (BOP, 1.5 eq.), 1-hydroxybenzotriazole (HOBT, 1.5 eq.) and N,N-diisopropylethylamine (DIPEA, 10 eq.) in DMF was added dropwise. The mixture was stirred at room temperature for 16 h. After distilling the DMF, product was dialyzed in MeOH for 40 h.

5. Catecholic polyglycerol with vinyl groups (hPG-Cat-V)

hPG-Cat5-A5 was dissolved in DMF, to which a solution of acrylic acid (AA, 1.5 eq.), (benzotriazol-1-yloxy) tris(dimethylamino) phosphonium hexafluorophosphate (BOP, 1.5 eq.), 1-hydroxybenzotriazole (HOBT, 1.5 eq.) and N,N-diisopropylethylamine (DIPEA, 10 eq.) in DMF was added dropwise. The mixture was stirred at room temperature for 16 h. After distilling the DMF, product was dialyzed in MeOH for 40 h. To avoid the crosslinking of the vinyl groups, this step was only operated at room temperature.

## A3 Tip functionalization protocol

*This tip functionalization protocol is adapted from the publication: Stetter, F. W. S.; Kienle, S.; Krysiak, S.; Hugel, T., Investigating Single Molecule Adhesion by Atomic Force Spectroscopy. J. Vis. Exp,* ***2015,*** *e52456, doi:10.3791/52456.* [95]

**Reagent Setup**

Use chemicals with low water content such as dry chloroform rapidly and store dry but not longer than a week. Store both chemicals at -20 °C and under nitrogen or argon gas because APTES ((3-aminopropyl)triethoxysilan) and PEG (polyethylenglycol) are hygroscopic and PEG is subject to oxidation in air. To avoid frequent exposure of the stock to atmospheric oxygen and moisture, prepare smaller aliquots, ideally within a glovebox system with a nitrogen atmosphere.

**Equipment Setup**

Clean glassware and tweezers in detergent solution for 30 min in an ultrasonic bath at 60 °C. Rinse and sonicate equipment two times thoroughly with ultrapure water. Heat glassware and tweezers in RCA solution (ultrapure water, hydrogen peroxide and ammonia (5:1:1)) to 75 °C in an oven for 45 min and subsequently rinse them with ultrapure water. Finally, dry the glass ware and tweezers under a stream of dry nitrogen or in an oven (100 °C, 3 h).

**Tip functionalization**

Note: Use tweezers, vessels, etc. made from stainless steel, PTFE, glass or any other material which is chemically stable in organic solutions if applicable. Unless specified otherwise, carry out all steps at room temperature. The amount of incubation solution needed depends on the number of cantilever chips. Make sure that the cantilevers are immersed in the respective solutions at all time.

**Formation of OH-groups on cantilever surface (‘activation’) (approximately 0.5 h):**

- Use tweezers to place fresh cantilever chips (material: SiN, spring constant: 10 pN/nm - 100 pN/nm) on a clean glass slide and put them in a plasma chamber (100 W).

- Evacuate chamber (~0.2-0.3 mbar).
- Flood chamber with oxygen gas and evacuate again.
- Activate the plasma process (power: 20%, duration: 15 minutes, process pressure: 0.25 mbar).

**Amino-silanization of cantilevers (approximately 0.5 h):**

- Prepare the 2.5 ml of APTES solution (see Table 1) in a glass petri dish – do this ideally during the plasma process.
- Immediately after the plasma process, dip each cantilever for one second in acetone and place them immediately afterwards in the APTES solution.
- Incubate for 10 minutes at room temperature.
- Carefully rinse cantilever chips three times with 10 ml of acetone.

**PEGylation (approximately 1 h):**

Note: NHS and maleimide groups are subject to hydrolysis in aqueous environments and PEG itself is subject to oxidation in air. Therefore timing (especially in between the steps) is a critical parameter.

- Prepare the chloroform solution.
- To avoid condensation, warm PEG powders up to room temperature before opening the aliquot and weighing the appropriate amount.
- For the coupling of polymers or lipids with amino groups, separately solve NHS-PEG-NHS (6 kDa or 10kDa) and methyl-PEG-NHS (5 kDa) in the chloroform solution by vortexing them until they are completely solved.
- Alternatively. for the coupling of polymers with thiol groups separately solve Mal-NHS-PEG and methyl-PEG-NHS in the chloroform solution.
- Mix the solutions as required to adjust a certain number ratio between the NHS- or the maleimide- and the methyl-terminated PEG molecules (typically 1:1500). Note that the ideal ratio has to be determined iteratively in a series of preparation-experiment cycles.
- Incubate cantilever chips in the PEG solution for 45 minutes within a chloroform saturated atmosphere to prevent evaporation of the chloroform.

**Probe molecule conjugation (> 1 h):**

Note: The probe molecule can be conjugated to the tip via primary amino groups (NHS chemistry) or via thiol groups (maleimide chemistry). NHS-chemistry works best in aqueous

environments at pH 8-8.5. We used 50 mM sodium borate buffer at pH 8.1. Poly-D-tyrosine was solved in 1M NaOH at a concentration of 1mg/ml and the NaOH was exchanged for sodium borate buffer (pH 8.1) using spin desalting columns (7 kDa MWCO). A good alternative are dry organic solvents. For this dry chloroform, dry methanol and dry DMSO were employed depending on the solubility of the probe molecule. For maleimide chemistry a pH range of 6.0-7.5 works well. PBS with added TCEP to cleave disulfide bonds is a good reaction buffer.

- Dissolve the probe molecule at a concentration of 1mg/ml in borate buffer pH 8.1 or a suitable dry organic solvent
- Rinse the cantilevers first with 5 ml of chloroform, then with 5 ml of ethanol and finally with 5 ml of borate buffer (in the case of organic solvent rinse with chloroform followed by the organic solvent).
- Incubate the cantilever chips for 1 h in the probe molecule solution and then rinse with the reaction buffer and ultrapure water. Store in air or ultrapure water until the measurement.

# Bibliography


1. Henkel *Geschäftsbericht 2013*, Henkel AG & Co. KGaA, 2014.

2. Grand View Research, I. *Adhesives and Sealants Market Analysis And Segment Forecasts To 2020* San Francisco, 2014.

3. Mazza, P. P. A.; Martini, F.; Sala, B.; Magi, M.; Colombini, M. P.; Giachi, G.; Landucci, F.; Lemorini, C.; Modugno, F.; Ribechini, E. *Journal of Archaeological Science* **2006**, *33*, 1310.

4. Billiet, S.; Hillewaere, X. K. D.; Teixeira, R. F. A.; Du Prez, F. E. *Macromolecular Rapid Communications* **2013**, *34*, 290.

5. von Byern, J.; Grunwald, I. *Biological Adhesive Systems: From Nature to Technical and Medical Application*; Springer, 2011.

6. Gorb, S. N. *Philosophical Transactions of the Royal Society of London A: Mathematical, Physical and Engineering Sciences* **2008**, *366*, 1557.

7. Waite, J. H.; Qin, X. *Biochemistry* **2001**, *40*, 2887.

8. Lee, H.; Scherer, N. F.; Messersmith, P. B. *Proc Natl Acad Sci U S A* **2006**, *103*, 12999.

9. Yip, J.; Shen, Y.; Berndt, M. C.; Andrews, R. K. *IUBMB Life* **2005**, *57*, 103.

10. Krogh, A.; Larsson, B.; von Heijne, G.; Sonnhammer, E. L. L. *Journal of Molecular Biology* **2001**, *305*, 567.

11. Overington, J. P.; Al-Lazikani, B.; Hopkins, A. L. *Nat Rev Drug Discov* **2006**, *5*, 993.

12. Cummings, B. S. *Biochemical Pharmacology* **2007**, *74*, 949.

13. Suckling, K. *Atherosclerosis* **2010**, *212*, 357.

14. Singh, N.; Jabeen, T.; Somvanshi, R. K.; Sharma, S.; Dey, S.; Singh, T. P. *Biochemistry* **2004**, *43*, 14577.

15. Rubinstein, M.; Colby, R. H. *Polymer Physics*; OUP Oxford, 2003.

16. Marko, J. F.; Siggia, E. D. *Macromolecules* **1995**, *28*, 8759.

17. Hugel, T.; Seitz, M. *Macromolecular Rapid Communications* **2001**, *22*, 989.

18. Rief, M.; Clausen-Schaumann, H.; Gaub, H. E. *Nat Struct Mol Biol* **1999**, *6*, 346.

19. Oesterhelt, F.; Rief, M.; Gaub, H. E. *New Journal of Physics* **1999**, *1*, 6.

20. Israelachvili, J. N. *Intermolecular and Surface Forces*; Elsevier Science, 2010.

21. Prakash, S. *Advanced Inorganic Chemistry*; S. Chand Limited, 2000.

22. Kramers, H. A. *Physica* **1940**, *7*, 284.

23. Bell, G. *Science* **1978**, *200*, 618.

24. Evans, E.; Ritchie, K. *Biophysical Journal* **1997**, *72*, 1541.

25. Bizzarri, A. R.; Cannistraro, S. *Dynamic Force Spectroscopy and Biomolecular Recognition*; Taylor & Francis, 2012.

26. Getfert, S.; Reimann, P. *Biophysical Journal* **2012**, *102*, 1184.

27. Cho, W.; Stahelin, R. V. *Annual Review of Biophysics and Biomolecular Structure* **2005**, *34*, 119.

28. Alberts, B.; Johnson, A.; Lewis, J.; Walter, P.; Raff, M.; Roberts, K. *Molecular Biology of the Cell 4th Edition: International Student Edition*; Routledge, 2002.

29. Singer, S. J.; Nicolson, G. L. *Science* **1972**, *175*, 720.

30. Engelman, D. M. *Nature* **2005**, *438*, 578.

31. Petersen, F. N. R.; Jensen, M. Ø.; Nielsen, C. H. *Biophysical journal* **2005**, *89*, 3985.

32. Yau, W.-M.; Wimley, W. C.; Gawrisch, K.; White, S. H. *Biochemistry* **1998**, *37*, 14713.

33. Six, D. A.; Dennis, E. A. *Biochimica et Biophysica Acta (BBA) - Molecular and Cell Biology of Lipids* **2000**, *1488*, 1.

34. Stahelin, R. V.; Cho, W. *Biochemistry* **2001**, *40*, 4672.

35. Davidson, F.; Dennis, E. *J Mol Evol* **1990**, *31*, 228.

36. Winget, J. M.; Pan, Y. H.; Bahnson, B. J. *Biochimica et Biophysica Acta (BBA) - Molecular and Cell Biology of Lipids* **2006**, *1761*, 1260.

37. Bollinger, J. G.; Diraviyam, K.; Ghomashchi, F.; Murray, D.; Gelb, M. H. *Biochemistry* **2004**, *43*, 13293.

38. Boilard, E.; Lai, Y.; Larabee, K.; Balestrieri, B.; Ghomashchi, F.; Fujioka, D.; Gobezie, R.; Coblyn, J. S.; Weinblatt, M. E.; Massarotti, E. M.; Thornhill, T. S.; Divangahi, M.; Remold, H.; Lambeau, G.; Gelb, M. H.; Arm, J. P.; Lee, D. M. *EMBO Molecular Medicine* **2010**, *2*, 172.

39. Lee, B. P.; Messersmith, P. B.; Israelachvili, J. N.; Waite, J. H. *Annu Rev Mater Res* **2011**, *41*, 99.

40. Floriolli, R. Y.; von Langen, J.; Waite, J. H. *Mar. Biotechnol.* **2000**, *2*, 352.

41. Zhao, H.; Waite, J. H. *J. Biol. Chem.* **2006**, *281*, 26150.

42. Papov, V. V.; Diamond, T. V.; Biemann, K.; Waite, J. H. *J. Biol. Chem.* **1995**, *270*, 20183.

43. Yu, J.; Wei, W.; Danner, E.; Ashley, R. K.; Israelachvili, J. N.; Waite, J. H. *Nat Chem Biol* **2011**, *7*, 588.

44. Schweigert, N.; Zehnder, A. J. B.; Eggen, R. I. L. *Environmental Microbiology* **2001**, *3*, 81.

45. Grandbois, M.; Beyer, M.; Rief, M.; Clausen-Schaumann, H.; Gaub, H. E. *Science* **1999**, *283*, 1727.

46. Sunder, A.; Hanselmann, R.; Frey, H.; Mülhaupt, R. *Macromolecules* **1999**, *32*, 4240.

47. Sunder, A.; Mülhaupt, R.; Haag, R.; Frey, H. *Advanced Materials* **2000**, *12*, 235.

48. Roller, S.; Zhou, H.; Haag, R. *Mol Divers* **2005**, *9*, 305.

49. Wei, Q.; Krysiak, S.; Achazi, K.; Becherer, T.; Noeske, P.-L. M.; Paulus, F.; Liebe, H.; Grunwald, I.; Dernedde, J.; Hartwig, A.; Hugel, T.; Haag, R. *Colloids and Surfaces B: Biointerfaces* **2014**, *122*, 684.

50. Ghoorchian, A.; Holland, N. B. *Biomacromolecules* **2011**, *12*, 4022.

51. Dankerl, M.; Eick, S.; Hofmann, B.; Hauf, M.; Ingebrandt, S.; Offenhäusser, A.; Stutzmann, M.; Garrido, J. A. *Advanced Functional Materials* **2009**, *19*, 2915.

52. Stalder, A. F.; Kulik, G.; Sage, D.; Barbieri, L.; Hoffmann, P. *Colloids and Surfaces A: Physicochemical and Engineering Aspects* **2006**, *286*, 92.

53. Krysiak, S.; Liese, S.; Netz, R. R.; Hugel, T. *Journal of the American Chemical Society* **2013**, *136*, 688.

54. Binnig, G.; Quate, C. F.; Gerber, C. *Physical Review Letters* **1986**, *56*, 930.

55. Moy, V. T.; Florin, E.-L.; Gaub, H. E. *Colloids and Surfaces A: Physicochemical and Engineering Aspects* **1994**, *93*, 343.

56. Lee, G. U.; Kidwell, D. A.; Colton, R. J. *Langmuir* **1994**, *10*, 354.

57. Heymann, B.; Grubmüller, H. *Physical Review Letters* **2000**, *84*, 6126.

58. Merkel, R.; Nassoy, P.; Leung, A.; Ritchie, K.; Evans, E. *Nature* **1999**, *397*, 50.

59. Rief, M.; Gautel, M.; Oesterhelt, F.; Fernandez, J. M.; Gaub, H. E. *Science* **1997**, *276*, 1109.

60. Dietz, H.; Rief, M. *Proc Natl Acad Sci U S A* **2004**, *101*, 16192.

61. Dietz, H.; Rief, M. *Proceedings of the National Academy of Sciences* **2006**, *103*, 1244.

62. Butt, H.-J.; Cappella, B.; Kappl, M. *Surface Science Reports* **2005**, *59*, 1.

63. Friedsam, C.; Gaub, H. E.; Netz, R. R. *Biointerphases* **2006**, *1*, MR1.

64. Hugel, T.; Grosholz, M.; Clausen-Schaumann, H.; Pfau, A.; Gaub, H.; Seitz, M. *Macromolecules* **2001**, *34*, 1039.

65. Schwierz, N.; Horinek, D.; Liese, S.; Pirzer, T.; Balzer, B. N.; Hugel, T.; Netz, R. R. *Journal of the American Chemical Society* **2012**, *134*, 19628.

66. Pirzer, T.; Hugel, T. *ChemPhysChem* **2009**, *10*, 2795.

67. Geisler, M.; Pirzer, T.; Ackerschott, C.; Lud, S.; Garrido, J.; Scheibel, T.; Hugel, T. *Langmuir* **2007**, *24*, 1350.

68. Horinek, D.; Serr, A.; Geisler, M.; Pirzer, T.; Slotta, U.; Lud, S. Q.; Garrido, J. A.; Scheibel, T.; Hugel, T.; Netz, R. R. *Proceedings of the National Academy of Sciences* **2008**, *105*, 2842.

69. Putman, C. A. J.; De Grooth, B. G.; Van Hulst, N. F.; Greve, J. *Journal of Applied Physics* **1992**, *72*, 6.

70. Hutter, J. L.; Bechhoefer, J. *Review of Scientific Instruments* **1993**, *64*, 1868.

71. Johnson, H. E.; Douglas, J. F.; Granick, S. *Physical Review Letters* **1993**, *70*, 3267.

72. Descas, R.; Sommer, J.-U.; Blumen, A. *The Journal of Chemical Physics* **2006**, *124*.

73. Wang, Y.; Rajagopalan, R.; Mattice, W. L. *Physical Review Letters* **1995**, *74*, 2503.

74. Ainavarapu, S. R. K.; Brujić, J.; Huang, H. H.; Wiita, A. P.; Lu, H.; Li, L.; Walther, K. A.; Carrion-Vazquez, M.; Li, H.; Fernandez, J. M. *Biophysical Journal* **2007**, *92*, 225.

75. Pauling, L.; Corey, R. B. *Proceedings of the National Academy of Sciences* **1951**, *37*, 251.

76. Germann, M. W.; Turner, T.; Allison, S. A. *The Journal of Physical Chemistry A* **2007**, *111*, 1452.

77. Hanke, F.; Serr, A.; Kreuzer, H. J.; Netz, R. R. *EPL (Europhysics Letters)* **2010**, *92*, 53001.

78. Schwierz, N.; Krysiak, S.; Hugel, T.; Zacharias, M. *in preparation*.

79. Wiener, M. C.; White, S. H. *Biophysical Journal* **1992**, *61*, 434.

80. Wimley, W. C.; White, S. H. *Nat Struct Mol Biol* **1996**, *3*, 842.

81. Lee, A. G. *Biochimica et Biophysica Acta (BBA) - Biomembranes* **2003**, *1612*, 1.

82. Rief, M.; Oesterhelt, F.; Heymann, B.; Gaub, H. E. *Science* **1997**, *275*, 1295.

83. Stetter, Frank W. S.; Cwiklik, L.; Jungwirth, P.; Hugel, T. *Biophysical Journal*, *107*, 1167.

84. Beers, S. A.; Buckland, A. G.; Giles, N.; Gelb, M. H.; Wilton, D. C. *Biochemistry* **2003**, *42*, 7326.

85. Han, S. K.; Kim, K. P.; Koduri, R.; Bittova, L.; Munoz, N. M.; Leff, A. R.; Wilton, D. C.; Gelb, M. H.; Cho, W. H. *J. Biol. Chem.* **1999**, *274*, 11881.

86. Richter, R. P.; Maury, N.; Brisson, A. R. *Langmuir* **2004**, *21*, 299.

87. Krysiak, S.; Wei, Q.; Rischka, K.; Hartwig, A.; Haag, R.; Hugel, T. *Beilstein Journal of Organic Chemistry* **2015**, *11*, 828.

88. Wang, J.; Tahir, M. N.; Kappl, M.; Tremel, W.; Metz, N.; Barz, M.; Theato, P.; Butt, H.-J. *Advanced Materials* **2008**, *20*, 3872.

89. Li, Y.; Qin, M.; Cao, Y.; Wang, W. *Langmuir : the ACS journal of surfaces and colloids* **2014**, *30*, 4358.

90. Wilke, P.; Helfricht, N.; Mark, A.; Papastavrou, G.; Faivre, D.; Börner, H. G. *Journal of the American Chemical Society* **2014**, *136*, 12667.

91. Bahri, S.; Jonsson, C. M.; Jonsson, C. L.; Azzolini, D.; Sverjensky, D. A.; Hazen, R. M. *Environmental Science & Technology* **2011**, *45*, 3959.

92. Li, S.-C.; Chu, L.-N.; Gong, X.-Q.; Diebold, U. *Science* **2010**, *328*, 882.

93. Gelb, M. H.; Cho, W.; Wilton, D. C. *Current Opinion in Structural Biology* **1999**, *9*, 428.

94. Kracke, B.; Cole, J. T.; Kaiser, C.; Hellenkamp, B.; Krysiak, S.; Ghoorchian, A.; Holland, N. B.; Hugel, T. *submitted*.

95. Stetter, F. W. S.; Kienle, S.; Krysiak, S.; Hugel, T. *J. Vis. Exp.* **2015**, e52456 doi:10.3791/52456.

# List of publications

- Kienle, S.; Pirzer, T.; Krysiak, S.; Geisler, M.; Hugel, T., *Measuring the interaction between ions, biopolymers and interfaces – one polymer at a time.* Faraday Discussions, **2013**, *160*, 329.

- Krysiak, S.; Liese, S.; Netz, R. R.; Hugel, T., *Peptide Desorption Kinetics from Single Molecule Force Spectroscopy Studies*. Journal of the American Chemical Society, **2013**, *136*, 688.

- Kienle, S.; Gallei, M.; Yu, H.; Zhang, B.; Krysiak, S.; Balzer, B. N.; Rehahn, M.; Schlüter, A. D.; Hugel, T., *Effect of Molecular Architecture on Single Polymer Adhesion*. Langmuir **2014**, *30*, 4351.

- Wei, Q.; Krysiak, S.; Achazi, K.; Becherer, T.; Noeske, P.-L. M.; Paulus, F.; Liebe, H.; Grunwald, I.; Dernedde, J.; Hartwig, A.; Hugel, T.; Haag, R., *Multivalent anchored and crosslinked hyperbranched polyglycerol monolayers as antifouling coating for titanium oxide surfaces*. Colloids and Surfaces B: Biointerfaces, **2014**, *122*, 684.

- Stetter, F. W. S.; Kienle, S.; Krysiak, S.; Hugel, T., *Investigating Single Molecule Adhesion by Atomic Force Spectroscopy.* J. Vis. Exp, **2015,** e52456, doi:10.3791/52456.

- Krysiak, S.; Wei, Q.; Rischka, K.; Hartwig, A.; Haag, R.; Hugel, T., *Adsorption mechanism and valency of catechol-functionalized hyperbranched polyglycerols.* Beilstein J. Org. Chem., **2015**, 11, 828

- Kracke B.; Cole J. T.; Kaiser C.; Hellenkamp B.; Krysiak S.; Ghoorchian A.; Holland N. B.; Hugel T. , *Thermo-Switchable Nanoparticles Based on Elastin-Like Polypeptides,* submitted

- Schwierz N.; Krysiak S.; Hugel T.; Zacharias M., *On the Mechanism of Reversible Peptide-Bilayer Attachment: A Combined Experimental and Simulation Single-Molecule Study,* in preparation

# Acknowledgements

An erster Stelle gilt mein Dank meinem Doktorvater Prof. Thorsten Hugel für die gute Betreuung meiner Doktorarbeit. Er hat mir die Freiheit gegeben eigene Ideen selbstständig umzusetzen und hat mir in vielen Diskussionen wertvolle Anregungen gegeben. Durch seine immer ruhige und freundliche Art hat er eine sehr angenehme Arbeitsatmosphäre in der Gruppe geschaffen. Ich bedanke mich ebenfalls für die Möglichkeit meine Ergebnisse auf internationalen Konferenzen zu präsentieren.

Ich danke Prof. Hendrik Dietz für die Zweitbetreuung im Rahmen der Graduate School "Material Science of Complex Interfaces".

Ohne die große Anzahl an Kooperationspartnern wäre diese Arbeit nicht möglich gewesen. Ich möchte mich bei Susanne Liese und Prof. Roland Netz für die gute Zusammenarbeit und das Erarbeiten eines theoretischen Modells zur Polymerdesorption bedanken.

Ich danke Dr. Nadine Schwierz und Prof. Martin Zacharias für die Molekulardynamik Simulationen zur Untersuchung der Polypeptid-Lipid Wechselwirkungen.

Für die Synthese der biomimetischen verzweigten Polyglycerole danke ich Qiang Wei und Prof. Rainer Haag von der FU Berlin. Für die Herstellung der Titanoxidoberflächen und hilfreiche Diskussionen zum Thema Haftung danke ich Dr. Katharina Achazi, Dr. Ingo Grunwald und Prof. Andreas Hartwig vom IFAM Bremen.

Für die Synthese und das zur Verfügung stellen der ELPs danke ich James T. Cole, Dr. Ali Ghoorchian und Prof. Nolan B. Holland von der Cleveland State University.

Ich bedanke mich für die Unterstützung durch die Graduate School "Material Science of Complex Interfaces", den Exzellenzcluster "Nanosystems Initiative Munich" und dem "Center for NanoScience".

Ich möchte mich bei allen jetzigen und ehemaligen Kollegen am IMETUM und in der Physik für die gute Zusammenarbeit und die schöne Zeit zusammen bedanken. Dies gilt besonders für meine Bürokollegen Tobias, Frank, Bizan, Sandra, Bettina und Joanna.

Meiner Familie danke ich für die Unterstützung und den Rückhalt den sie mir geben. Der letze und größte Dank gilt meinem Freund Conrad.